Graphene Labs - Italian Institute of Technology

Department of Physics - University of Genova

Dottore di Ricerca in Fisica XXX ciclo, June 2018

Gold/Graphene Fractals as Tunable Plasmonic Devices

Thesis submitted in partial fulfillment of the requirements for the

Degree of Doctor of Philosophy in Physics

By

Nikhil Santh Puthiya Purayil

Supervisor:

Prof. Vittorio Pellegrini

Director, Graphene Labs, Istituto Italiano di Tecnologia (IIT)

School Coordinator:

Prof. Alessandro Petrolini

Department of Physics, University of Genova and National Institute of Nuclear Physics (INFN)

External Supervisors:

Prof. Maurizio De Crescenzi

Department of Physics, University of Rome Tor Vergata

Prof. Stefano Roddaro

Department of Physics, University of Pisa and Scuola Normale Superiore (SNS)

Abstract

Graphene, an atomically thin sheet of carbon atoms arranged in a honeycomb geometry, is attracting unique attention thanks to its extraordinary mechanical, electrical and optical properties. This thesis work concerns the realization of graphene-based nanoscale devices for novel plasmonic applications. We focus mainly on gold/graphene (Au/G) structures designed to display plasmonic multiresonances in the visible range thanks to the nanostructure geometry based on the Sierpinski carpet (SC) deterministic fractal. In addition, we study Au SC fractals without graphene, demonstrating their multiband resonance from the visible to mid-infrared range. In both Au SC and Au/G SC, we systematically investigate the far-field and near-field properties by Fourier transform infrared spectroscopy and surface enhanced Raman spectroscopy (SERS), supported by electromagnetic simulations. Hierarchical spatial distribution of electric near-field enhancement provided by Au SC is visualized on Brilliant Cresyl Blue molecules, yielding a maximum resonant SERS enhancement factor of about 10^4, while SERS measurement on Au/G exhibited a light-matter enhancement factor up to 10^5. Finally, increased light absorption due to strong electric-field enhancement provided by plasmonic nanostructures is exploited to realize a novel photodetector with broadband photoresponse and an enhancement factor up to 10 over a bare graphene photodetector.

Table of contents

Acknowledgements

The time I have spent at the Istituto Italiano di Tecnologia and University of Genova, in Genova, a lovely port city of Italy, was an experience that has tremendously contributed in shaping me as a researcher, and as a person, and it will continue to influence me for the rest of my life. I express my gratitude to everyone who contributed to it.

Firstly, I would like to thank my supervisor Prof. Vittorio Pellegrini, Director of Graphene Labs, for his consistent support despite of having an exceptionally busy schedule. He's incredibly enthusiastic in physics and has often challenged me as a researcher, which helped me to become more independent. I owe special thanks to Prof. Francesco Bonaccorso for his advices in general academics and for collaborative works. I am also immensely grateful to Prof. Alessandro Petrolini, coordinator of Department of Physics, University of Genova and to ex-coordinator Prof. Giovanni Ridolfi, for their support in enrolment as a PhD student in UniGe and in managing courses/assessments. I appreciate Prof. Iwan Moreels, Prof. Giuseppe Bandelloni, Dr. Luca De Trizio and Dr. Andrea Toma for sharing your knowledge through the graduate courses.

I'm grateful to Dr. Francesco De Nicola, Dr. Davide Spirito, Dr. Marco Polini, and Dr. Antonio Del Rio, post-doctoral researchers in IIT, for their guidance and collaborations. I'm thankful to Davide for training me in various cleanroom instruments particularly electron beam lithography. I really appreciate Francesco for being in the heart of research projects and for suggestions regarding thesis. I extend my gratitude towards all the cleanroom technicians, Eliana Rondanina, Marco Leoncini, Alessandro Bosca and Fabio

Moia for helping me out with technical issues as well as for training sessions. Likewise, I thank technicians in Graphene Labs: Luca Gagliani, Elisa Mantero and Manuel Crugliano as well as technicians in Nanochemistry and Microscopy labs. I'm thankful to Mario Miscuglio, with whom I have shared my Ph.D. process with most closely. I had a great time working in cleanroom, thanks to friendly and generous colleagues including Sedat, Andrea, Milan and Sara. Leyla and Duc Anh, along with me, formed the first batch of doctoral students in Graphene Labs. They brought fun and enthusiasm into the lab as well as in the office. I'm grateful to my colleagues: Lin Chen, Javad, Taimoor, Zahid, Nicola and Davide with whom I shared the office space with, for creating a friendly and relaxed work environment. I thank human resource organization in IIT, particularly Francesco, Arianna, Isadora and Stefano for their warm support in dealing with bureaucratic processes for foreign students.

Looking beyond IIT and UniGe to the larger physics community, I had great opportunities to meet and interact with researchers from different parts of the world through various conferences and schools. I acknowledge participants and presenters of the conference in Nanosciences and Nanotechnologies in Thessaloniki, Greece (2016) and the Nanophotonics and Micro/Nano Optics International Conference in Barcelona, Spain (2017). It was a pleasure to be able to share my research projects with scientists working in similar background and getting acquainted with them. I acknowledge strong collaboration from Vaidotas Mišeikis and Camilla Coletti, Center for Nanotechnology Innovation at NEST, Pisa, Italy. I wish the best to all other cycle XXX PhD students in Physics department,

particularly Luca, Filippo and Giovanni in their career. I thank my former colleagues from CUSAT for sharing your experiences and wisdom throughout the years.

I express my heartfelt gratitude to the group of friends outside academia that I have met during my 3 years stay in Europe. The long list includes friends from other departments of IIT including Sandeep, Milan, Cheng, Edwin, Ali, Subrahmaniam, Prachi, Zeeshan, Shovan, Assegid, Wazeem and Sankar. I also acknowledge friends from UniGe- Vinil, Praveen, Sherona, Sherin, Julia and also numerous people from various parts of Europe from academic and non-academic backgrounds that I have met during my stay and travels; all of them have contributed in widening my horizons of experiences, knowledge and perspective in different aspects of life.

Most importantly, I express my deepest gratitude to my family for all the love, support and encouragement that you have given me throughout the years.

Last, but not the least, thank you dearest reader. This would have been just a bulky stack of papers or a PDF file without you!

Chapter 1: Introduction

Deeper understanding of the underlying physical phenomenon and developments in nanoscale fabrication techniques triggered research in nanoscience and nanotechnology at an explosive rate, reporting remarkable advances and plethora of promising applications.[1] The emerging field of nanotechnology facilitated studies in the area of plasmonics, which deals with the optical phenomena related to the electromagnetic response of metals, providing the possibility to manipulate light beyond diffraction limits.[2]

Graphene, a one atom thick layer of carbon, has been a hot topic in research since its initial isolation[3] and has been described as a "wonder" material due to its unique properties.[4,5] Graphene plasmonics in particular is a new field of research that merges the extraordinary properties of graphene with that of plasmons. Graphene is a possible alternative to the traditional noble metals for plasmonics applications, thanks to its larger confinement, longer propagation distances and unique tunability.[6–8]

The main goal of this thesis work is to explore electric and optical properties of graphene and metal/graphene hybrid plasmonic systems and to demonstrate their potential applications. The key objectives of this thesis work are the following:

- Fabrication of graphene nanoribbon (GNR) and GNR based field-effect devices. This stage is intended to develop and optimize nanofabrication and characterization techniques along with investigation of optical and electrical properties of such devices.

- Design and precise fabrication of novel gold Sierpinski carpet (SC) fractals and investigation of their plasmonic properties experimentally and theoretically. Explore possibility of chemical sensing by means of surface enhanced Raman spectroscopy (SERS).
- Development of methodologies to pattern graphene without directly etching it by introducing a novel Au/G hybrid plasmonic system. This is aimed to produce devices with enhanced quality and improved light absorption. Furthermore, 1) Tailor the plasmonic resonance via electrostatic gating. 2) Study near-field enhancement via SERS. 3) Realize broadband and highly efficient photodetector based on such hybrid systems.

This thesis is organized into five chapters as follows:

- In chapter 2, plasmonic properties are briefly reviewed for metals, graphene, and hybrid systems. Necessary physical concepts are introduced along with a brief literature review.
- Chapter 3 is dedicated to the experimental methods employed to realize the aforementioned samples. Various characterization techniques are also described in detail.
- The experimental and simulation results are presented in chapter 4. A detailed examination of optical and electrical response is discussed and important findings are highlighted.
- Chapter 5 concludes and summarizes our findings.

Chapter 2: Background

2.1 Plasmonics in metals

Noble metals such as Ag and Au exhibit excellent reflectivity in their bulk form due to the large number of free electrons hosted. When the size of metal structures is reduced to subwavelength range, the electrons are confined to smaller volumes, leading to distinct optical properties due to plasmonic effect[2]. Although nanotechnology is a relatively new field of science, the preparation and use of metal nanoparticles (MNPs) had begun as early as fourth century by ancient Romans and had been widely used for decoration of glasses and ceramics.[9–11]

Fig 2.1: Lycurgus cup in reflected (left) and transmitted (right) light (Photograph: British museum).

Figure 2.1 shows Lycurgus cup, a 4th century AD Roman glass cage cup which exhibits an intriguing optical property -i.e., it appears red in transmitted light while green in reflection. Dichroic effect in Lycurgus cup is caused by the presence of finely dispersed particles of gold alloyed with silver[12,13]. The reduced size of these metal particles gives rise to the phenomenon of localized surface plasmon resonance leading to extraordinary optical properties which are tunable with particle size, shape, and medium. The major applications of metallic nanoparticles nowadays include biosensing[14,15], SERS[16], photovoltaic devices [17], optical data storage[18] and photonic metamaterials.[19]

In this section, a general outline on the origin, characteristics, types and theory of plasmons in metals is given.

2.1.1 Volume and surface plasmons

Plasmons are collective oscillations of the free electron gas of metals. They can be observed in optical experiments, where an incident light with a frequency below the plasma frequency is reflected, while light of frequency above the plasma frequency is transmitted.[2] Typical plasma wavelengths in noble metals, such as Au, Ag, and Al are approximately 145 nm, 129 nm and 81 nm respectively.[20–22] The optical properties of metals can be understood by considering the Drude model, which treats electrons within a metal as a negatively charged gas surrounding fixed ion cores. The resonance condition is due to response of plasma to the external electric-field. In bulk metal, the resonance occurs at the volume plasmon frequency ω_p, which is given by:[2]

$$\omega_p^2 = \frac{n_c e^2}{\varepsilon_0 m_c} \qquad (2.1)$$

Where $\varepsilon_0 = 8.85 \times 10^{-12}\mathrm{m}^{-3}\mathrm{kg}^{-1}\mathrm{s}^4\mathrm{A}^2$ is the permittivity of free space, $\mathrm{e} = 1.6 \times 10^{-19}\mathrm{C}$ is the electron charge, n_c is the density of free electrons, and $\mathrm{m_c} = 9.1 \times 10^{-31}\mathrm{kg}$ is the electron mass.

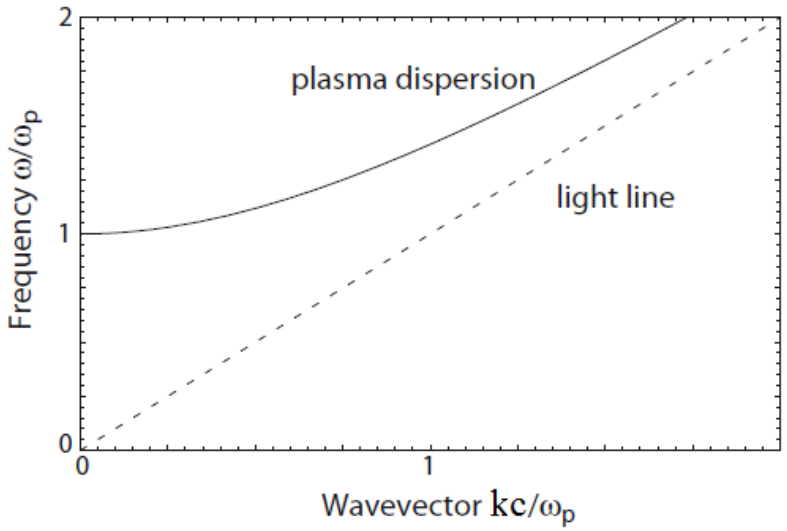

Fig 2.2: Dispersion relation of the plasmon wave of free electron gas [Adapted from Ref. 2].

The model gives a relation between bulk plasmon frequency and dielectric function:[2]

$$\varepsilon(\omega) = 1 - \frac{\omega_p^2}{\omega^2 + i\gamma\omega} \qquad (2.2)$$

Where ω is the frequency of the incident light and γ is a constant related to the damping of the oscillation due to electronic scattering. At large frequencies close to ω_p, damping is negligible, yielding:

$$\varepsilon(\omega) = 1 - \frac{\omega_p^2}{\omega^2} \qquad (2.3)$$

The dispersion relation for electromagnetic waves in a plasma is given by:[2]

$$\omega^2 = \omega_p^2 + k^2c^2 \qquad (2.4)$$

Where k is the wavevector. From Equation 2.4 it is clear that for $\omega < \omega_p$, $k^2 < 0$, so that k is imaginary. Electromagnetic waves incident in this frequency region do not propagate, but will be totally reflected. An electron gas is transparent when $\omega > \omega_p$, which describes transverse electromagnetic waves in a plasma. The dispersion relation for a generic free electron metal is depicted in Fig 2.2.

The coherent charge density oscillations propagating along the surface of a metal at the interface of two media with dielectric constants of opposite signs are called surface plasmons (SPs). Surface plasmon polaritons (SPPs) represent photon-electron waves, which travel along the interface between a metal and a dielectric. Figure 2.3a shows SPP which propagate along x-and y-directions and decays evanescently along z-direction.[2,23]

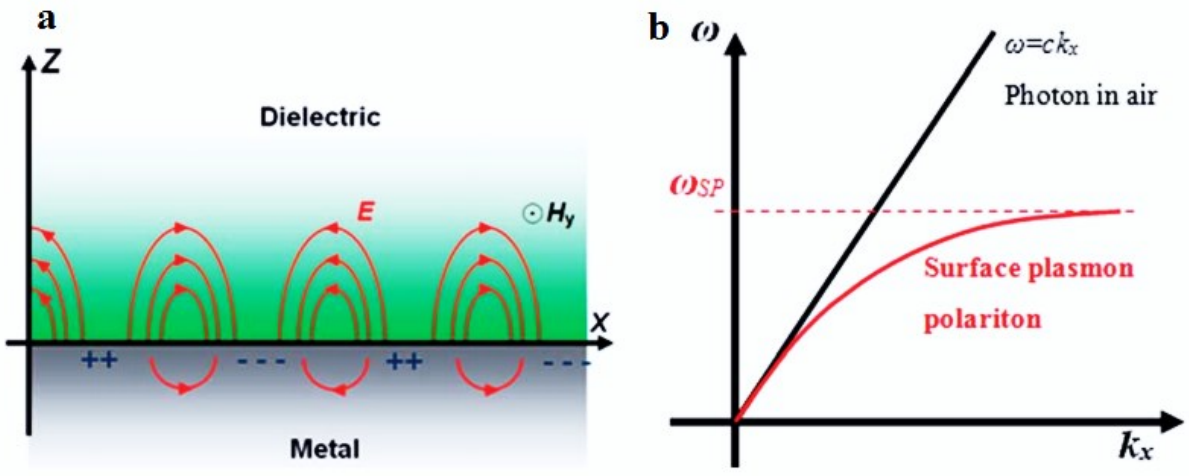

Fig 2.3: a) Surface plasmon polaritons. **b)** Dispersion curve of a typical SPP mode [Adapted from Ref. 24].

Based on Maxwell's equations, the dispersion relationship for a surface plasmon can be described by:[25]

$$K_{SP} = \frac{\omega}{c}\sqrt{\frac{\varepsilon_d \varepsilon_m}{\varepsilon_d + \varepsilon_m}} \qquad (2.5)$$

Where K_{SP} is the SP wavevector, ε_d and ε_m are the relative permittivities of the dielectric and metal respectively, and ω and $c = 3 \times 10^8 \mathrm{ms}^{-1}$ are the angular velocity and speed of light in vacuum respectively. Fig 2.3b represents the typical dispersion relation of SPPs at a metal-dielectric interface. It can be observed that a momentum mismatch exists between the photon and the SPP, which means that the incident light cannot easily excite the SPPs. In order to create a condition to bridge the momentum gap, specific configurations have to be employed. Optical excitation of SPs on metal films is first demonstrated by Andreas Otto[26] as well as Kretschmann and Raether[27] in 1968.

In the Otto configuration (Fig 2.4a), an air gap less than a few radiation wavelengths thick gives an evanescent tunnel barrier, across which the light couples to excite SPs in a total internal reflection condition.

In the Kretschmann configuration (Fig 2.4b) the metal itself acts as the evanescent tunnel barrier, resulting in a set-up that is simpler, hence more widely used than the Otto configuration. The metal should be very thin in order to allow the radiation to penetrate to the other side.[27,28]

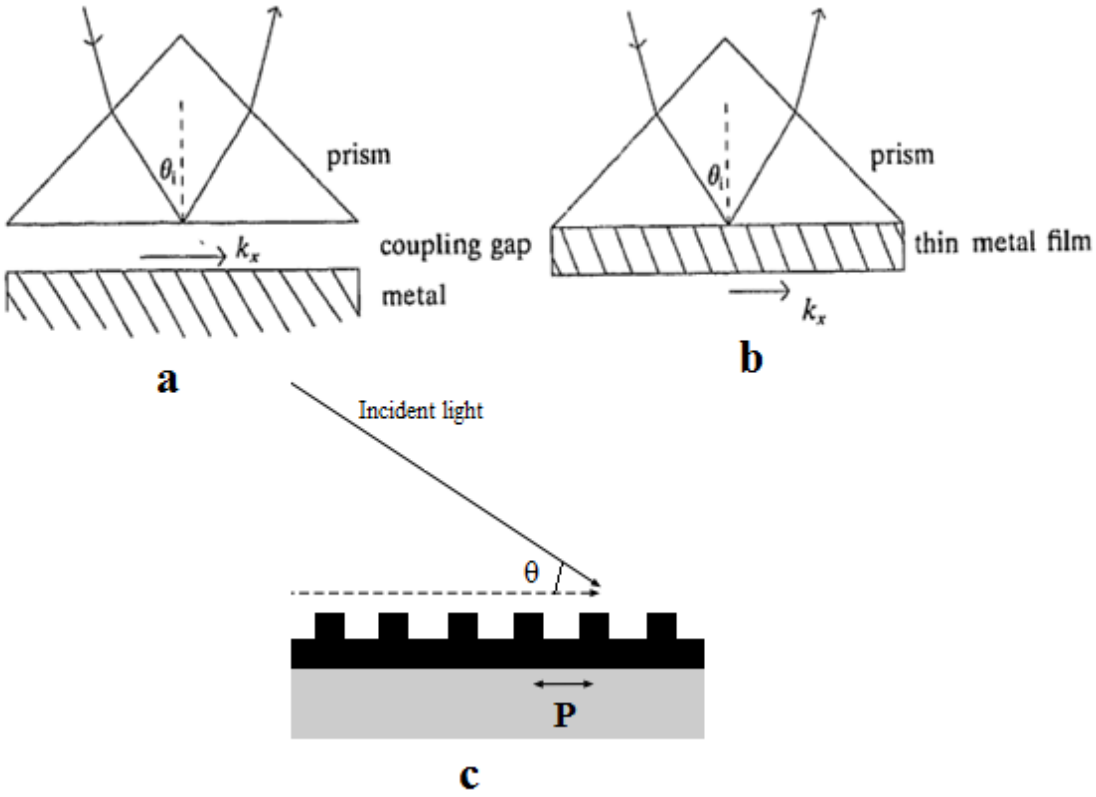

Fig 2.4: Geometries used to couple photon into a surface mode. **a)** Otto **b)** Kretschmann – Raether [adapted from Ref. 28]. **c)** Periodic grating with spacing P [Adapted from Ref. 2].

A third method employs periodic arrangement of the metal-dielectric configuration (i.e., grating) as shown in Fig 2.4c, which provides an additional momentum G = 2π/ P where P is the grating constant. The momentum matching condition of grating structure can be written as:[2]

$$k_x = k_{sp} + G = k_0 \sin\theta \pm \frac{2\pi n}{P} \qquad ; n = 1,2,3 \ldots \qquad (2.6)$$

Where θ is the angle at which the electromagnetic radiation hits the grating and k_0 is the free space wave vector of light.

2.1.2 Localized surface plasmon resonance

Localized surface plasmon (LSP) results from interaction of light with metal particles with size much smaller than the incident wavelength.[2] Figure 2.5 shows interaction of light with a nanoparticle leading to local plasmon oscillation around the nanoparticle. In the following part, influence of LSPs on the optical properties of metal particles are explained.

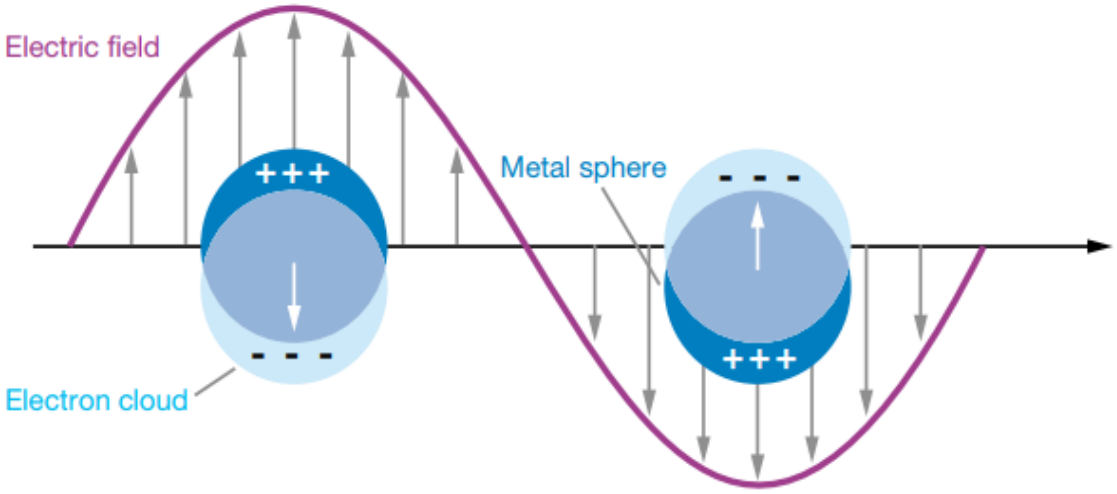

Fig 2.5: Schematic diagram of localized surface plasmon [Adapted from Ref. 23].

Generally, the basic processes taking place during light-matter interaction involve scattering and absorption. When a metal is illuminated by an electromagnetic wave, the electric charges are set to an oscillatory motion and the excited electric charges then decay through either re-emission of photons, i.e., scattering, or via non-radiative decay processes which result in absorption.[27] Hence, the plasmonic effect on the nanoparticles under the influence of an electromagnetic wave results in an enhancement of electric-field around it, called near-field enhancement and the decay results in far-field scattering and absorption.

The decrease in the light transmission as a result of absorption and scattering is known as extinction. Transmission (T), absorption (A) and reflection (R) must satisfy the conservation of energy, i.e., T + A + R = 1.

We could use Mie theory to characterize excitation of resonance modes, which is an exact solution to the Maxwell's equations for small spherical particle (radius << λ, λ being wavelength of radiation) in a non-absorbing, homogeneous medium. From Mie theory, extinction and scattering cross sections follows:[2]

$$C_{ext} = \frac{2\pi}{k^2}\sum_{n=1}^{\infty}(2n+1)\mathrm{Re}(a_n + b_n) \qquad (2.7)$$

$$C_{sca} = \frac{2\pi}{k^2}\sum_{n=1}^{\infty}(2n+1)(|a_n|^2 + |b_n|^2) \qquad (2.8)$$

And the absorption cross section:

$$C_{abs} = C_{ext} - C_{sca} \qquad (2.9)$$

Here *n* represents multipole expansion of the electromagnetic field and the coefficients a_n and b_n are given by:

$$a_n = \frac{m\psi_n(mx)\psi_n'(x) - \psi_n(x)\psi_n'(mx)}{m\psi_n(mx)\xi_n'(x) - \xi_n(x)\psi_n'(mx)} \qquad (2.10)$$

$$b_n = \frac{\psi_n(mx)\psi_n'(x) - m\psi_n(x)\psi_n'(mx)}{\psi_n(mx)\xi_n'(x) - m\xi_n(x)\psi_n'(mx)} \qquad (2.11)$$

Where ψ and ξ are Ricatti-Bessel functions of order n, $x = kr$ is the size parameter (r -being radius of the particle) and m is the ratio of the refractive index of the sphere to that of surrounding medium. i.e., $\mathrm{m} = n_m/n_d = \sqrt{\varepsilon_m/\varepsilon_d}$

When the nanoparticle size is much smaller than the incident wavelength, it can be considered as a dipole with polarizability:[2]

$$\alpha = 4\pi r^3 \frac{\varepsilon_m - \varepsilon_d}{\varepsilon_m + 2\varepsilon_d} \qquad (2.12)$$

The polarizability reaches the maximum when the real part of Drude permittivity $\mathrm{Re}\{\varepsilon_m\}$ is equal to $-2\varepsilon_d$ (i.e., Frohlich condition[2]). The wavelength at which the maximum occurs is called localized surface plasmon resonance (LSPR) wavelength. Therefore expressions for scattering and absorption cross section become:[2]

$$C_{sca} = \frac{8\pi}{3} k^4 r^6 \left| \frac{\varepsilon_m - \varepsilon_d}{\varepsilon_m + 2\varepsilon_d} \right|^2 \qquad (2.13)$$

$$C_{abs} = 4\pi k r^3 \mathrm{Im}\left\{ \frac{\varepsilon_m - \varepsilon_d}{\varepsilon_m + 2\varepsilon_d} \right\} \qquad (2.14)$$

And the extinction coefficient is:

$$C_{ext} = C_{sca} + C_{abs} \qquad (2.15)$$

The LSPR of metal nanoparticles (MNP) depends on the parameters such as size, shape, material and the dielectric constant of the surrounding environment.[29–31]

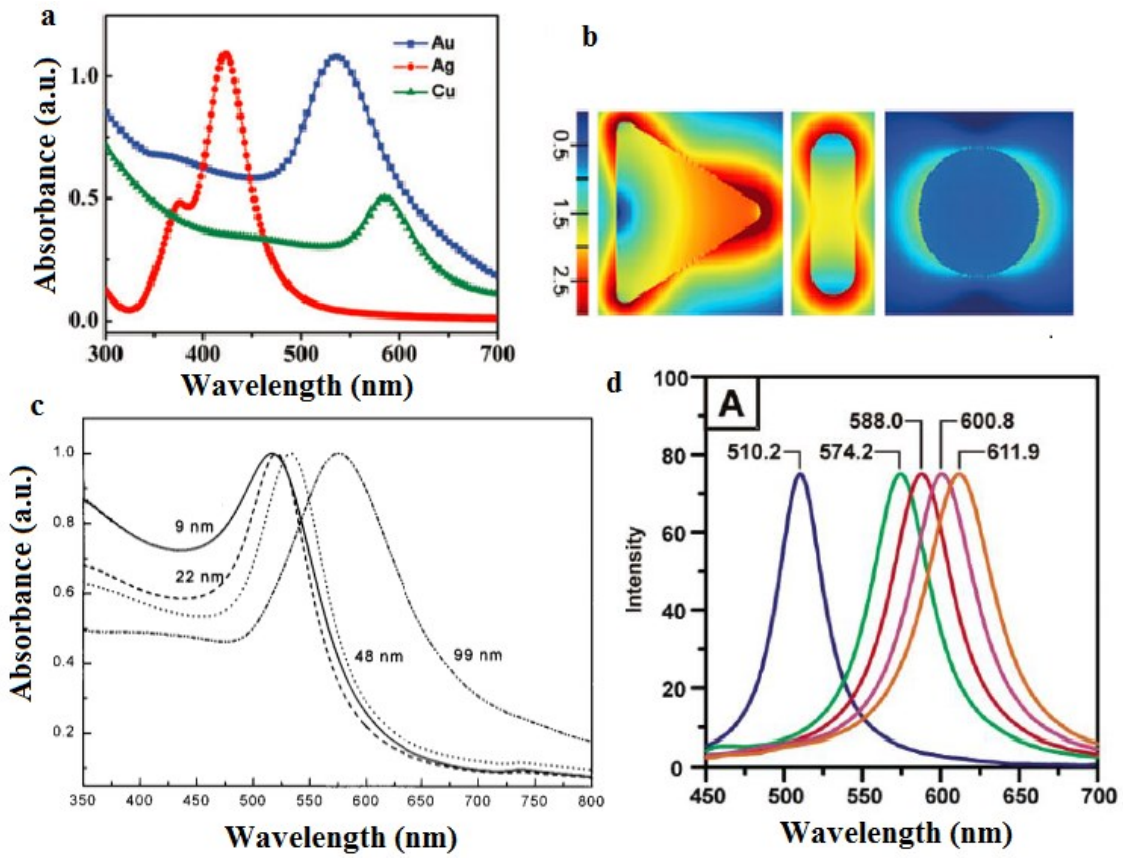

Fig 2.6: a) Absorption spectra of Au, Ag and Cu nanospheres with a diameter of 50 nm. [Ref. 32] **b)** Electric-field intensity of differently shaped Au nanocrystals (from left to right): nano-prism with an edge length of 87 nm and a thickness of 10 nm, nanorod with a length of 103 nm and a diameter of 30 nm, and nanosphere with a diameter of 50 nm [Ref. 33]. **c)** Absorption spectra of 9, 22, 48, and 99 nm Au NPs in water [Ref. 34]. **d)** Ag NP resonant Rayleigh scattering spectrum in various solvent environments (left to right): nitrogen, methanol, 1-propanol, chloroform, and benzene [Ref. 35].

The dielectric properties of the metal describe its interaction with electromagnetic radiation. Noble MNPs are of great interest thanks to their LSPR being in the visible (VIS) regime of electromagnetic spectrum. Figure 2.6a shows absorption spectra of Au, Ag and Cu nanospheres with a diameter of 50 nm exhibiting LSPR at 512 nm, 400 nm and 576 nm respectively.[32] Change in the shape of MNP modifies electric-field density on its surface, causing a shift in the oscillation frequency of the electrons.[36–38] This results in different

cross sections for absorption, scattering and extinction. Electric-field intensity in Au nanoparticles with different shapes is shown in Fig 2.6b.

The optical properties of MNPs show strong dependence on the particle size.[34,37,39] Small nanoparticles (≤ 10 nm) show prominent absorption with negligible scattering. Dipole approximation is valid in this case and their properties are due to intrinsic effects. In relatively large nanoparticles, the plasmon resonance depends explicitly on the particle size and relative contribution of absorption towards extinction decreases with increase in size. Figure 2.6c shows absorption spectra of 9 nm, 22 nm, 48 nm, and 99 nm Au nanoparticles in water. All spectra are normalized at their absorption maxima, which are 517 nm, 521 nm, 533 nm, and 575 nm, respectively.[34]

In addition, the plasmonic resonance depends on the surrounding environment of MNP.[40–43] An increment in the refractive index of the surrounding medium results in a decrease in the restoring force for the electron oscillation, which in turn causes a decrease in plasmon oscillation frequency. Single Ag nanoparticle scattering spectrum in various solvent environments is shown in Fig 2.6d, where LSPR exhibits a linear relationship with solvent refractive index.[35]

2.2 Fractal structures

In simple terms, a fractal geometry is built upon the rule of self-similarity, i.e., a characteristic pattern repeats itself on different length scales. This property, called scale invariance, is a fundamental concept in various aspects. A keen interest over the past decade in designing and realizing fractal metamaterials resulted in the development of

compact, multiband, and high-gain antennas intended for radio- frequency applications[44], terahertz (THz) resonators[45–47], lasers[48], and microwave devices.[44,49] In the infrared (IR) range, plasmonic fractal structures which act as frequency-selective photonic quasi-crystals have been reported.[50–52] In the following sections, the concept of self-similarity will be introduced along with examples of representative deterministic fractal structures.

2.2.1 Fractals and self-similarity

It was B. Mandelbrot[53] to coin the term "fractal", which is related to the Latin word *frangere* (to break). He described a fractal as "a rough or fragmented geometric shape that can be split into parts, each of which is (at least approximately) a reduced-size copy of the whole." A self-similar object is characterized by a particular symmetry, the symmetry of scale. As a consequence, a fractal can be magnified and yet remain equal to the original object. In contrast to the Euclidean geometry, fractal objects are characterized by a non-integer dimensionality, which derives from their distinctive self-similarity, meaning that the spatial structures observed on one length scale appears identical when observed at successively smaller scales.[51,54] More precisely, deterministic fractals[53] can be defined as self-similar objects generated by geometrical rules, having a Hausdorff-Besicovitch dimension[55] or fractal dimension (d_H) exceeding their topological dimension. For a fractal, the Hausdorff-Besicovitch dimension can be calculated as $d_H = \log \mathcal{N} / log(\mathcal{L}^{-1})$ where $\mathcal{N}$ *and* $\mathcal{L}$ are the number of elements forming the fractal and their size respectively.[56] The concept of fractal dimension will be described with examples in following section.

Figure 2.7a shows the Koch curve, one of the earliest fractal curves, described by Swedish mathematician Helge von Koch.[57] Generation of Koch curve starts with an equilateral

triangle, removing one third of each side, constructing another equilateral triangle at the location where the side is removed, and then repeating the process iteratively. In other words, in a Koch curve, each side is divided into $\mathcal{N} = 4$ parts, each of which is a rescaled version of the original side, scaled by a factor 1/3. The fractal dimension is given by $3^{d_H} = 4$, with $d_H = \log 4/\log 3 \approx 1.26$.

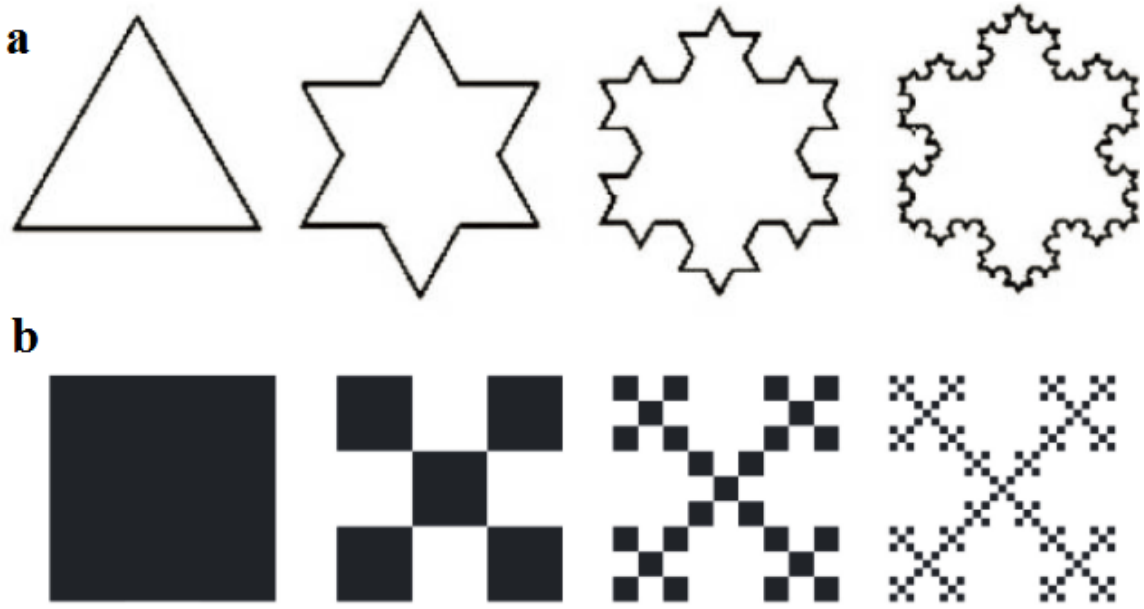

Fig 2.7: Examples of fractal structures: **a)** Four stages in the construction of Koch snowflake [Adapted from Ref. 58] and **b)** Vicsek fractal structure [Adapted from Ref. 59].

Figure 2.7b shows another example of a fractal, proposed by Tamás Vicsek.[60] In a Vicsek fractal, a basic square is decomposed into 9 smaller squares in a 3-by-3 grid. Then the four squares at the corners and at the middle are left, while other squares being removed. The process is recursively repeated for each of the five remaining sub-squares. Here the fractal dimension is $d_H = \log 5/\log 3 \approx 1.46$.

2.2.2 Sierpinski carpet

The Sierpinski carpet (SC) is one of the most studied fractal structures, described by Waclaw Sierpinski.[61] Construction of a SC begins with a square, which is cut into 9 identical subsquares in a 3 x 3 array, and the central subsquare is removed. The same procedure is then recursively applied to the remaining 8 subsquares. Therefore the fractal dimension of a Sierpinski carpet is $d_H = \log 8/\log 3 \approx 1.89$.

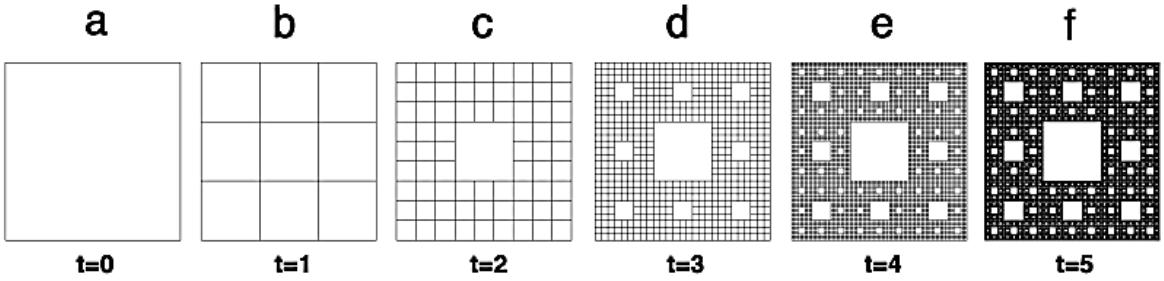

Fig 2.8: Stages in constructing SC fractals [Adapted from Ref. 62].

In general, Sierpinski carpets can be generated by a recursive geometrical algorithm employing a Lindenmayer system (L-system) implementation.[63] L-system is a deterministic approach to iteratively generate complex fractal objects starting from a finite alphabet of symbols and a collection of production rules. These rules are simple prescriptions, such as inflations, that expand each symbol into larger strings of symbols starting from an initial axiom that is considered the seed of the recursive construction. L-systems provide a computationally efficient and general method to produce many fractal shapes. In Fig 2.8, L-system implementation for the generation of first five orders of SC is depicted.

The initial axiom is *F*, while the rules to iterate are $F \rightarrow F + F - F - F - UGD + F + F + F - F), (G \rightarrow GGG)$. Both the variables *F* and *G* means “draw forward", while +/- stands respectively for “turn right/left by 90^0", and *U/D* are respectively “pen up/down".

2.2.3 Plasmonics in fractals

A variety of fractal geometries has been investigated for antenna design, offering real life applications such as multiband mobile telecommunication devices.[44] Recent advancements in high resolution nanofabrication techniques allowed realization of precisely engineered nanoscale structures, paving the way to fractal plasmonics. Fractals have been demonstrated to exhibit outstanding properties relying on the peculiar scale invariance. A particularly intriguing property attained in engineered fractal geometries is the possibility to support multiple resonances in a wide frequency range. This lead to new prospects for broadband plasmonic optical manipulation[64–66], including realization of multiband antennas[67], bio/chemical sensors[68], solar cells[64], and photodetectors.[69] Further, plasmonic fractals can be used to observe SERS[16,70,71] by exploiting its strong near-field enhancement. Different self-similar geometries, including Vicsek fractal[72], fractal-like films and clusters[73–76], and Cayley tree[77] have been previously studied.

In SC fractals, a tunable broadband spectral response by controlling the degree of fractal complexity has been theoretically investigated by Giorgio Volpe et al.[65] Subdiffraction limited focusing in such structures and its potential use for optical trapping of nano objects has also been studied.

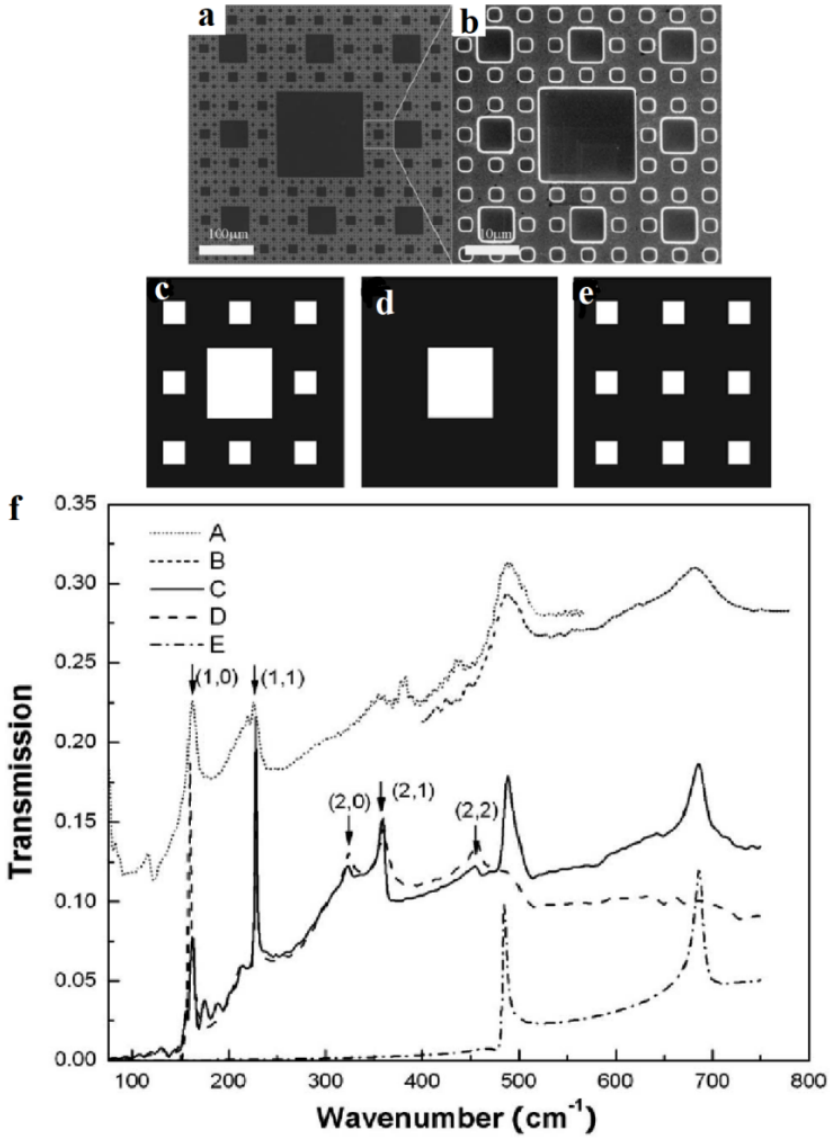

Fig 2.9: a) SEM micrograph of an Al thin film perforated with SC with four iterative generations on Si wafer. Scale bar = 100 μm. **b)** SEM micrograph of the marked region in (a). Scale bar = 10 μm. **c)** One iteration SC pattern made of square apertures of 2 μm and 6 μm in size. **d)** 6 μm square aperture. **e)** Array of 2 μm square apertures. The transmission spectra of structures c, d, and e are shown by curves C, D and E in Fig (f). **f)** Transmission spectra of SC structures. Curves A and B are experimental spectra obtained from FTIR covering different wavelength ranges. C, D, E are spectra obtained from FDTD simulations [Adapted from Ref. 78].

Bao et al. investigated Al Sierpinski carpet fractal structure fabricated using electron beam lithography (EBL) on Si wafer. The SC fractal viewed by field emission scanning electron microscopy is shown in Fig 2.9a, whereas the geometry used for the simulations is

represented in Fig 2.9c-e. The transmission spectra measured by FTIR spectrometer with normal incidence and as obtained from finite difference-time-domain simulations are shown in Fig 2.9f. Plots A and B are the transmission spectra of the four iterative generations of the SC measured by two spectrometers at different wave bands. The peaks at 161.99 cm^{-1}, 225.63 cm^{-1}, 487.90 cm^{-1}, and 682.68 cm^{-1} can be identified. Plot C corresponds to the resonance of one iteration SC aperture array, plot D corresponds to the resonance of 6 μm square aperture array, and plot E corresponds to the resonance of 2 μm square aperture array. The resonance modes are indexed as (*i, j*) where *i* and *j* are integers and the wave number of SPP-mediated resonances are approximately expressed as[79] $\nu_{max}(i,j) = \frac{\sqrt{i^2+j^2}}{a_0 n_{eff}}$; where a_0 is the lattice parameter, and n_{eff} is the real part of the effective refractive index of the perforated film.

It is worth noting that up to date, SC fractals have been experimentally studied mainly in the far-IR range[78,80] while at optical frequencies they have been scarcely investigated computationally[64,65], and experimentally[67] up to only the third order of complexity.

2.3 Fundamentals of graphene

Graphene is a single two-dimensional (2D) layer of carbon atoms bound in a hexagonal lattice structure. Theoretical study of graphene dates back to 1947, when Wallace[81] first calculated the electronic band structure of graphene and highlighted its linear dispersion near the K-point of the Brillouin zone. Isolation of such a 2D crystal was considered to be impossible being thermodynamically unstable.[82,83] Breakthrough was made in 2004, when researchers at University of Manchester unambiguously demonstrated isolation of single-layer graphene from bulk graphite using a simple scotch tape method.[3] This has sparked rapid researches in graphene, leading to discovery of novel characteristics of the material, including its excellent electrical, mechanical, thermal and optical properties. As mentioned, the quasiparticles in graphene are massless Dirac fermions with linear energy dispersion.[84,85] This remarkable property leads to observation of certain relativistic effects in graphene, such as anomalous quantum Hall effect[86,87] which shows conductivity plateaus at half-integer positions, and Klein tunneling[88,89] where complete transmission can be realized over high and wide potential barriers. Despite of its one-atom thickness, graphene shows outstanding mechanical properties with a breaking strength ~ 42 N/m, which is ~ 100 times larger than that of a hypothetical steel film of the same thickness.[90] In the following sections, fundamentals of graphene are explained, followed by graphene plasmonics. Finally, major techniques employed for graphene production are also outlined.

2.3.1 Structural properties

Graphene is a two-dimensional allotrope of carbon, which is formed of sp^2-bonded carbon atoms packed in a hexagonal lattice.[91] The carbon atom, with an electronic configuration $1s^2\ 2s^2\ 2p^2$, has four valence electrons determining the solid-state properties of carbon structures. The unit cell of the graphene lattice hosts six carbon atoms, each of them forming three bonds with each of its nearest neighbors.

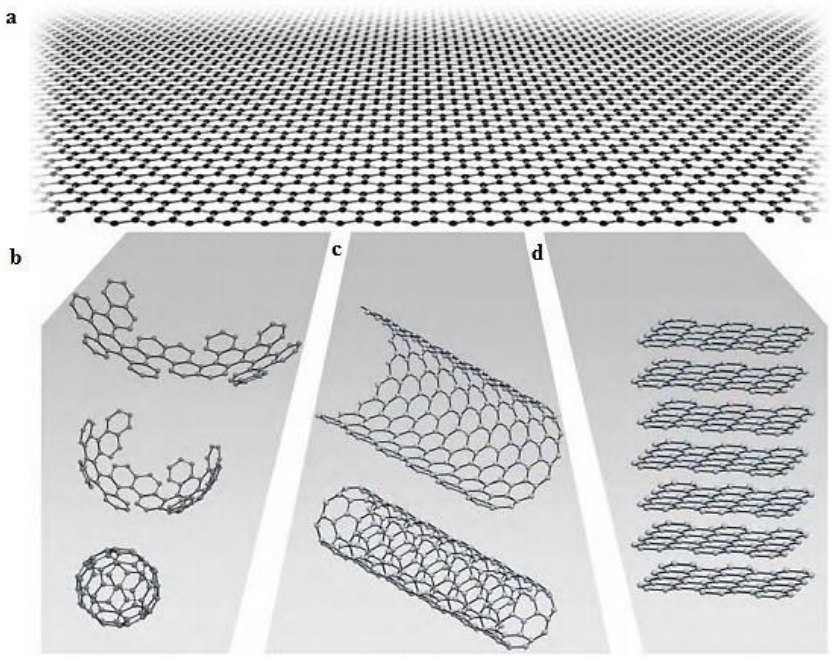

Fig 2.10: Graphene **(a)** is the 2D building material for carbon materials of all other dimensionalities: It can be wrapped up into 0 D buckyballs **(b)** rolled into 1D nanotubes **(c)** or stacked into 3D graphite **(d)** [Adapted from Ref. 4].

These are known as σ bonds and are formed when one 2s orbital is mixed with two of the 2p orbitals. This process is called sp^2 hybridization which gives graphene its mechanical strength.[90] The bond angle between the C–C bonds is 120^0 and the bond length is 0.142 nm. The 4^{th} valence electron in the dangling $2p_z$ orbital does not contribute to covalent bond

formation and forms a molecular orbital, which is responsible for the remarkable electronic and thermal conductivity of graphene.[92]

Electronic properties and the band structure of graphene was first theoretically studied by Wallace[81], who investigated its behavior as a semimetal using tight-binding approximation. In order to explain the electronic properties of graphene, it is necessary to provide a brief description about the band structure and the energy spectrum. Figure 2.11 shows the crystal structure of graphene containing two stacked carbon atoms A and B separated by a distance $a \sim 1.42$ Å [Ref. 85]. The primitive transitional vectors of the graphene hexagonal lattice are given by[85]:

$$\vec{a}_1 = \frac{a}{2}(3, \sqrt{3}) \quad \text{and} \quad \vec{a}_2 = \frac{a}{2}(3, -\sqrt{3}) \tag{2.16}$$

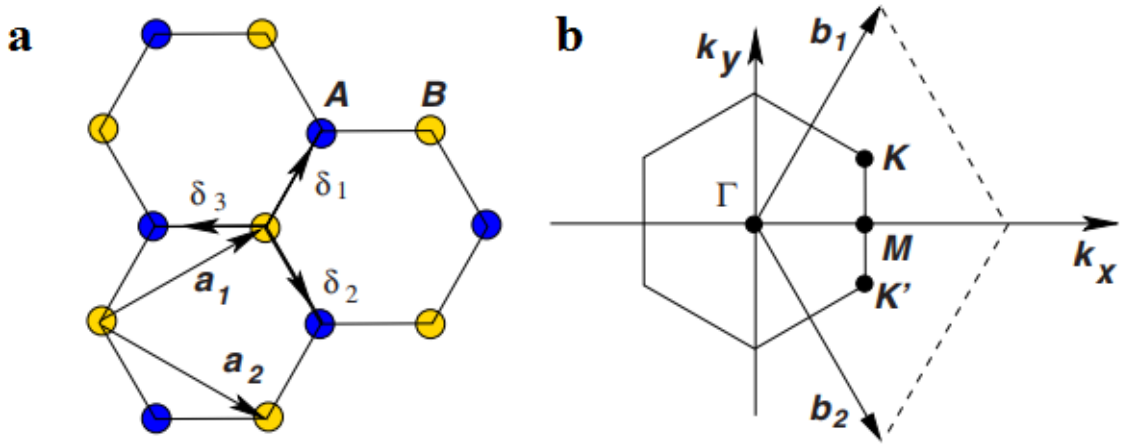

Fig 2.11: Graphene crystalline lattice and its Brillouin zone. **a)** Lattice structure of graphene, made out of two stacked hexagonal lattices (a_1 and a_2 are the lattice unit vectors, and δ_i are the nearest-neighbor vectors; i = 1, 2, 3). **b)** Corresponding Brillouin zone [Adapted from Ref. 85].

The vectors a_1 and a_2 are the basis of the lattice vector with modulus $\sqrt{3}a$~2.46Å. The reciprocal-lattice vectors are[85]:

$$\vec{b}_1 = \frac{2\pi}{3a}(1, \sqrt{3}) \quad \text{and} \quad \vec{b}_2 = \frac{2\pi}{3a}(1, -\sqrt{3}) \tag{2.17}$$

Two points at the corners of graphene Brillouin zone, K and K', named Dirac points are characterized by positions in momentum space[85]:

$$\boldsymbol{K} = \left(\frac{2\pi}{3a}, \frac{2\pi}{3\sqrt{3}a}\right) \quad \text{and} \quad \boldsymbol{K'} = \left(\frac{2\pi}{3a}, \frac{-2\pi}{3\sqrt{3}a}\right) \tag{2.18}$$

The two-dimensional energy dispersion relations can be calculated by solving the eigenvalue problem for the Hamiltonian associated with two stacked carbon atoms in the graphene unit cell. The solution obtained from the tight-binding approximation[22] including only the first-nearest-neighbor carbon-carbon interactions of π-orbitals of a single graphene sheet is[85]:

$$E_g^{\pm}(k) = \pm t\sqrt{1 + 4cos\left(\frac{\sqrt{3}k_x a}{2}\right)cos\left(\frac{k_y a}{2}\right) + 4cos^2\left(\frac{\sqrt{3}k_y a}{2}\right)} \tag{2.19}$$

where $E_g^+(k)$ and $E_g^-(k)$ correspond to the π* and π energy bands respectively. t is tight-binding hopping parameter (t ~ 2.8 eV)[85], and $\vec{k} = (k_x, k_y)$ denotes the 2D wavevector components along x and y directions. Figure 2.12 shows the energy spectrum of graphene as a function of k in the hexagonal Brillouin zone, where band crossing occurs at the K and K′ points. This clearly demonstrates the important feature of graphene dispersion relation:

the existence of a linear electronic spectrum around the Fermi energy at the K point. This means the electrons in graphene behave as massless particles like photons or neutrinos.[84,85]

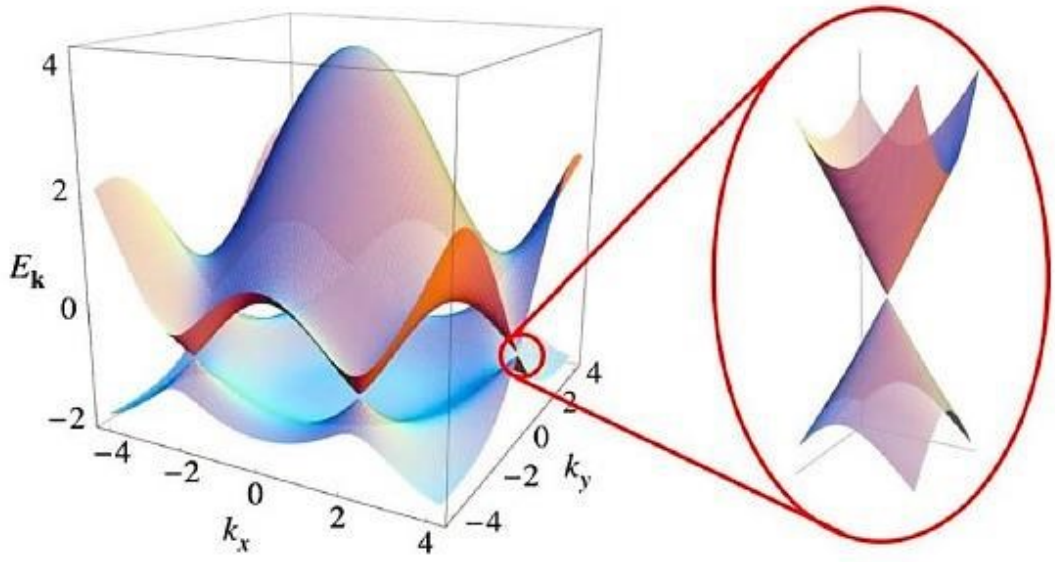

Fig 2.12: Electronic dispersion in the honeycomb lattice and detail of the linearly dispersing energy bands at one of the Dirac points [Adapted from Ref. 85].

The electronic dispersion of graphene near the vertices of the hexagonal Brillouin zone can be approximated as: $E_g^{\pm}(k) = \pm\hbar v_f \left|\vec{k}\right|$ where ħ is the Planck's constant (h) divided by 2π, v_f is the Fermi velocity given by $v_f \approx c/300 \approx 10^6 ms^{-1}$ (c is the velocity of light in vacuum) and $\overrightarrow{k}$ is the wavevector.

2.3.2 Electrical properties

Extremely high room-temperature mobility of charge carriers observed in graphene makes it a highly desirable material for electronic applications.[93,94] Graphene sandwiched between hexagonal boron-nitride (hBN) flakes shows mobility values as high as $\mu \sim 10^5$ cm^2/Vs at room temperature and at a carrier density $n \sim 10^{11}$ cm^{-2} [Ref. 95]. Electrons in such system are free to move with low interaction with the lattice.[94] Note that conventional semiconductors such as Si, exhibit a room-temperature charge carrier mobility for electrons[96] of around $\mu \sim 1400$ cm^2/Vs at the intrinsic charge carrier density $n \sim 10^{10}$ cm^{-2}.

Graphene is a zero bandgap semiconductor, as the conduction and valence bands touch at the Dirac points.[97] A graphene field-effect transistor (FET) shows ambipolar characteristics and a low ON/OFF ratio.[97] Figure 2.13a displays schematic of a graphene FET with SiO_2 dielectric and a p-doped Si backgate. A typical transfer characteristic of the device is represented in Fig 2.13b and schematic of the band energy diagram showing the Fermi level for electron, hole, and minimum conductivity zones is shown in Fig 2.13c. Due to non-uniformities and impurities in graphene, presence of electrical charges, thermal fluctuations etc., there is always a minimum residual charge carrier concentration in any graphene device despite tuning by gate.[3,97] As shown in Fig 2.13c, gate voltage at minimum conductivity is referred to as charge neutrality point voltage (V_{CNP}), which corresponds to having the Fermi level at the Dirac point.

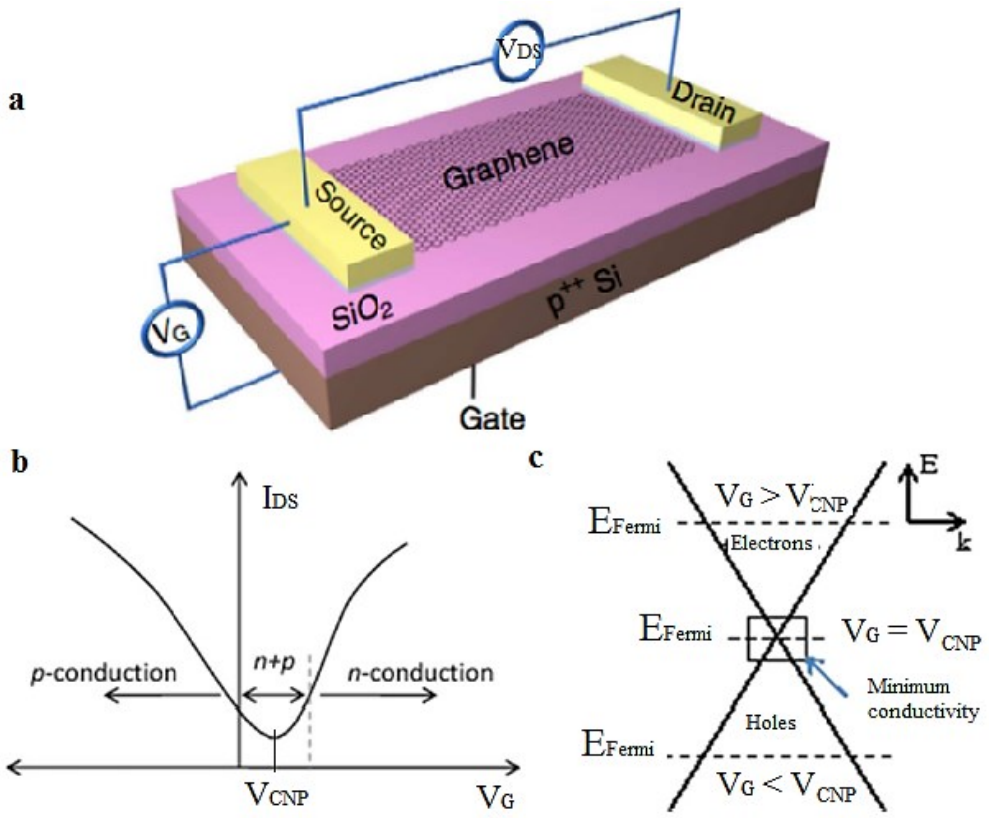

Fig 2.13: a) Schematic of a graphene FET. **b)** Typical transfer characteristics. **c)** Band energy diagram [Adapted from Ref. 97].

For $V_G > V_{CNP}$, the Fermi level is in the conduction band and the right side of I–V in Fig 2.13b is due to conduction of electrons, while for $V_G < V_{CNP}$, the Fermi level is in the valence band and left side of I–V in Fig 2.13b is due to conduction of holes. Despite of its high carrier mobility and tunability, the lack of a bandgap in graphene restricts its application in digital electronics. One technique to introduce a bandgap in graphene is by quantum confinement, such as those obtained in graphene nanoribbons[98], which will be explained in the following sections.

2.3.3 Optical properties

Since its discovery, one of the most interesting properties of graphene that has attracted researchers is its visibility with naked eye when it is deposited on a Si/SiO_2 substrate, despite of being a single atom-thick layer.[89] Graphene exhibits uniform optical absorption spectrum in the visible frequencies given by $\pi\alpha \sim 2.3\%$ [Refs. 89,99], where $\alpha = \frac{e^2}{\hbar c} = \frac{1}{137}$ is the fine structure constant (See Fig 2.14). This shows that the absorbance of graphene depends only on the fine structure constant and it is independent on the details of the band structure as well as the photon energy of the incoming light.

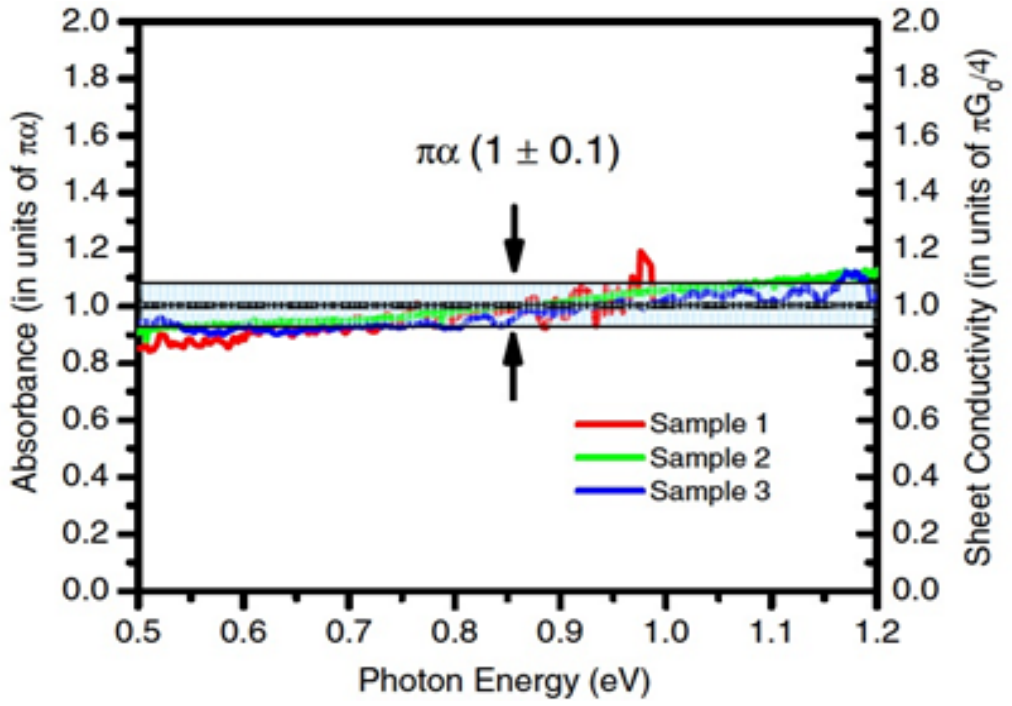

Fig 2.14: Absorption spectra for 3 different graphene samples over the range of photon energies between 0.5 eV and 1.2 eV. Left scale shows absorbance in units of πα, while the right scale gives corresponding optical sheet conductivity in units of $\pi G_0/4 = 6.08\times10^{-5}$S. The black horizontal line corresponds to the universal result of an absorbance of $\pi\alpha = 2.293\%$ with a range indicated of approximately ± 0.2% [Adapted from Ref. 100].

The excellent transmission given by T ≈ 1- $\pi\alpha$ has drawn considerable attention towards the development of transparent electrodes using graphene.[101] The experimentally reported absorption spectra for three different graphene samples over the spectral range of 0.5 - 1.2 eV is shown in Fig 2.14. The absorption follows the predicted uniform absorption for graphene with small deviations. The above simple approximation is expected for undoped samples at zero temperatures. Doping causes strong deviations in the optical properties.

The optical properties of graphene can be analytically expressed in terms of optical conductivity derived under the Random Phase Approximation (RPA):[6]

$$\sigma(\omega) = \frac{2ie^2T}{\pi\hbar(\omega + i\tau^{-1})}\log\left[2\cosh\left(\frac{E_F}{2k_BT}\right)\right]$$

$$+\frac{e^2}{4\hbar}\left[H(\omega/2) + \frac{4i\omega}{\pi}\int_0^\infty d\varepsilon \frac{H(\varepsilon)-H(\omega/2)}{\omega^2-4\varepsilon^2}\right] \qquad (2.20)$$

$$\text{Where } H(\varepsilon) = \frac{\sinh(\hbar\varepsilon/k_BT)}{\cosh(E_F/k_BT)+\cosh(\hbar\varepsilon/k_BT)}$$

Here ω is the radian frequency and τ is the relaxation time $\tau = \mu E_F/e\nu_F^2$ where v_f is the Fermi velocity and μ is the carrier mobility of graphene. The Fermi level is linked to the carrier concentration by $E_F = \hbar\nu_F\sqrt{\pi n}$. The first term of equation 2.20 is attributed to the intraband transitions, which represents the free carrier response of graphene, and the second term to the interband transitions. In the THz and mid-infrared (MIR) frequencies where the photon energy is below the double Fermi level ($\hbar\omega \ll 2|E_F|$), graphene optical conductivity is dominated by intraband transitions while the interband transitions are forbidden due to Pauli blocking.[6,102,103] On contrary, when $\hbar\omega > 2|E_F|$, interband

transitions are allowed and photons are absorbed by the promotion of an electron from valence to conduction band, which is responsible for the aforementioned universal absorption in graphene.[89,99] Figure 2.15 shows relative contributions of interband and intraband transitions to optical response of graphene as obtained from RPA calculations.[103]

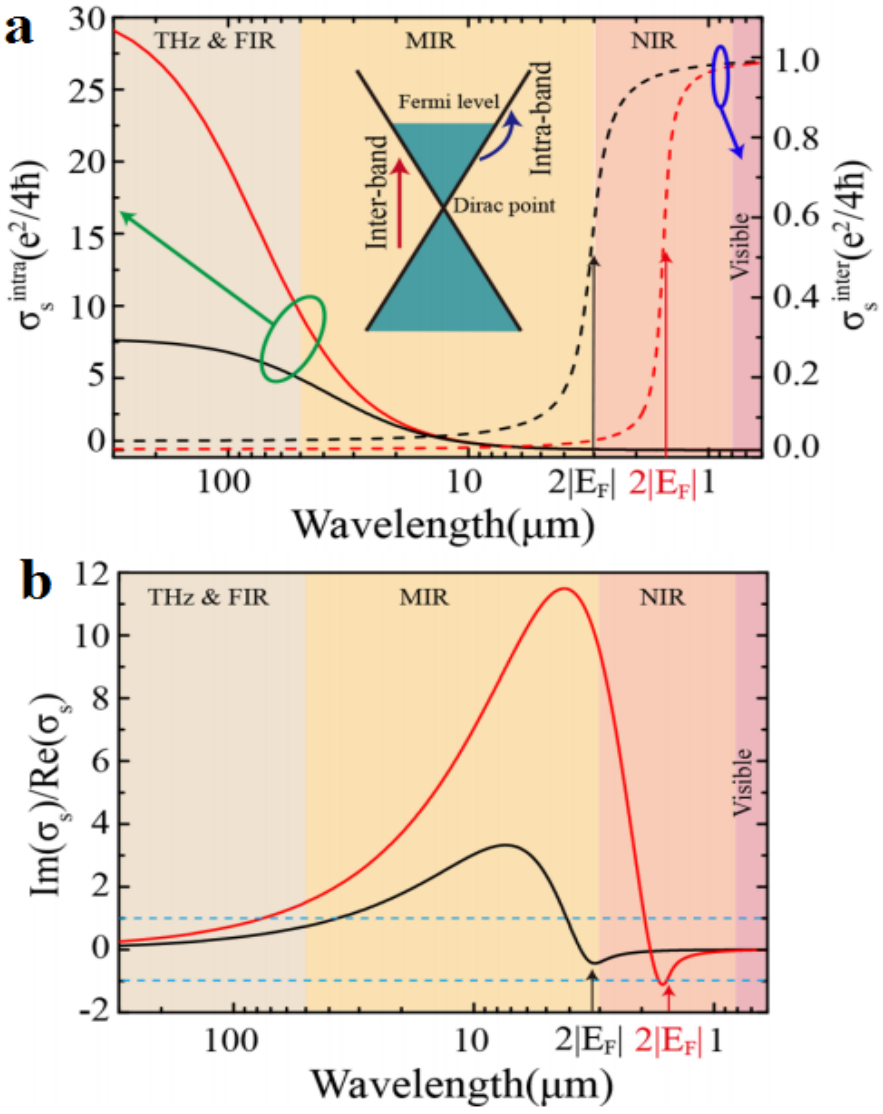

Fig 2.15: a) Real parts of intraband (solid) and interband (dash) surface conductivities of graphene with E_F = 0.2 eV (black) and E_F = 0.4 eV (red). The carrier mobility is assumed to be μ = 1000 cm^2/Vs. Inset shows the band structure of graphene. **b)** The optical response of moderately doped graphene. In the THz, Near-IR or MIR frequencies, graphene exhibits a lossy ($|Im(\sigma_s)/Re(\sigma_s) < 1|$) or plasmonic behavior ($Im(\sigma_s)/Re(\sigma_s) > 1$), respectively [Ref. 103].

2.3.4 Graphene plasmonics

Noble metals are considered to be attractive candidates for plasmonic applications owing to relative ease of synthesis, fine control over size, shape and surface properties, and their plasmon resonance peak typically in the visible region of the electromagnetic spectrum.[2,104] However, the large energy losses and poor tunability set a major drawback for plasmonics with noble metals. In contrast, plasmons in graphene has attracted growing attention due to low losses, high confinement, long life time and great tunability by gating or doping.[8,105–108] This part elaborates the fundamental theory of graphene plasmonics.

Pioneering theoretical investigations in graphene showed a √q dependency of the plasmon frequency (q is the wavevector) resembling normal 2-dimensional electron gas system (2DEG) plasmons, but exhibiting a scaling density $\omega_{pl} \propto n^{1/4}$ instead of $\omega_{pl} \propto n^{1/2}$ in conventional 2DEG[90,109]; where *n* is the carrier density. Plasmon dispersion in a 2DEG can be explained in the long wavelength limit ($q \ll k_F$; $k_F = \sqrt{n\pi}$ being Fermi wave vector) by the linearized Euler equation of motion:[7]

$$\frac{\partial \mathbf{j}(\mathbf{r},t)}{\partial t} = -\frac{D}{\pi e^2}\nabla_r \int d^2\mathbf{r}' \frac{e^2}{\varepsilon|\mathbf{r}-\mathbf{r}'|}\delta n(\mathbf{r}',t) \qquad (2.21)$$

Where $\delta n(\mathbf{r},t)$ is the deviation of electron density from its average value, $\partial \mathbf{j}(\mathbf{r},t)$ is the associated current density, and ε is the dielectric constant of the medium. The continuum-model Hamiltonian describing the electron gas at low energies is given by:[7]

$$\widehat{H} = v_f \sum_i \sigma.\,\mathrm{p_i} + \frac{1}{2}\sum_{i\neq j}\frac{e^2}{\varepsilon|\mathbf{r_i}-\mathbf{r_j}|'} \qquad (2.22)$$

Combining equations 2.21 and 2.22 yields the following expression for the Fourier component of $\delta n(\mathbf{r}, t)$:

$$\delta n(\mathbf{q}, \omega)\left[\omega^2 - \frac{D}{\pi e^2} q^2 u_q\right] = 0 \qquad (2.23)$$

Where D is the Drude weight, $u(r_{ij}) = u(|\mathbf{r_i} - \mathbf{r_j}|)$ is the potential due to the pairwise interactions of electrons, which depends on absolute value of the relative distance $\mathbf{r}_{ij} = \mathbf{r_i} - \mathbf{r_j}$ between them. $\mathbf{p}_i$ and σ are the canonical momentum of the i^{th} electron and 2D vector of the Pauli matrices respectively.

$$p_i = -i\hbar\nabla_{\mathbf{r}_i} \text{ and } \sigma = (\sigma_x, \sigma_y) \qquad (2.24)$$

Plasmon frequency as deduced from the above equations in terms of Drude weight is given by:

$$\omega_{pl}(q) = \sqrt{\frac{2Dq}{\varepsilon}} \Rightarrow \omega_{pl}(q) \propto \sqrt{q} \qquad (2.25)$$

For ordinary Schrödinger fermions with mass m^*, $D = \pi e^2 n/m^*$. Hence equation 2.25 becomes:

$$\omega_{pl}(q) = \sqrt{\frac{2\pi e^2 nq}{\varepsilon m^*}} \qquad (2.26)$$

Above equations are formulated in the framework of Galilean-invariant interacting electron model which is valid for many semiconductors and semiconductor hetero-junction systems

and is obtained by replacing m^* by effective band mass m_b and e^2 by e^2/ε in the classical formula, in the long wavelength limit.

The situation is quite different in graphene, as the broken Galilean invariance results in large many-body effects on the plasmon dispersion and the Massless Dirac-Fermions have a Drude weight given by[110] $D_{MDF} = 4E_F\sigma_{uni}/\hbar$, where $\sigma_{uni} = \pi e^2/2h$ is the universal optical conductivity of graphene. Thus, the equation for plasmon frequency in doped graphene in long wavelength limit is:

$$\omega_{pl}(q) = \sqrt{\frac{8E_F\sigma_{uni}q}{\varepsilon\hbar}} \qquad (2.27)$$

Which results in the scaling, $\sqrt{E_F} \propto n^{1/4}$. A remarkable conclusion from equation 2.27 is the compression of surface plasmon wavelength (λ_{pl}) relative to the excitation wavelength (λ_0), which is governed by the fine-structure constant as:

$$\frac{\lambda_{pl}}{\lambda_0} \approx \frac{2\alpha E_F}{\varepsilon\hbar\omega} \sim \alpha \qquad (2.28)$$

This property of strong confinement of graphene plasmons can be used to tailor extremely strong light-matter interactions at a quantum level.[6] Typical plasmon frequencies in graphene reside in the MIR regime of the electromagnetic spectrum, assuming an electron concentration of 1×10^{13} cm^{-2}.

The semi-classical approach described above is valid when the system is sufficiently below the interband threshold. When $q \approx k_F$, a fully quantum mechanical model is

necessary[109,111,112], in which the relaxation time τ is introduced to take into account the losses due to electron-impurity, electron-defect, and electron-phonon scattering. The collision-less RPA describes the case when[109] $\tau \to \infty$ while the RPA-RT (relaxation time) approximation can be applied for finite[113] τ.

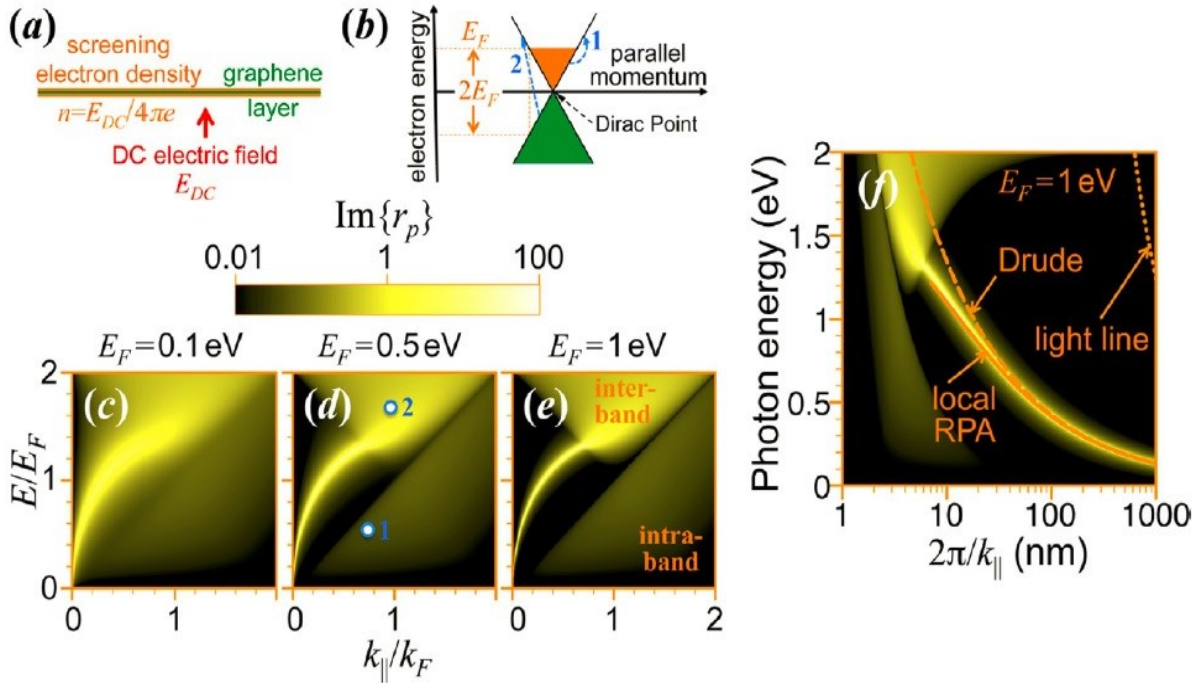

Figure 2.16: Electrostatic doping and plasmon dispersion relation in graphene. **a)** An applied DC electric-field induces doping charges on the graphene. **b)** A doping charge density *n* raises the Fermi level to $E_F = \hbar v_F k_F$. Consequently, a gap is opened of size $2E_F$ for vertical transitions. **c–e)** this optical gap closes down for parallel wave vector transfers $k_\parallel \geq k_F$ and a plasmon mode is allowed to exist free from Landau damping in the remaining $k_\parallel < k_F$ region. Here the gap and the plasmon are visualized by representing the $k_\parallel - \omega$ dependence of the loss function $\mathrm{Im}\{r_p\}$ for 3 different levels of doping in free-standing graphene. Two specific intraband (1) and interband (2) transitions are shown in (d), corresponding to the dashed arrows in (b). **f)** Same as (e), but represented as a function of in-plane wavelength $2\pi/k_\parallel$ instead of parallel wave vector $k_\parallel$. The light line (dotted curve) and the plasmon dispersion relations in the Drude (dashed curve) and local-RPA (solid curve) models are also shown [Adapted from Ref. 105].

Injection of charge carriers in graphene results in the shift of Fermi energy to $E_F = \hbar v_F \sqrt{n\pi}$. Typically, electrical gating can produce $E_F \sim 1$ eV, which corresponds to $n \sim 7 \times 10^{13}$ cm^{-2} [Ref. 114]. An immediate consequence of doping is the opening of an optical gap of size $2E_F$ for vertical transitions as shown in Fig 2.16b. The density plots of Fig 2.16 are calculated using full RPA conductivity for graphene with mobility $\mu = 2000$ cm^2/Vs. The function Im $\{r_p\}$ whose variation with E_F is shown in Fig 2.16c-f accounts for the energy-loss probability when the graphene is excited by a fast electron.[115] The difficulty in coupling graphene plasmons to propagating light requires to employ complex near-field techniques or patterning graphene into micro/nanoscale arrays for far-field coupling which will be described in detail in the following section.

2.3.5 Graphene micro/nanostructures

Graphene supports plasmons in a broad frequency range from MIR to the THz regime and they can be tuned in situ through the modulation of the carrier density by electrostatic gating which is a significant advantage compared to plasmons in noble metals.[6] The surface plasmon polaritons (SPPs) can be excited in graphene by patterning it into different geometries such as graphene nano/ micro ribbons (GNR/GMR)[116–118] and disks[119,120], or using the apex of an illuminated nanoscale tip.[121,122] Chen et al.[121] has launched and detected propagating optical plasmons in tapered graphene nanostructures (Fig 2.17) using scattering-type scanning near-field optical microscopy (SNOM). The extracted plasmon wavelength was more than 40 times smaller than the wavelength of illumination, demonstrating an extraordinary confinement of graphene plasmons.

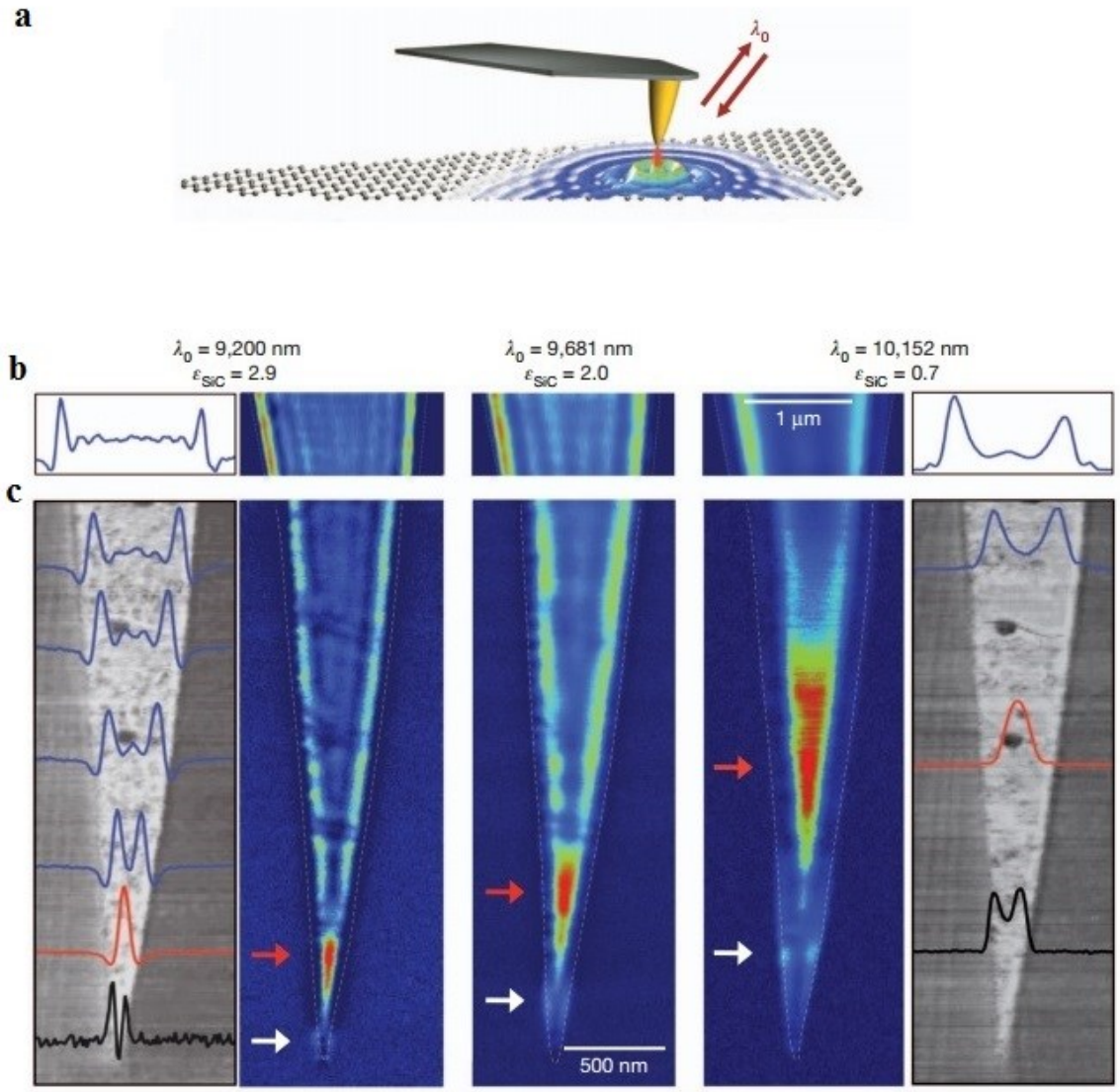

Fig 2.17: Optical imaging of graphene plasmons. **a)** Experimental configuration used to launch and detect propagating surface waves. The metallized AFM tip (yellow) is illuminated by an IR laser beam. **b)** Near-field optical images with wavelengths 9.2 μm, 9.681 μm and 10.15 μm. Corresponding dielectric constants of SiC are also shown. **c)** Images of a tapered graphene ribbon; both ribbons are on the same 6H-SiC substrate. The AFM obtained topography is shown in leftmost and rightmost panels, and outlined by dashed lines in the central colored panels. The line traces in the leftmost and rightmost panels are extracted from the near-field images for λ_0 = 9200nm and λ_0 = 10152nm. Red and white arrows indicate resonant localized modes [Adapted from Ref. 121].

Another pioneering study of plasmon excitations and light–plasmon coupling in graphene micro-ribbon arrays was reported by Ju et.al.[116] It was shown that plasmon excitations can be controlled by changing the width of the ribbons. The plasmon frequency scales as $W^{-1/2}$ where W is the micro-ribbon width.[116] Assuming the GMR/GNR as a stripe of a finite width W, the lowest quasistatic eigen-mode frequency is expected at $q \approx \pi/W$.[123] Authors tuned the plasmon resonance through electrical gating and by varying the ribbon width in GMRs fabricated using chemical vapor deposition (CVD), EBL and oxygen plasma etching. Figure 2.18 shows the tuning of graphene plasmon resonance characterized by FTIR over a wide THz range.

Hugen Yan et al.[118] demonstrated graphene plasmon resonances in the MIR regime by patterning graphene into nanostructures with dimensions as small as 50 nm. In contrast to their microstructure counterparts in which plasmon resonances lie in THz frequency range, the MIR plasmonic response has been found to be affected strongly by interactions with substrate phonons and intrinsic graphene optical phonons.[118] It was experimentally shown that the resonance peaks blue shift with decrease in GNR width. The electromagnetic responses are demonstrated through extinction spectra using a Fourier-transform IR spectrometer. Figure 2.19 shows the schematic diagram of the experiment, the SEM image, and the extinction spectra on silicon dioxide (SiO_2) substrate. T_{per} and T_{par} denote the transmission of the light through GNR array with the electric-field perpendicular and parallel to the ribbon respectively, and T_0 is the transmission through the substrate without graphene.

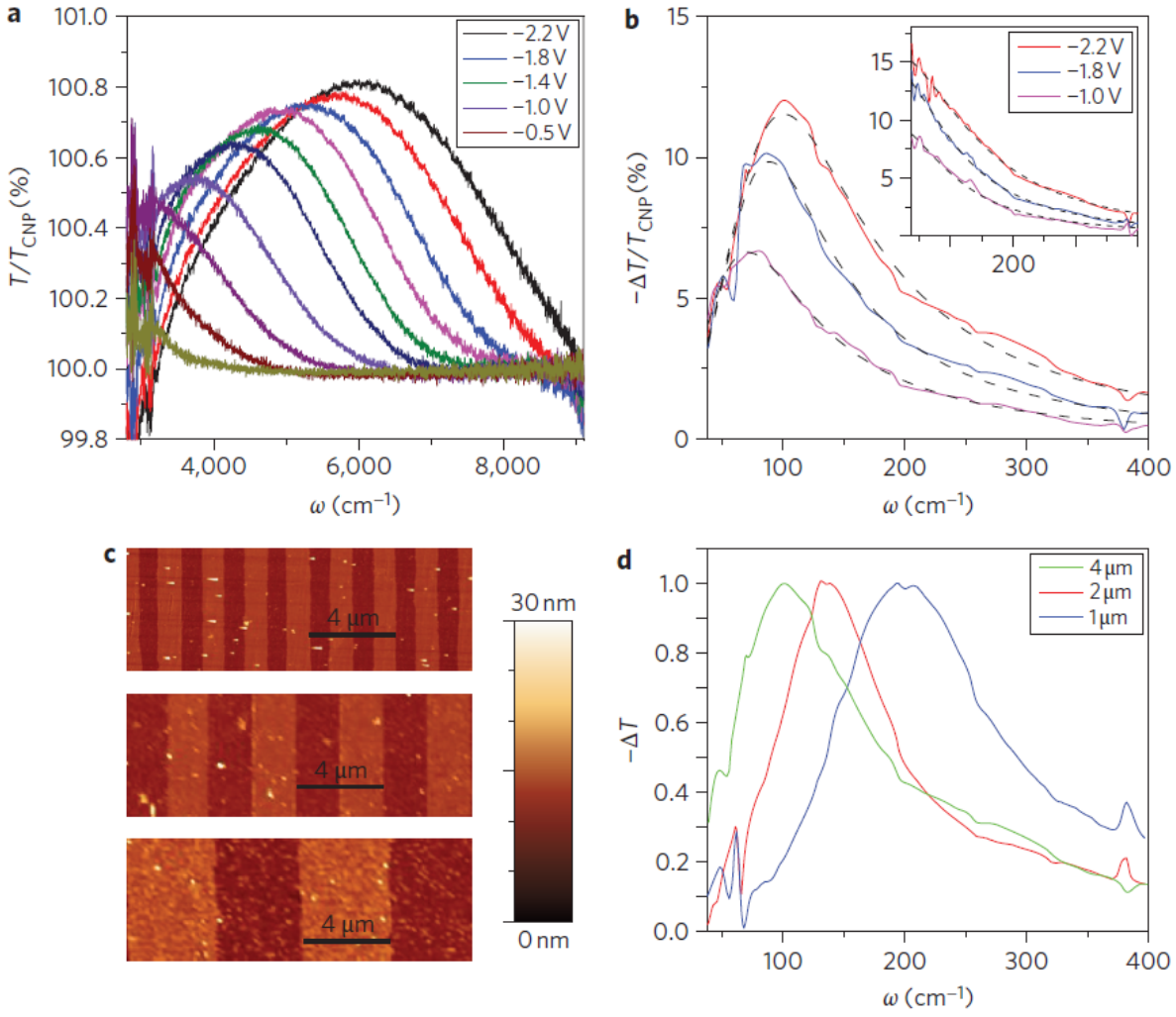

Fig 2.18: Control of plasmon resonance through electrical gating and micro-ribbon width. **a)** Transmission spectra of the graphene ribbon array (T/T_{CNP}) with varying gate voltage. The voltages corresponding to the unlabeled lines, starting with the red line and alternating downwards, are: -2.0 V, -1.6 V, -1.2 V, -0.7 V and -0.3 V. On electrical gating, optical transmission is increased up to a threshold energy of $2|E_F|$ due to blocked interband optical transitions. This provides direct determination of E_F and carrier concentration in gated graphene, $n = (|E_F|/\hbar v_F)^2/\pi$. **b)** Control of THz resonance of plasmon excitations through electrical gating. Radiation is polarized perpendicular to the graphene ribbons. The plasmon resonance shifts to higher energy and gains oscillator strength with increased carrier concentration. Inset shows corresponding spectra due to free carrier absorption for radiation polarized parallel to the ribbons. **c)** AFM images of samples with micro-ribbon widths 1, 2 and 4 μm. **d)** Transmission spectra corresponding to different ribbon widths with same doping concentration of 1.5×10^{13} cm^{-2}. Plasmon resonance frequency shifts from 3 to 6 THz when micro-ribbon width decreases from 4 to 1 μm [Ref. 116].

As a result of plasmon excitation, the extinction spectrum with perpendicular polarization shows prominent resonance peaks.[116,118,119] The existence of multiple resonances in Fig 2.19 is due to interactions of graphene plasmons with substrate phonons. These are Fuchs–Kliewer surface optical (SO) phonons and are well known in polar semiconductor surfaces.[124] SiO_2 being a polar substrate accommodates SO phonons and the long-range Frohlich coupling can mediate interactions with the electronic degrees of freedom in graphene including the collective plasmon modes.[125,126]

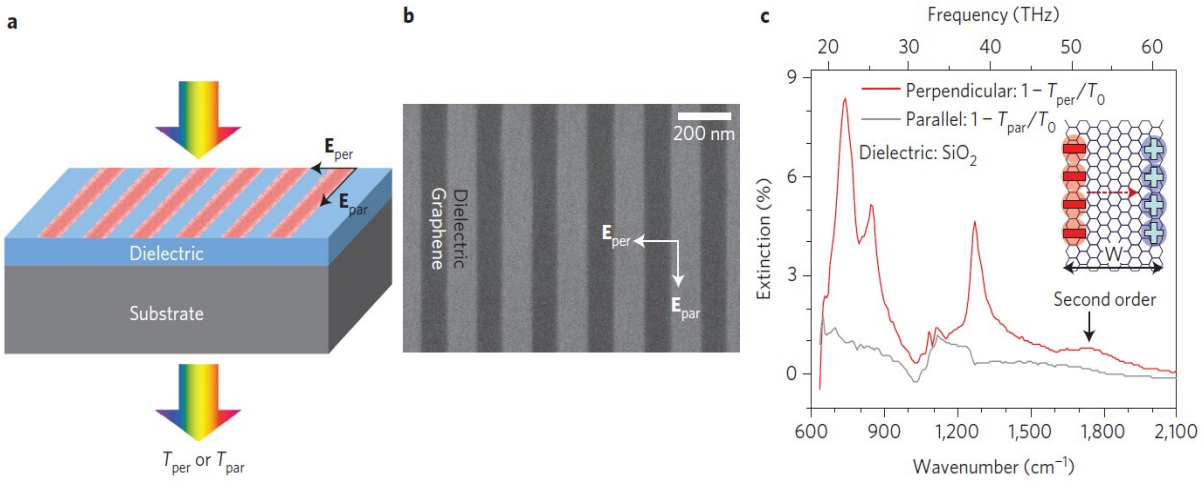

Fig 2.19: MIR transmission measurement scheme for graphene nanoribbons. **a)** Schematics of the experiment. **b)** SEM image of a typical array of graphene nanoribbons with ribbon width ~ 100 nm. **c)** Extinction spectra of a ribbon array on SiO_2 with the incident light polarization perpendicular (red) and parallel (grey) to the ribbons. Here the ribbon width is 240 nm. A weak second-order mode is indicated. Inset shows dipole oscillation in a graphene ribbon [Adapted from Ref. 118].

A simpler system with a nonpolar substrate such as diamond-like-carbon (DLC) allows one to observe only one prominent plasmon resonance peak in the extinction spectra as shown in Fig 2.20a. The inset to Fig 2.20a shows the extracted plasmon frequencies as a function of π/W, which does not match well with the simple scaling $W^{-1/2}$.

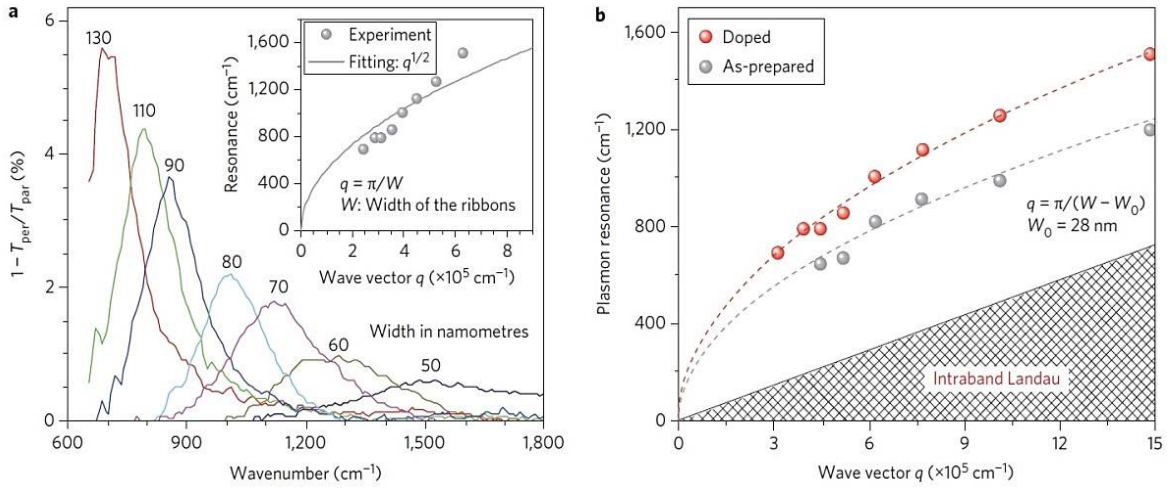

Fig 2.20: Plasmons in graphene nanoribbons on DLC. **a)** Extinction spectra (1 - T_{per} /T_{par}) of graphene ribbons on DLC substrate with different ribbon widths. The spectra were referenced using transmission of light with parallel polarization (T_{par}). Inset shows plasmon resonance frequency as a function of wave vector q = π/W, where W is the width of the nanoribbon. The grey curve is a fit according to $\nu_{pl} \approx \sqrt{q}$. **b)** The same plasmon resonance data (red dots) as in (a), plotted as a function of wave vector q = π/W_e, where W_e = W-W_0 is the effective ribbon width and W_0 is 28 nm. Plasmon resonance data for a lower Fermi level are also plotted (grey dots). Dashed curves are fits based on √q scaling. The shaded area is the intraband Landau damping region [Adapted from Ref. 118].

This disagreement is due to a discrepancy between electrical width and the physical width of the GNR as a result of rigorous fabrication method using EBL and oxygen plasma etching which induce atomic-scale defects and complicated edge chemistry.[127–129] An effective ribbon width W_e = W-W_0 is introduced to take into account the above effect. Fig 2.20b shows plasmon frequency as a function of $q = \pi / W_e$ which is in good agreement with the fit based on √q scaling.

2.3.6 Production techniques

Since graphene was first isolated[3] in 2004 by Geim and Novoselov using Scotch tape method, many processes have been developed to produce graphene of various dimensions, shapes and quality.[130] The research, development and market of graphene correlate with the advancement of appropriate production techniques for specific applications. Figure 2.21 summarizes some of the most common methods of graphene production in terms of quality, cost, scalability, purity, and yield.

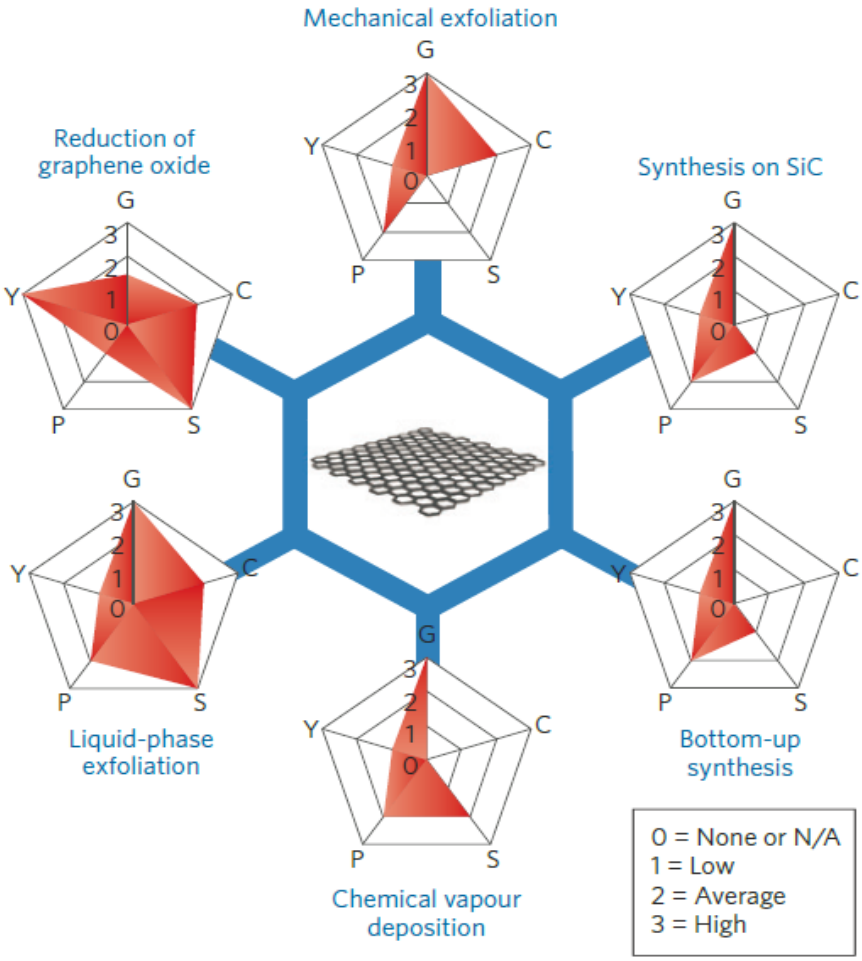

Fig 2.21: Most common graphene production methods. Each method has been evaluated in terms of graphene quality (G), cost aspect (C; a low value corresponds to high cost of production), scalability (S), purity (P) and yield (Y) of the overall production process [Adapted from Ref. 131].

The various production techniques can broadly be classified into top-down and bottom-up approaches. The former involves production of graphene by exfoliation from bulk graphite. Examples are micro-mechanical exfoliation (scotch tape method) and liquid phase exfoliation.[132] In the bottom up approach, synthesis and growth of graphene occurs atom by atom: CVD and molecular beam epitaxy (MBE) are major examples. In this thesis work, CVD grown graphene is used. For this reason, this technique will be described in detail while other techniques will be briefly reviewed in following sections.

2.3.6.1 Mechanical exfoliation

Developed by Geim and Novoselov[3,133] in 2004, the mechanical exfoliation yields monolayer and few-layers graphene with excellent quality that are well suited for fundamental research. The procedure is rather simple: an adhesive tape is used to peel off layers from the surface of graphite and repeated peeling eventually leads to single or few layers of graphite, which are then transferred onto a substrate, such as Si/SiO_2. Single layer graphene (SLG) of sizes up to 10 μm and few layer graphene (FLG) around 100μm are reported in the initial studies.[3] Even monolayers of graphene are visible under optical microscope due to its considerable absorption and optical interference contrast.[134] Mechanically exfoliated graphene samples are superior in terms of purity, defects and optoelectronic properties, and have mobilities up to 2×10^5 cm^2/Vs when sandwiched between hBN crystals on a Si/ SiO_2 substrate.[95] The limited size and yield of SLG sets a major drawback for mechanical exfoliation, hence development of new strategies for scalable and industrial production of graphene became a necessity. Figure 2.22 shows a mechanically exfoliated graphene sample.

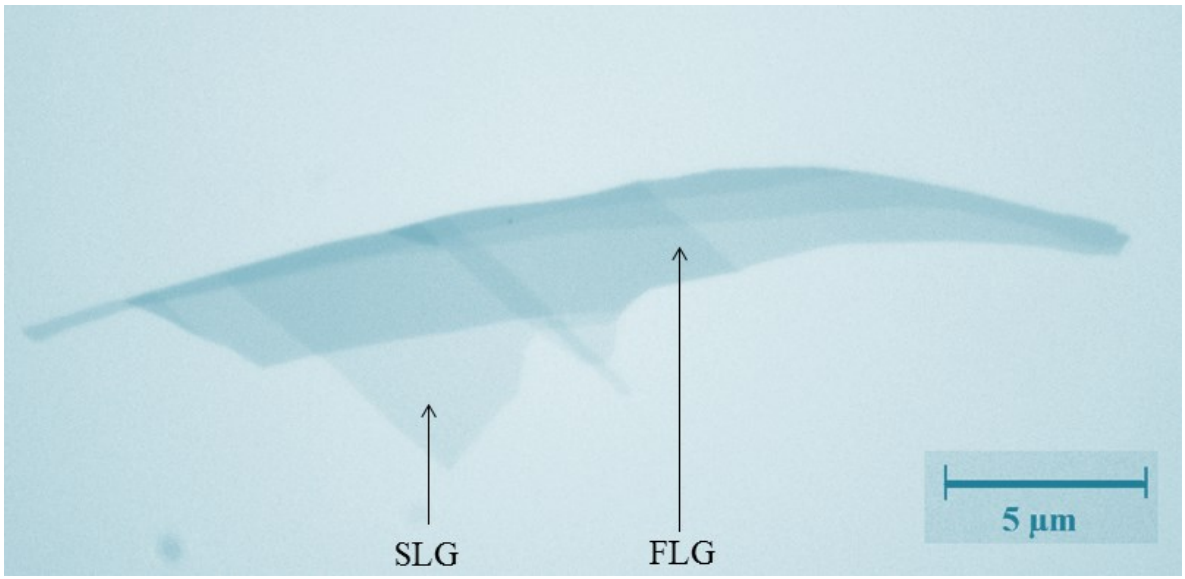

Fig 2.22: Optical image of mechanically exfoliated graphite in our lab, showing SLG and FLG on a Si/SiO_2 substrate.

2.3.6.2 Chemical Vapor Deposition

In the CVD method, carbon is supplied in gaseous form and a metal acts as both catalyst and substrate to grow the graphene layer. This allows growth of large-area uniform polycrystalline graphene films on transition metal films such as nickel and copper.[135]

The starting materials for CVD growth are an atomically flat surface of a transition metal substrate[136–141] which acts as a catalyst, and an appropriate carbon precursor. The substrate is placed in a furnace which is attached to a gas delivery system through which reactive gas enters the system. The gas flow rates are controlled with valves called mass flow controllers (MFCs). The precursor molecules (methane or ethylene) are brought into contact with the substrate at high temperature, typically up to ~ 1000 ^{0}C [Ref. 136]. Upon contact with the substrate, the molecules are broken to form carbon atoms which get

attached to the substrate. Graphene is formed when carbon atoms start forming bonds with each other. To complete the process, transfer of graphene from the copper substrate to desired substrate is required.[136,137] Main components of a typical CVD furnace are shown in Fig 2.23.

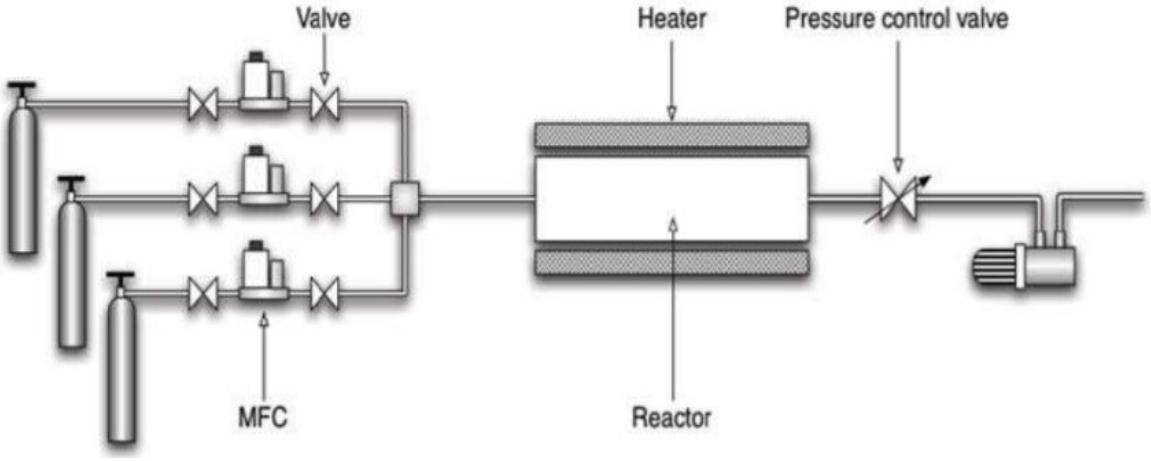

Fig 2.23: The schematic diagram of a typical tube-furnace CVD system [Adapted from Ref. 138].

Over the years, considerable research to optimize the process has been carried out, which triggered an interest in growth of graphene on Nickel[137,139,140] and Copper[136,141] substrates which are relatively inexpensive. Although graphene deposited on polycrystalline Nickel have been successfully transferred onto desired substrates using a PDMS stamp, they suffered from inhomogeneity over the entire substrate due to poor control over the number of layers.[137,140] CVD growth of graphene on Cu has shown to yield promising results thus allowing access to high-quality uniform SLG over large areas.[136] This is because the thickness of graphene layer is dominantly controlled by the solubility of carbon in the substrate and copper has lowest solubility compared to all other metals.[142] Graphene films with dimension as large as ~ 400 cm^2 was reported recently[143] on ultra-thin copper foils.

To summarize, CVD enables production of high quality, large-scale graphene and the major drawbacks are higher expenses compared to mechanical exfoliation and difficulties in simultaneous control of the domain (grain) size, ripples, doping level and the number of layers.[144]

2.3.6.3 Other methods

It has been shown that graphitic layers can be grown either on the 0001 (silicon-terminated) or $000\bar{1}$ (carbon terminated) faces of 4H- and 6H-Silicon Carbide (SiC) crystals by sublimating Si atoms, which leaves a graphitized surface.[145] The obtained graphene shows electrical properties comparable to that of mechanically-exfoliated graphene in terms of carrier mobilities and their Dirac nature.[146] Major drawbacks of epitaxial graphene from SiC include high cost of the SiC wafers, controlling the number of layers, repeatability of large area growths, interface effects with the SiC substrate, high temperatures required (1000 ^{0}C to 1500 ^{0}C) and requirement of ultra-high vacuum.[135]

Liquid phase exfoliation (LPE) is a top down synthesis which is suitable for industrial production and applications due to its scalable and cost effective nature.[130,132] Unlike most of the CVD techniques, LPE does not require transfer of graphene from a metal substrate. The general principle of LPE is weakening of the van der Waals interaction between the layers of graphite in a liquid environment.[130] A typical LPE involves dispersion of pristine graphite in a solvent such as N-methylpyrrolidone (NMP), followed by exfoliation of graphitic flakes assisted by ultrasonication.[147,148] The exfoliated graphene flakes can be further isolated from thicker un-exfoliated graphite stacks by means of centrifugation.[149]

LPE graphene is used for composites, smart windows, solar cells and some touch screen applications.[130,150]

2.4 Metal/graphene plasmonic structures

Noble metals have large carrier concentrations (10^{22} cm^{-3}) required to support SPR[2] and hence they have been widely used for plasmonics. However, exploiting the full potential of plasmonics in various applications demands the ability to dynamically modulate the plasmon resonance, which is hard to achieve in noble metals.[151] In contrast, graphene exhibits remarkably tunable surface plasmons and been extensively investigated and demonstrated in the MIR[121,152,153] and far-infrared[116,119] spectra. However, realization of tunable devices at VIS - near infrared (NIR) regime using graphene faces critical challenges due to the large interband loss of graphene.[154,155] More importantly, considerably weak light absorption in graphene (~ 2.3%)[156] restricts its applications in optoelectronic devices.[157]

In order to address above limitations, metal/graphene hybrid nanostructures have been introduced and widely explored in the past few years, demonstrating their potential applications in SERS[158–162], photodetectors[69,163–167] and biosensors.[168] Various metallic plasmonic structures such as nanoribbon[169], nanorod[170], dolmen structure[171] and nanovoid array[172] have been incorporated with graphene to realize such systems.

In a metal/graphene hybrid structure, the optical field near the graphene layer experiences significant enhancement due to the excitation of SP waves on the plasmonic structure, resulting in increased light absorption in graphene.[169] As the graphene itself is not patterned, the generated carriers can easily be transported in the extended plane without

being trapped. This also eliminates the presence of rough edges, generally introduced during the fabrication of graphene nanostructures using conventional lithographic processes followed by etching.[173]

Realization of hybrid devices provides means of tailoring the plasmon resonance of the metal nanostructure. An immediate consequence is red shift of resonance peak primarily due to its dependency on the dielectric function of the surrounding medium[174,175], which is graphene ($n_g \sim 2.4$ at 532 nm)[176]. For instance, Fig 2.24a shows plasmonic resonance wavelength and amplitude of 4 nm diameter Ag NPs on bare glass as well as on different number of graphene layers on glass. A red-shift in the resonance frequency is observed with added graphene layers.[175] Figure 2.24b depicts simulated quality factor values of Ag disks with 10 nm thickness and 40 nm diameter without graphene, with 0.7 nm graphene layer (bilayer), and with 2 nm graphene layer between the Ag disk and the glass substrate. It can be seen that the plasmonic resonance is dampened and broadened by the presence of graphene, which is attributed to energy transfer from Ag NPs to graphene, thus dissipating the localized electrical-field concentration on the surface of the Ag NPs.[175] It is worth noting that treating graphene as a mere dielectric environment for the metallic nanostructures does not fully grasp the physics of the hybrid systems, as the interactions involve more complex phenomena such as electron transfer[177] and enhanced photoexcitation due to plasmonic near-field effects.[178]

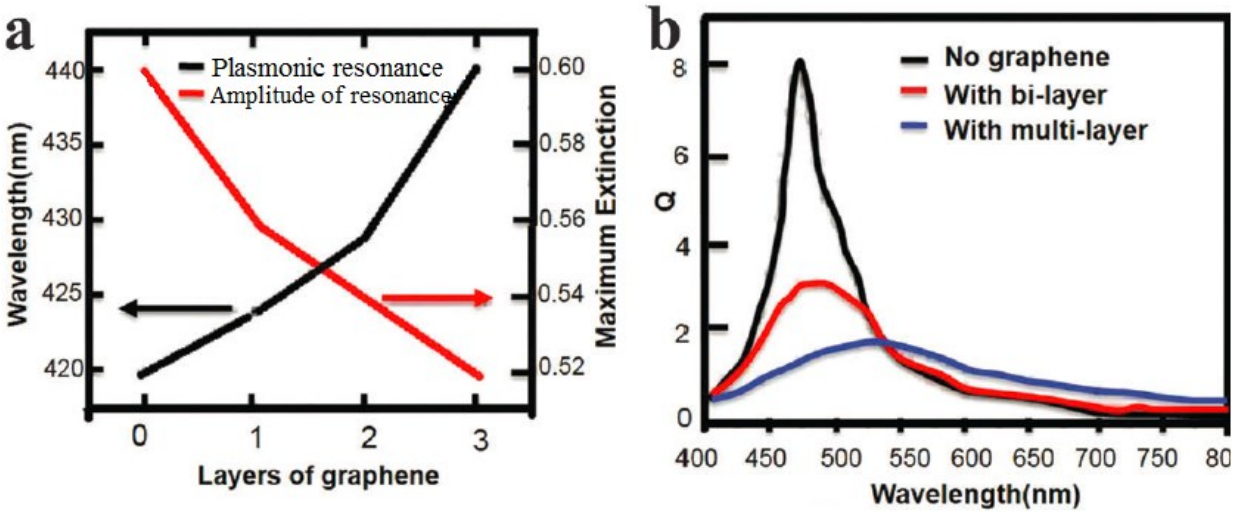

Fig 2.24: a) Plasmonic resonance frequency and amplitude of 4 nm Ag NPs for different number of graphene layers. **b)** Simulated Q-values of Ag disks with 10 nm thickness and 40 nm diameter without graphene, with 0.7 nm graphene layer, and with a 2 nm graphene layer [Adapted from Ref. 175].

Several studies have exploited the ability to electrostatically modulate carrier concentration in graphene[106,107,179] to achieve electrically tunable optical properties in a metal/graphene hybrid[170,171,180,181], paving a way towards next generation plasmonic and nanophotonic devices. Tunable resonance around the THz regime in metal/graphene system was first demonstrated using split-ring resonators on top of CVD graphene[182] as shown in Fig 2.25. Such devices exploit dependence of graphene surface conductivity on the Fermi level, which in turn can be controlled in-situ through applied gate voltage. In a graphene FET, the dependence of graphene Fermi energy E_F on the applied gate voltage is given by[183]:

$$E_F(V_G - V_{CNP}) = \hbar v_F \sqrt{\pi C_g (V_G - V_{CNP})} \qquad (2.29)$$

Where V_G is the applied gate voltage, V_{CNP} is the charge neutrality point voltage, v_F is the Fermi velocity and C_g is the capacitance per unit area per charge of the SiO_2 layer.

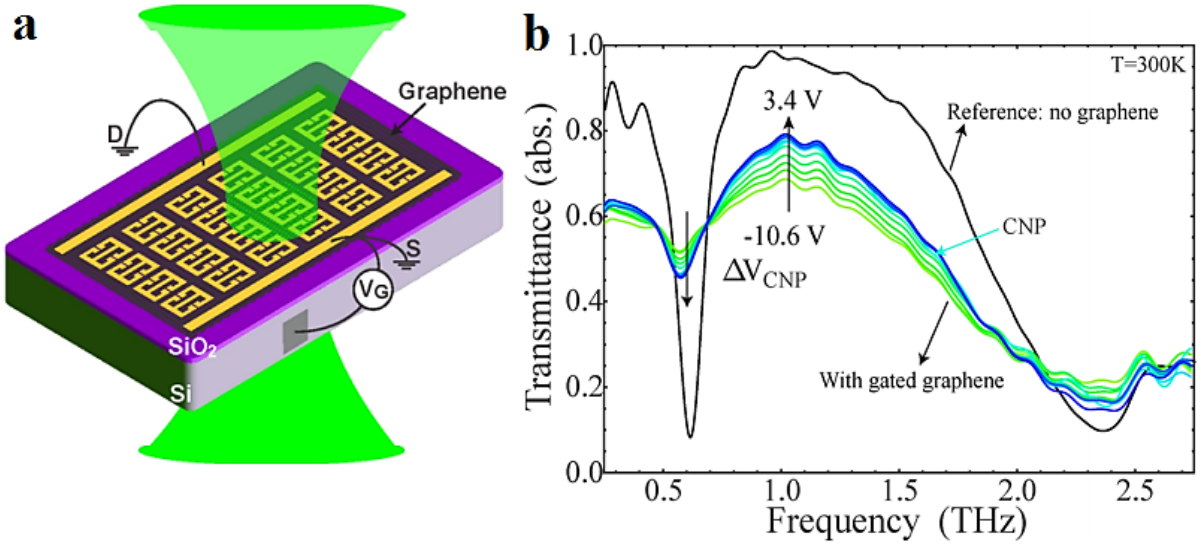

Fig 2.25: a) Schematic of gated CVD graphene/THz-metamaterial device. **b)** Room temperature transmittance spectra for back-gate voltages V_G = (0, 2, 4, 6, 8, 10, 11, 12, 13, 14) V, from green to blue with $\Delta V_{CNP} = V_G - V_{CNP}$ [Ref. 182].

Active control of the optical properties in the range 0.25 - 2.75 THz achieved in a graphene/THz metamaterial device is shown in Fig 2.25b. Presence of graphene has strongly changed the metamaterial transmittance over the whole frequency range and through graphene gating; a modulation depth of 11.5% with an applied bias of 10.6 V is obtained. Efficient control of plasmon resonance in the NIR was reported by Kim et al in a hybrid graphene-gold nanorod system[170], which is explained in detail in the following part. In the visible-range, SPP modulation was achieved by Quian et al.[184] by employing graphene-Ag nanowire hybrid structures.

Figures 2.26a,b display the effect of graphene on the optical properties of Au nanorod[170] and Fig 2.26c shows the effect of a gate voltage. The mechanism of interband optical transitions present at all energies in pristine graphene (d) and a gate-induced shift in Fermi energy which blocks the interband transition (e) are also shown. A typical SEM image of the device is shown in the inset to Fig 2.26a. As mentioned before, the presence of

graphene resulted in broadening of the Au nanorod plasmon resonance peak. Authors used a top electrolyte gate with ionic liquid to control plasmon resonance through varying optical transitions in graphene.

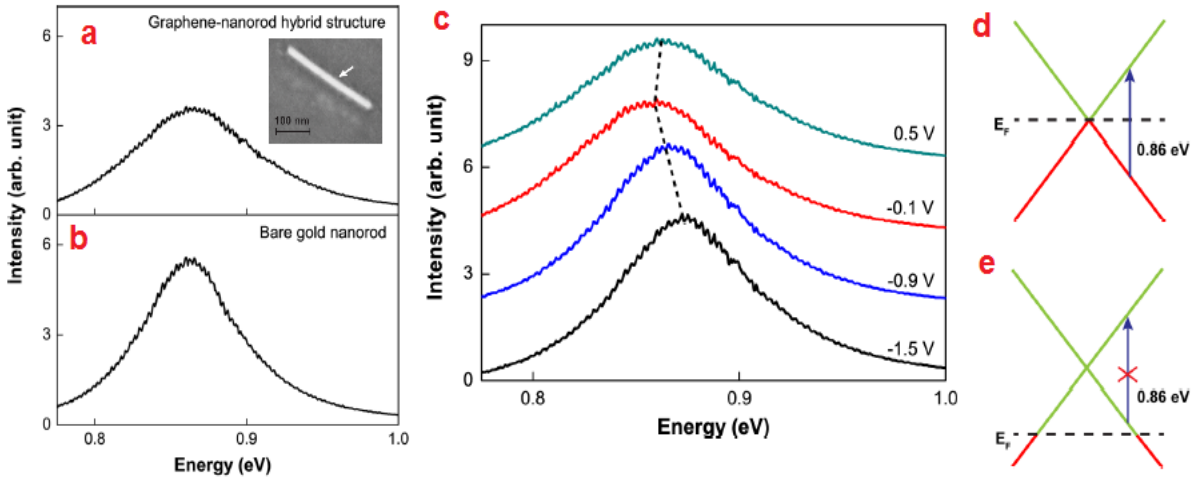

Fig 2.26: Effect of graphene on the gold nanorod plasmon resonance. **a)** Rayleigh scattering spectra of graphene-nanorod hybrid structure. **b)** Rayleigh scattering spectrum of a bare gold nanorod. **c)** Rayleigh scattering spectra of an individual graphene−nanorod hybrid structure at different gate voltages, Vg = 0.5, −0.1, −0.9, and −1.5 V, demonstrating strong modulation of plasmon excitation. **d)** Strong interband optical transitions in graphene present at all energies. They contribute to the plasmon dissipation at 0.86 eV. **e)** Illustration showing that a gate-induced shift in E_F can block the interband transition in graphene and reduce optical dissipation at 0.86 eV [Adapted from Ref. 170].

Figure 2.26c shows Rayleigh scattering spectra at V_g = 0.5, −0.1, −0.9, and −1.5 V, clearly demonstrating the capability to modulate surface plasmon resonance through electrical gating as it shifts the Fermi energy and modifies optical transitions in graphene.[107]

Efficient modulation of different aspects of the resonance was reported: A 20 meV shift in the resonance frequency, a 30% increase in quality factor, and a 30% increase in resonance scattering intensity.[170] The shift in plasmon resonance frequency and enhanced resonance quality factor can be attributed to changes in the real (ε_g') and imaginary (ε_g'') part of the graphene dielectric constant upon electrical gating respectively. Modulation of the plasmon resonance is achieved by eliminating the energy dissipation channel in graphene by

switching off its interband optical transitions through electrostatic gating. Gated graphene has a shifted Fermi energy $|E_F|$, and the optical transitions with energy less than $2|E_F|$ become forbidden due to empty initial states (or filled final states) for hole (or electron) doping[107] (Fig 2.26e).

2.4.1 Surface enhanced Raman effects

Surface enhanced Raman spectroscopy (SERS) refers to a technique that enhances Raman scattering by several orders of magnitude, as high as 10^{15}, enabling to probe single molecules.[185] In general, SERS is attributed to two major mechanisms. First one is chemical mechanism, where a new resonance state is generated through a charge transfer between the substrate and adsorbate and the second mechanism is an electromagnetic process in which a local electric-field is enhanced in certain noble metal nanostructures.[186,187] In the latter, the increased intensity of the Raman signal occurs due to large electric-field enhancement provided by localized surface plasmon resonance (LSPR).[23] The enhancement, often referred to as electromagnetic hot spots, is greatest at the surface and rapidly falls off with distance.

Raman spectrum of graphene is well investigated and has been established as a powerful tool to monitor doping, defects and edges.[188–193] However, it has limited sensitivity being an inelastic scattering process. SERS can be employed as an efficient mechanism to facilitate Raman scattering intensity, which can be further benefited from enhanced molecular adsorption[194], surface passivation[195], and tunable Fermi level[196] of graphene. In a metal/graphene system, the electromagnetic hot spots created by the metal nanostructures through LSPR are passed through the monolayer graphene, resulting in an atomically flat

surface for Raman enhancement. Recently, SERS studies were performed in mechanically exfoliated graphene-gold disc system[158] exhibiting enhancement factor up to 60. Also, CVD graphene samples with thermally deposited gold film and a close-packed gold nanosphere layer have been investigated.[197]

2.4.2 Graphene photodetector

A photodetector (PD) is a device that converts light into current and is among the most ubiquitous technology we use today. In order to introduce general ideas and to define important characteristic parameters, a conventional semiconductor photodetector is considered. Figure 2.27 shows the structure and band diagram of a metal-semiconductor-metal (MSM) photodetector. When a bias voltage is applied between two electrodes, one of the Schottky junctions (interface between a metal and a semiconductor) is reverse-biased, and the other junction is forward-biased.[198,199] At a Schottky junction in thermal equilibrium, Fermi levels of the metal and the semiconductor are equalized forming a space charge region (SCR) at the edge of the semiconductor, which is depleted of free charge carriers.[199] The light absorption near the reverse-biased junction generates electron-hole pairs which are separated by the electric-field present in the SCR, thereby creating a photocurrent. The other electrode, consisting of a forward-biased Schottky junction acts as a collection electrode.[198] In Fig 2.27b, V_B denotes the applied bias voltage, L is the distance between two adjacent contact fingers, Φ_0 is the height of the Schottky barrier and I_{ph} is the photocurrent.

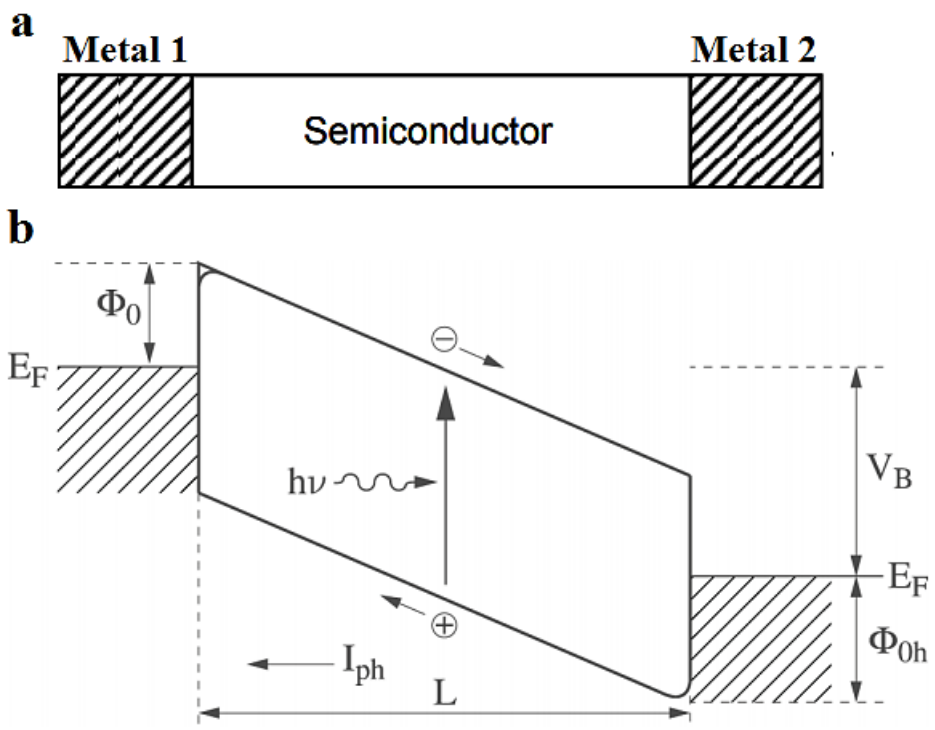

Fig 2.27: a) Schematic diagram of a metal-semiconductor-metal structure. **b)** Energy band diagram showing photocurrent generation [Ref. 198].

At a given wavelength λ, the incoming photon flux Φ_{in} is defined as the number of photons reaching the active surface per unit time. i.e., $\Phi_{in} = P_{in}\lambda/hc$ where h is the Planck constant and c is the velocity of light. Responsivity of a photodetector is the ratio photocurrent to the incident optical power (P_{in}), i.e.,

$$R = I_{ph}/P_{in} \qquad (2.30)$$

The external quantum efficiency (EQE) is equal to the number of electron–hole pairs per second collected to produce the photocurrent I_{ph} divided by the incoming photon flux.

$$EQE = \frac{I_{ph}/q}{\Phi_{in}} = \frac{R\hbar\omega}{q} \qquad (2.31)$$

Where q is the electron charge. The internal quantum efficiency (IQE) is defined in a similar way, but by taking into account only the absorbed photon flux (Φ_{abs}). i.e.,

$$IQE = \frac{I_{ph}/q}{\Phi_{abs}} \qquad (2.32)$$

Graphene, being a gapless material[5], enables charge carrier generation by light absorption over a wide energy spectrum. It also exhibits ultrafast carrier dynamics[200], wavelength-independent absorption[201,202], low dissipation rates and high mobility[203], ability to confine electromagnetic energy to small volumes[6,7], and most importantly, tunable optical properties through electrostatic doping.[106,107] Aforementioned advantages have motivated developing various photodetection platforms based on graphene over the past few years.[69,163,166,204–213]

Metal-graphene-metal (MGM) photodetectors[214] were the first class of graphene PDs investigated. In a MGM PD, the predominant mechanisms responsible for photovoltage generation are photovoltaic[157,166,207] (PV), photothermoelectric[215–217] (PTE), and bolometric[218,219] effects. PV effect exploits the built-in electric-field induced by the differently doped regions in graphene to separate the optically excited electron-hole (e^--h^+) pairs thereby giving rise to photovoltage, PTE effect is associated with the photovoltage produced by the optically generated hot electrons in regions with different thermoelectric powers, and bolometric effect is originates from the heat induced change in the mobility due to illumination leading to a change in device conductivity. Although such photodetectors feature attractive properties such as broadband operation, uniform wavelength sensitivity and fast response speed, they possess poor photoresponsivity and

low quantum efficiency (< 0.2 %)[157,220] due to the low light absorption (~ 2.3 %) in graphene.[156]

To this end, efforts have been made to enhance the photoresponse by exploiting electric-field enhancement resulting from the excitation of plasmons.[164,165,221,222] In the visible spectral range, Liu et al.[164] reported the use of plasmonic nanostructures as subwavelength scattering source to enhance optical detection and photoresponse at selected plasmon resonance frequency, enabling graphene PDs to respond sensitively to selected colors. By integrating graphene with Au nanoparticles of diameter ~ 18 nm, a largely enhanced photocurrent and EQE reaching up to 1.5 % at zero source drain bias and zero gate voltage was achieved.[164] Also, graphene FET-based detectors functioning in the THz regime have been demonstrated.[223] However, graphene photodetectors utilizing plasmonic enhancement methods are characterized by narrowband and polarization sensitive enhancement, limiting their applications mainly in spectrally resolved and polarization specific photodetection scenarios.

A significant improvement was reported by Fang et al., realizing a broadband and polarization insensitive plasmonic-enhanced graphene PD using a gold fractal metasurface.[69] When the visible light is incident on the fractal metasurface (snowflake geometry), it excites plasmon oscillations in the Au fractal structure. This leads to confinement and enhancement of the electric-field within nanometers of the structure, contributing to an extensive e^--h^+ pair generation and elevating the electron temperature through electron−electron interactions in graphene.[224] The generated carriers are then

separated via built-in electric-field and thermoelectric power differential at Au−graphene interface, giving rise to a detectable photovoltage.

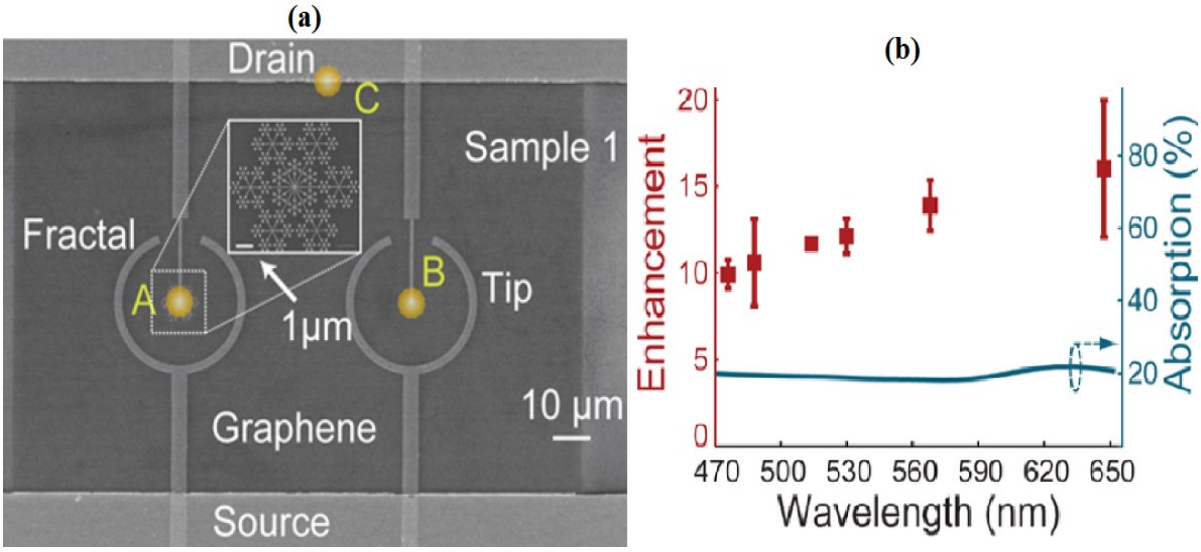

Fig 2.28: a) SEM image of the graphene photodetector with the fractal metasurface and tip-and-ring structure. **b)** Red markers: measured enhancement of photovoltage generation ($V_{fractal}/V_{edge}$, spot A to spot C in (a)) over a wavelength range from 476 nm to 647 nm. Cyan curve: simulated absorption spectrum of the fractal metasurface [Ref. 69].

Figure 2.28a presents a SEM image of the graphene PD with the fractal metasurface and tip-and-ring structure. The enhancement factor is characterized by the ratio $V_{fractal}$ to V_{edge} which denote photovoltage generated when the laser spot is incident upon the fractal metasurface, and when the laser spot is incident upon the plain gold−graphene edge, respectively (Fig 2.28b). Photoresponse was found to be independent of the polarization angle of incident light, as expected from the hexagonally symmetric geometry of the fractal metasurface design.[69]

Chapter 3: Experimental and computational methods

This section outlines all the fabrication and characterization methods used in this thesis work. Firstly, design and realization of plasmonic nanostructures with emphasis on lithographic process is described, followed by various techniques employed to characterize them. Finally, brief explanation is provided on simulation methods using COMSOL Multiphysics and CST Microwave studio, employed to investigate plasmonic properties of graphene nanoribbons and fractal structures respectively.

3.1 Sample preparation

For all fabrication processes discussed within this thesis, we used Calcium fluoride (CaF_2) and Si coated with Silicon dioxide (SiO_2) substrates. The 500µm Si wafers coated with 285 nm SiO_2 (purchased as 50mm radius discs from Si-Mat Silicon materials) were cut into pieces of dimension 1 x 1 cm. The insulating CaF_2 substrates are 500µm thick with dimension 1 x 1 cm. For the fabrication of Au fractals, the CaF_2 and Si/SiO_2 substrates with desired dimensions were cleaned as discussed in the next sections followed by spin coating of EBL resist and subsequent EBL process.

3.1.1 Graphene growth

Isolated single graphene crystals were grown on Cu foils by CVD and transferred to both Si/SiO_2 and CaF_2 substrates by our collaborators Vaidotas Mišeikis and Camilla Coletti (IIT - Center for Nanotechnology Innovation @NEST and IIT Graphene Labs)[225] (Fig 3.1).

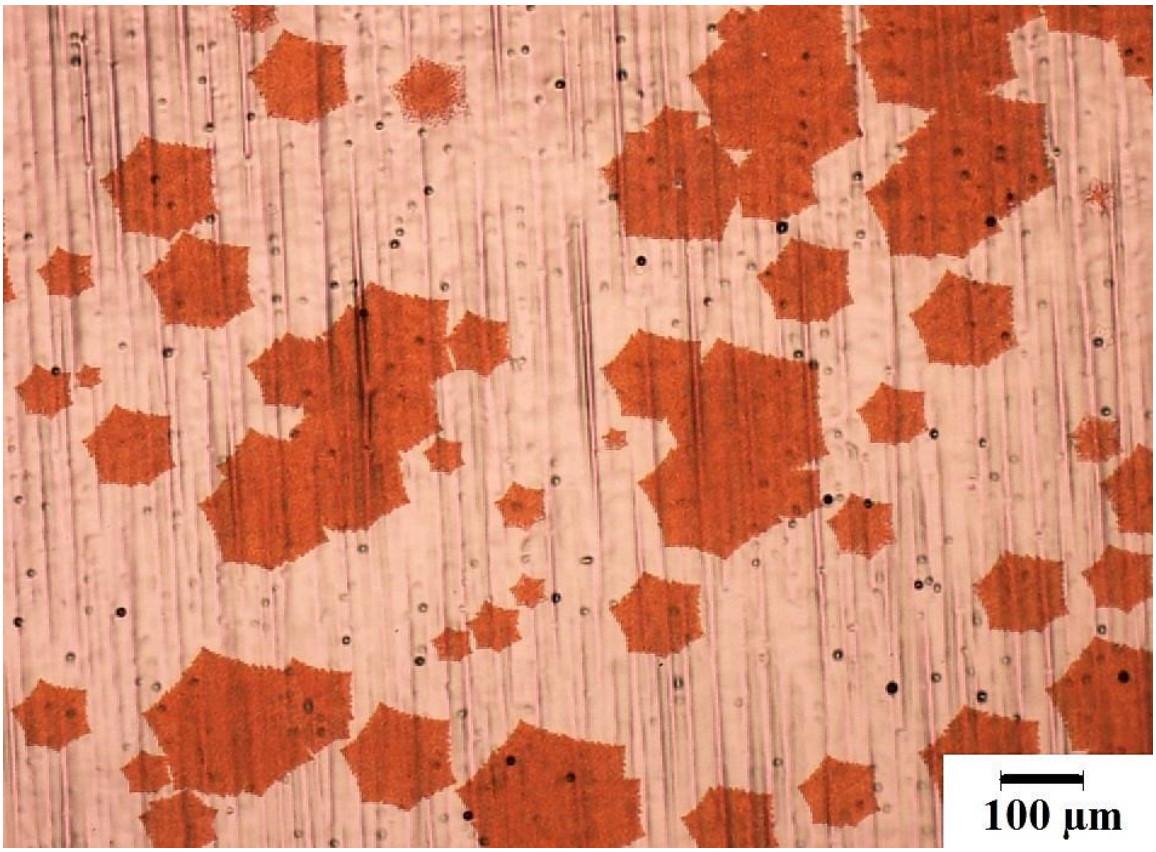

Fig 3.1: SEM image of a large isolated single crystal of CVD grown graphene on Cu foil.

Growth process was carried out in a cold-wall CVD reactor (AIXTRON "Black Magic") which offers relatively fast ramp-up and cool-down rates along with a short annealing process, resulting in faster process time (e.g. 2.5 hrs. for the production of 1 mm single-crystals). Graphene films were synthesized at a pressure of 25 mbar inside the CVD system at temperature ~ 1000 °C. The flow rates of process gases were set to 1 sccm of methane, 20 sccm of hydrogen and 900 sccm of argon. After the growth, the chamber was cooled in argon/hydrogen atmosphere to 120 °C.

3.1.2 Graphene transfer

Poly methyl methacrylate (PMMA) was used as a carrier material[136,137] for transferring the CVD-grown graphene to target substrates such as Si/SiO_2 and CaF_2. This was achieved by spin-coating PMMA onto the graphene to act as a support. The graphene/PMMA membrane was then removed from copper by electrochemical delamination[226] using sodium hydroxide as electrolyte. The graphene/PMMA membrane (suspended and stretched flat by the support frame) was rinsed in deionized (DI) water, dried, and deposited on the target substrate. The samples were heated 10 minutes at 120 °C to improve the adhesion. The PMMA was removed in acetone and IPA, completing the transfer process. Figure 3.2 shows optical image of SLG on Si/ SiO_2 substrate having lateral size ~ 200 μm.

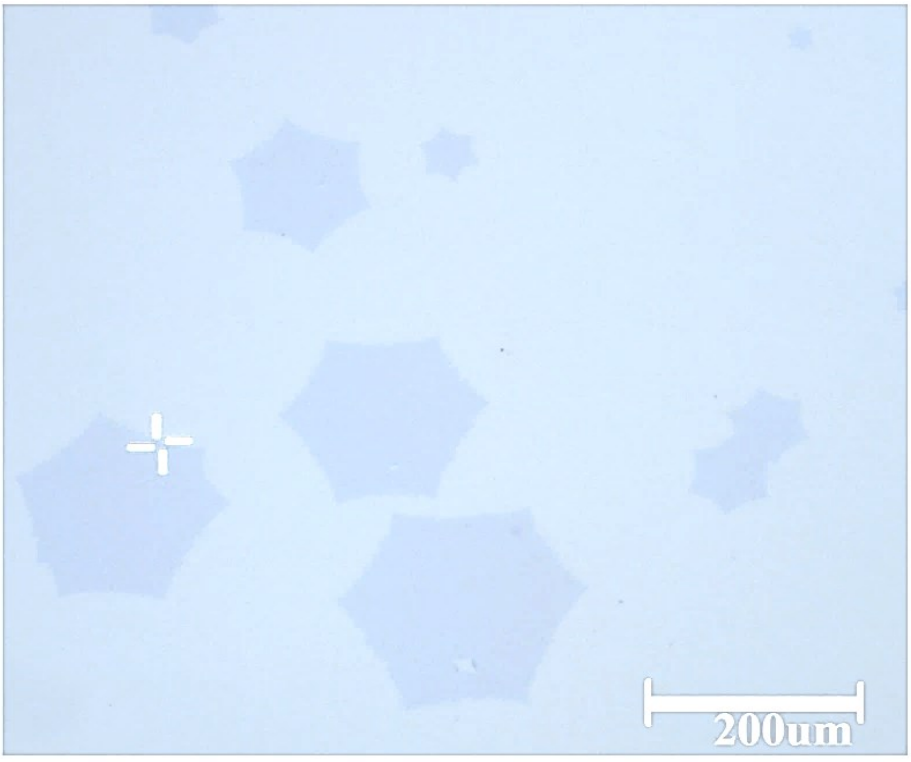

Fig 3.2: Optical microscope images of CVD graphene on Si/ SiO_2 substrate.

3.1.3 Substrate cleaning

A standard cleaning procedure was employed for all the substrates which involve 2 minutes sonication in acetone followed by isopropyl alcohol and dry with nitrogen gun. Also, 5 minutes oxygen plasma etching (Tucano tabletop plasma system) was carried out with 100W power at 0.1 mTorr pressure to get rid of any contaminants. The cleaned substrates were inspected under optical microscope and stored in a nitrogen dry box.

3.1.4 Optical imaging

A Nikon Eclipse LV 100 optical microscope was used for the preliminary investigation of samples as well as to obtain high quality images necessary for the computer-aided design (CAD) and alignment for the EBL. The lowest magnification available was 5 X, which allows to acquire a small area of the sample. In order to obtain an image of entire substrate (~ 1 x 1 cm), which was necessary for alignment purposes during EBL process, multiple images were captured sweeping the sample area and stitched them together. We used an open source photo stitching software, Hugin V 2.0. The process relies upon merging several overlapping photos taken over the substrate and blend them together using control points.[227]

3.2 Electron beam lithography

Generally, lithography is a process in which a patterned resist is used to selectively deposit metal on a substrate. Different lithographic techniques include electron beam lithography, optical lithography, interference lithography, hole-mask colloidal lithography, nano imprint lithography and nanosphere lithography[228–232]. Lithographic techniques offer great control over size, shape and orientation with good reproducibility. In a general EBL process,[228] an electron beam selectively irradiates predetermined areas of a resist which is spin-coated on the substrate. The electron beam and hence the pattern is controlled by a CAD software. EBL can be either positive or negative based on the nature of resist. A positive (negative) resist undergoes physico-chemical changes under the electron beam exposure so that the exposed (non-exposed) areas can be dissolved in a specific solvent. This process is called developing. Physical vapor deposition can then be used to deposit metal onto the patterned resist and substrate. Using a chemical etch, the resist underneath the metal layer can be attacked, hence lifting-off unwanted metal. We used acetone for this process. Poly (methyl methacrylate) (PMMA) is the common positive resist of choice due to its high resolution and chemical stability and we used it throughout the experiments.

In this thesis work we used the Raith 150 TWO ultra-high resolution electron beam lithography and imaging system which is developed using a scanning electron microscope to which a pattern generator and beam blanker are added in order to control the electron beam exposure.[233] Figure 3.3a outlines the major components in an EBL system[228] and Figure 3.3b shows a photograph of the Raith 150 TWO EBL system[230] used in this thesis work.

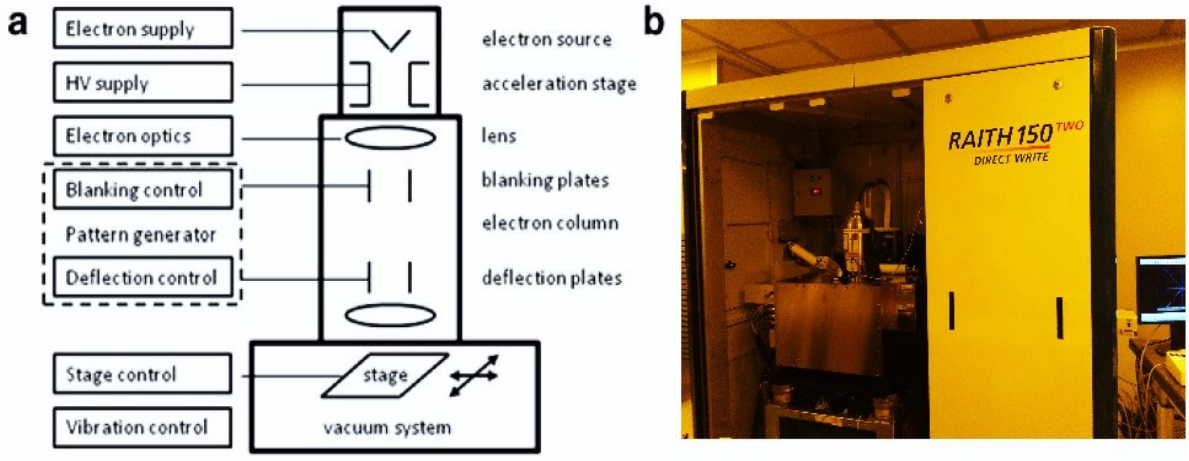

Fig 3.3: **a)** Schematic diagram showing major components of an EBL system [Adapted from Ref. 228] and **b)** Raith 150 two commercial EBL system in our lab.

We used 950k PMMA A2 (polymer chain with a mass 950 kDa, diluted 2% in Anisole) for all the fabrications in this thesis work. In order to characterize the resist thickness, a spin test was carried out with PMMA A2 with varying spin speeds on a 1 x 1 cm CaF_2 substrate. Figure 3.4 shows the measured PMMA layer thickness at different spin speeds. We used a Sawatec SM-180-BT spin coater and thickness analysis was carried out using a Veeco Dektak 150 profilometer. Prior to spin coating, the substrates were pre-baked at 120C for 2 minutes on a hot plate to remove any residual solvents and a post baking at 180C for 7 minutes was also carried out to evaporate anisole, after the spin coating. We optimized the spin speed for PMMA A2 to be 2000rpm, yielding ~ 110nm thick layer for further experiments. This choice was motivated by the following reasons.

1) such a thin layer yields high resolution[228] for the intended structures, having smallest feature size ~ 41 nm and 2) the intended metallization after the exposure (~ 35 nm) requires a resist thickness approximately 3 times thicker than the metal film (i.e., > 105 nm)[228].

After the spin coating and baking, the substrate is ready to be inserted in the Raith system for electron-beam exposure.

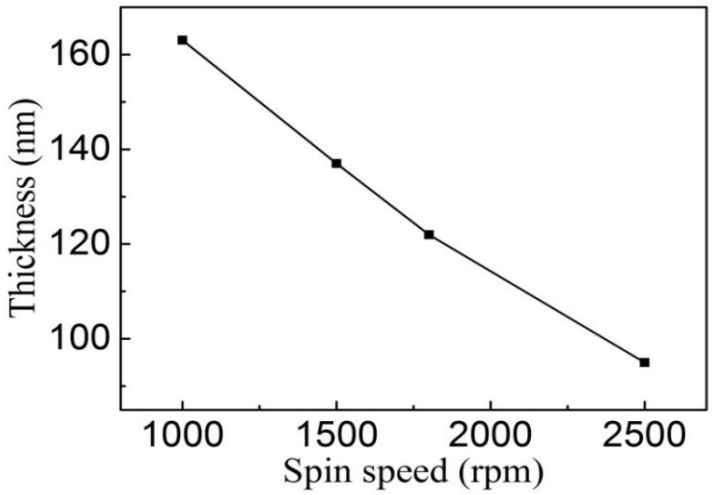

Fig 3.4: thickness analysis of 2% PMMA 950k in Anisole with varying spin speed.

RAITH150-TWO Nanosuit software was used to create and edit the CAD files for EBL which implements designs in GDSII database file format. All the structures that have to be exposed were designed with optimal dose factors. Electron dose is the number of electrons per unit area required to achieve the desired chemical response in the resist. The dose factor varies depending on the nature and thickness of the resist, and on the size and shape of the structures to be patterned. We optimized dose by exposing same pattern at different doses and after the development process, the optimum dose was determined through SEM inspection.

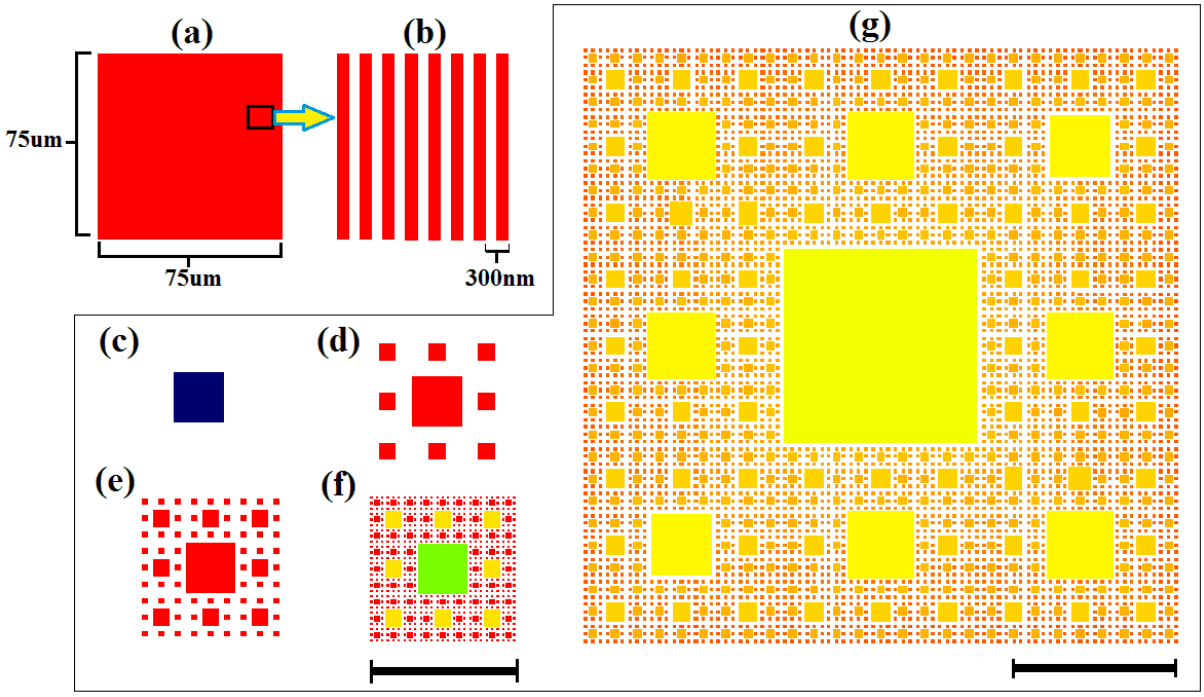

Fig 3.5: CAD designs using Raith software for graphene nanoribbon arrays **(a)** with individual ribbon width of 150nm (**b** shows zoomed view) and designed Sierpinski carpets of first **(c)**, second **(d)**, third **(e)** fourth **(f)** (scale bar = 5µm) and fifth order (g) (scale bar = 2.5µm).

Figure 3.5 shows examples of computer aided design (CAD) used in this work. The CADs of Sierpinski carpets (SC) and nanoribbons demand sub-50 nm resolution and were designed systematically by taking into account the proximity effects.[228] For instance, the 5th order SC consists of closely spaced squares with sides ~ 41 nm separated by 82 nm gaps and their precise fabrication requires careful optimization of dose and other process parameters. A low dose results in underexposure whereas a slightly higher dose leads the squares to merge as shown in Fig 3.6. Fraction of electrons which undergo large angle collisions with the substrate re-emerge into the resist, causing pattern distortion and overexposure[234,235] and this effect increases with feature size. In order to compensate for such exposure imbalances, doses were set inversely proportional to the feature size.

Structure/Parameter	EHT (kV)	Write field (μm)	Aperture (μm)	Beam current	Area dose ($\mu C.cm^{-2}$)	Area step size (nm)
Fractals (Sierpinski)	20	25	10	~ 26 pA	246-256	2
GNR	20	100	10	~ 26 pA	300	2
Contact pads	20	500	60	~ 2.3 nA	400	20

Table 3.1: Major parameters used for EBL of different types of structures.

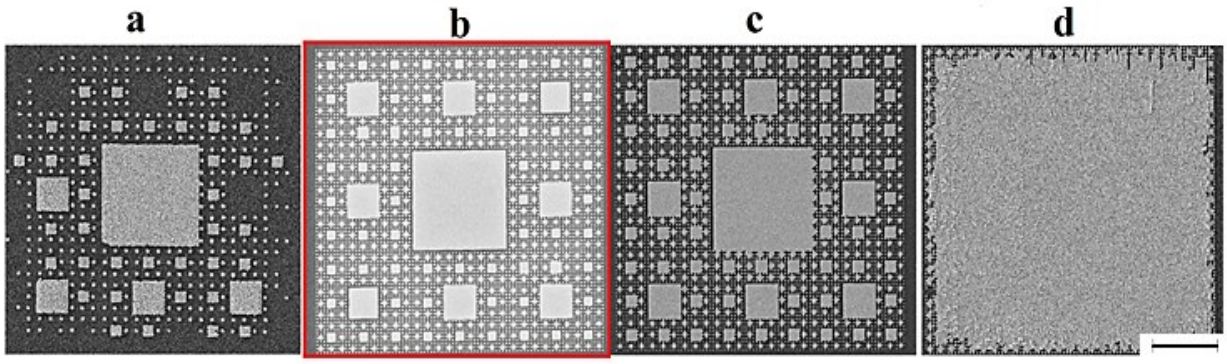

Fig 3.6: Dose optimization of 5th order SC. **(a)** displays missing and distorted features due to under-exposure while **(c)** and **(d)** shows broadened and merged features, an indication of over-exposure. The structure with optimal dose is shown in **(b)**. The scale bar is 2 μm.

For example, in the case of 5th order SC, the element with largest size (1.1 μm) was given a dose ~ 246.4 μC cm^{-2} while for the smallest element (41 nm), the dose was ~ 256 μC cm^{-2}. Once the sample is ready, it is loaded into the Raith system. Important steps prior to electron beam exposure involve focusing, adjusting stigmation and aperture alignment. Write field alignment was done in order to calibrate the electron beam deflection so that the beam movement precisely corresponds to the length defined by the coordinates of the patterns. We used a 3 point alignment procedure for sample alignment.[230,236] EBL parameters used for different structures are detailed in table 3.1. Contact pads 150 x 150 μm squares were patterned as well on the substrates for the electrical measurements.

The resist developer for PMMA is Methyl Isobutyl Kethone (MIBK). In our process, we used a solution 1:3 MIBK: IPA at 8C. A developing time of 30s was used, followed by dipping the sample in IPA and blowing with nitrogen gun. After the developing stage the sample was ready for metal deposition or oxygen etching, in the case of graphene nanoribbons/ fractals.

For the fabrication of Au Sierpinski carpets on the insulating CaF_2 substrates, a 10 nm thick layer of Al layer was deposited using a thermal evaporator (Kurt J Lesker PVD 75) prior to EBL, which acts as a conductive layer. After the electron beam exposure, the conductive coating was selectively removed by dipping the sample in KOH 1M for 20 seconds. The samples are then rinsed with DI water and dried with a nitrogen gun before developing.

3.3 Reactive ion etching

For the realization of nanostructures on graphene, such as nanoribbons and Sierpinski carpets, oxygen reactive ion etching (RIE) was employed. Generally, in a RIE system, a strong RF electromagnetic field is applied and the desired gases are introduced. A negative self-bias on the lower electrode results in acceleration of ions towards the substrate and etches the target material. We used ICP-RIE SI 500 by Sentech instruments with CESAR RF power generator. O_2 (5 sccm) was used for etching in an inert atmosphere (Ar at 80 sccm). An etching time of 30 seconds at a temperature 15 ^{0}C and with 35 W power resulted in total etching of exposed graphene.

3.4 Metal evaporation and lift off

In order to deposit fractal structures and contact pads after EBL, electron beam evaporation (Kenosistec KS 500 ET) was employed. We deposited 10 nm of Ti and 50 nm of Au to realize the contact pads for electrical measurements whereas for the Au SC fractals, different thicknesses of Au, from 25 to 45 nm, were deposited. The process was carried out at a pressure ~ 10^{-6} mbar with deposition rate ~ 0.3 Å/s.

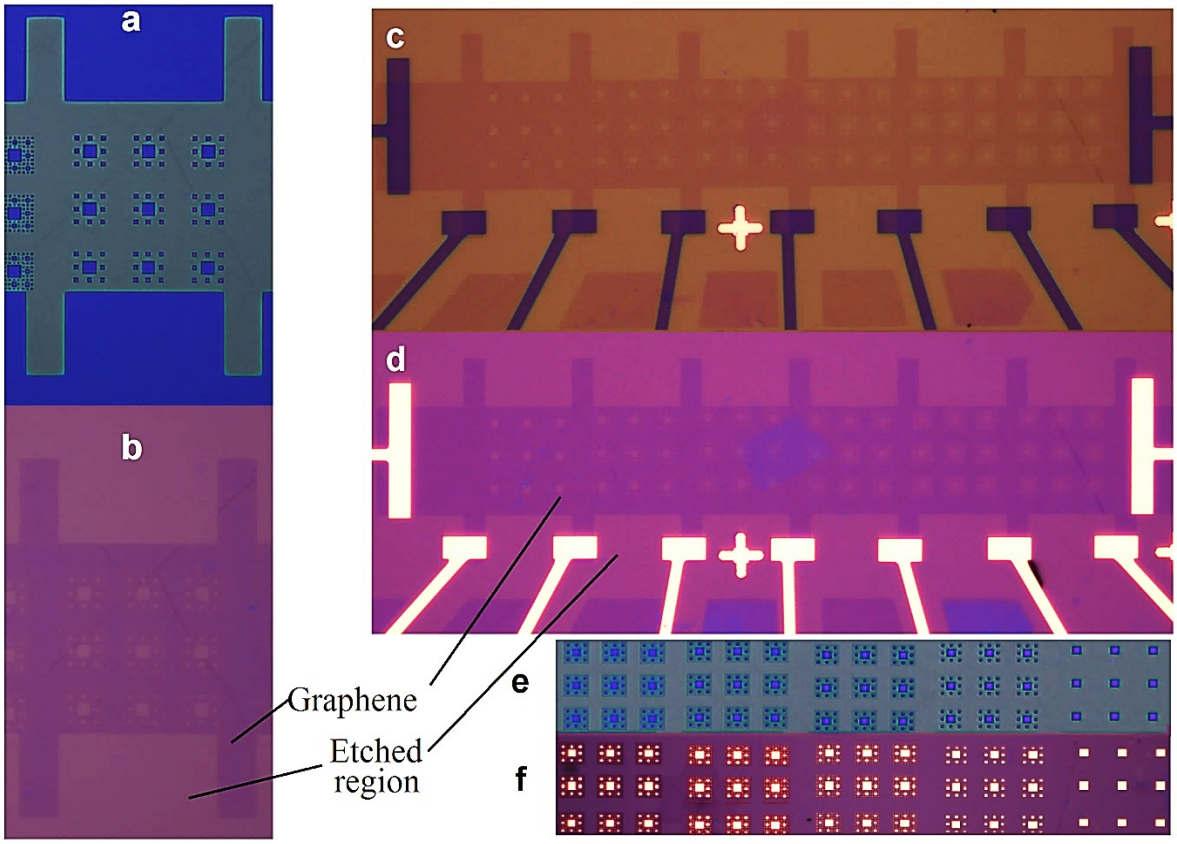

Fig 3.7: Optical images of typical sample with SC nanostructures at different stages of fabrication. **a)** SC array of order 2 after developing the resist. The blue color corresponds to the areas exposed by e-beam and the rest has PMMA mask. **b)** After etching and removal of resist with acetone. Graphene stripes left after etching (dark violet) are marked. Contact probes for the devices after resist development (dark blue) **(c)**, and after evaporation and lift-off **(d)**. **e, f)** Results of similar process for Au SCs for fractal orders 1 – 5.

Lift-off of the sample was performed in acetone at 80 ^{0}C, leaving only the structures exposed by EBL. Optical images of a sample consisting of Au SCs as well as SCs pierced on graphene along with contact probes at different stages of fabrication are presented in Fig 3.7. A graphene flake on a Si/SiO_2 substrate is shaped into a narrow strip of ~ 40 μm width using EBL and RIE. Along with this step, SC fractals were also patterned as shown in Fig 3.7b. Graphene underneath the exposed structures were etched during RIE while PMMA protects the unexposed area. Figs 3.7c,d show how graphene with nanostructures on its top were contacted by depositing narrow Au strips. Hybrid Au/G structures were fabricated by patterning SCs on the top of graphene strip, followed by developing, metal evaporation and lift-off (Figs 3.7e, f).

3.5 Characterization techniques

Essential techniques employed in order to characterize our samples are discussed below. Scanning electron microscope (SEM) was used to examine the fabricated nanostructures. SEM imaging system integrated with Raith 150 TWO was employed with an accelerating potential 5 keV and aperture size 10 μm. In addition, FEI Helios NanoLab DualBeam 650 was also used.

Height profiles of our samples deposited on Si/SiO_2 in tapping mode were obtained using a Bruker Innova atomic force microscope (AFM) system in combination with V-type cantilever and Silicon Nitride (SiN) tips.

Raman measurements were performed using a Renishaw inVia micro-Raman microscope equipped with a 100x (0.85 N.A.) objective, and laser sources of excitation wavelengths

514 nm, 532 nm, 633 nm, and 785 nm. All spectra were calibrated with respect to the first-order silicon LO phonon peak at 520 cm^{-1} and they were recorded at room temperature at a power 0.5 mW and integration time 10 s. For the Au SCs, 35 ± 3 nm thick Au film deposited on Si/SiO_2 substrate was used as a reference for SERS measurements, while for Au/G SCs, bare graphene deposited on Si/SiO_2 substrate was used. Raman maps of graphene G and 2D, and Brilliant Cresyl Blue (BCB) vibrational band $\omega^* = 1655$ cm^{-1} were scanned at 0.3 μm steps in both the directions in the plane of the sample. For the measurements on BCB, SCs were dip-coated for 1 h in 1 mM BCB aqueous solution, then rinsed in deionized water to wash the excess molecules in order to form a thin layer 12 ± 2 nm thick, and finally dried in nitrogen flow. Renishaw WiRE 3.0 software was used to analyze the collected spectra.

For the optical characterization, Thermo Fisher FTIR spectrometer with Thermo Scientific Nicolet Continuμm microscope was employed. The system is equipped with NO_2-cooled HgCdTe and Si detectors, KBr and quartz beamsplitters, and a 15x (0.58 N.A.) objective. The optical spectra of graphene and metal/graphene structures on Si/SiO_2 substrates were obtained in reflection mode while for CaF_2 substrates, transmission mode was employed.

In order to perform electrical measurements in our field-effect devices, we deposited probes (5 μm wide) and bonding pads (100 x 100 μm) on the top of desired points on graphene using electron beam evaporation (5 nm Ti and 50 nm Au). The bottom of p+ doped Si substrate was scratched with diamond pen to remove any oxide layer. Substrate was then attached on sample holder using silver colloidal paste. The two metal pads across the

graphene channel correspond to source and drain while the Si substrate contacted through silver paste is the backgate.

Electrical measurements were carried out in two- and four- probe Van der Pauw configuration by Keithley 2612A digital multimeter and Agilent 34410A digital voltmeter. For measurements in ambient condition, pads were contacted directly with sharp metal tips precisely positioned with the help of an optical microscope. For measurements in vacuum, sample was kept inside a chamber which was pumped down to ~ 10^{-6} mbar and the pads were contacted by metal tips with the help of a microscope coupled to a camera. To connect contact pad to external circuit board, a wire bonder (F&S BONDTEC Series 56) was employed (Fig 3.8).

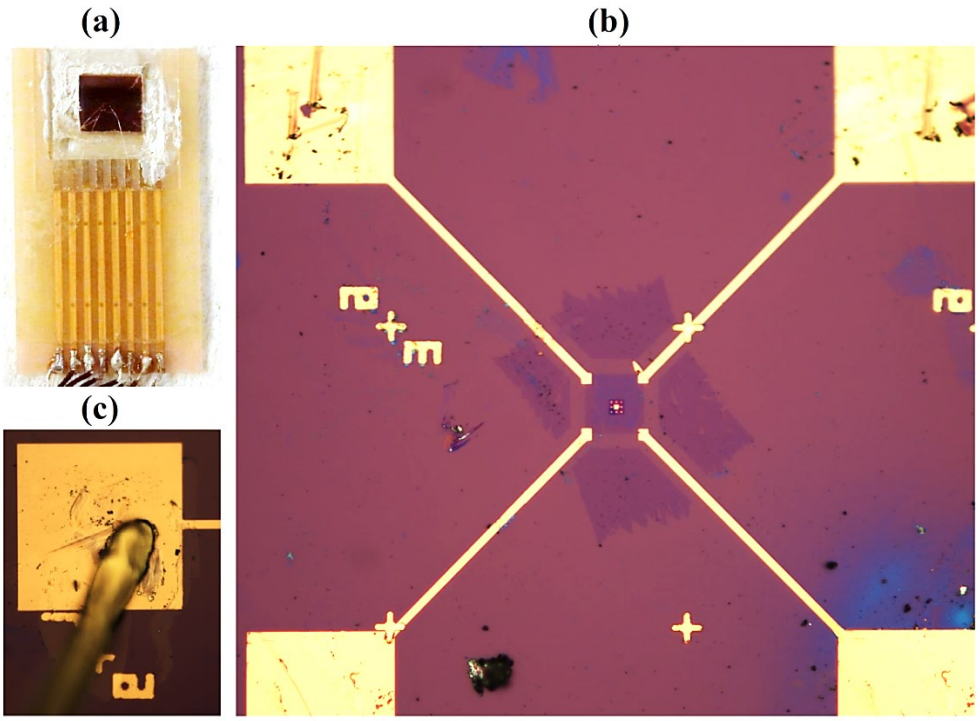

Fig 3.8: a) Sample attached on a connection board using silver paste. **b)** Representative image of final device (5th order Sierpinski carpet on top of 40x40 µm graphene stripe with Au pads and contact fingers). **c)** The contact pad connected to external circuit using a wire bonder.

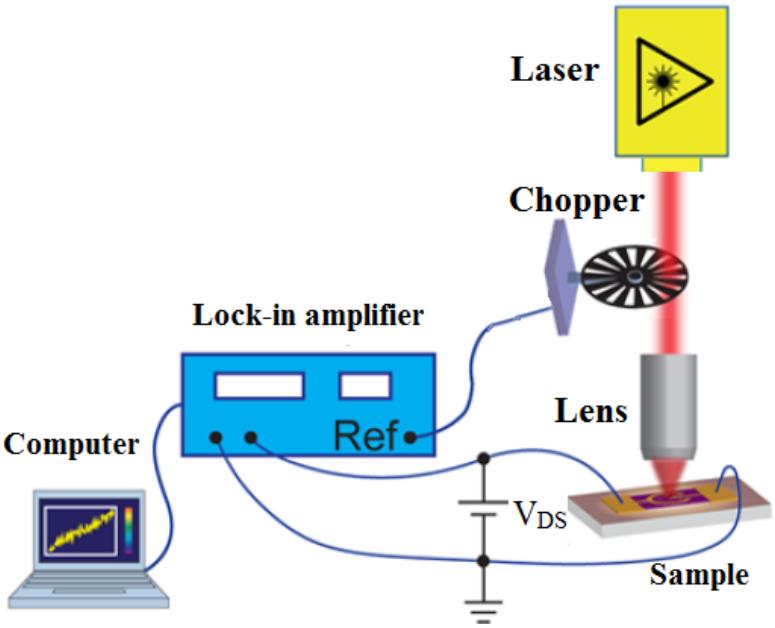

Fig 3.9: Schematic of photocurrent measurements.

Photocurrent was measured using 521 nm, 639 nm, 849 nm, and 1550 nm laser sources at different powers. The output power density was calibrated with a power meter. Responsivity was measured with a custom optical setup: an ASB-XE-175 source emits white light passing through a SP CM110 monochromator controlled by PC. Emerging monochromatic light was coupled to a fiber, modulated at 173 Hz by a mechanical chopper and focused by a lens first on the samples, then on Si and Ge photodiodes. Both AC current signals were measured by a Signal Recovery 7265 lock-in amplifier in series with a current pre-amplifier having an input impedance of 10 MΩ and an amplification factor 10^6 A/V, connected to a PC (Fig 3.9).

3.6 Electromagnetic simulations

Electromagnetic response of graphene ribbon array was simulated using COMSOL Multiphysics, which employs a finite element code allowing to solve partial differential equations in 2D and 3D domains.[237,238] GNR array is placed at the boundary between two dielectrics: air ($\varepsilon_1 = 1$) and SiO_2 ($\varepsilon_2 = 3.9$)[239] (Fig 3.10). Periodic boundaries were set with period 2W where W = 150 nm is the graphene ribbon width. After defining boundaries and domains, the mesh was generated.

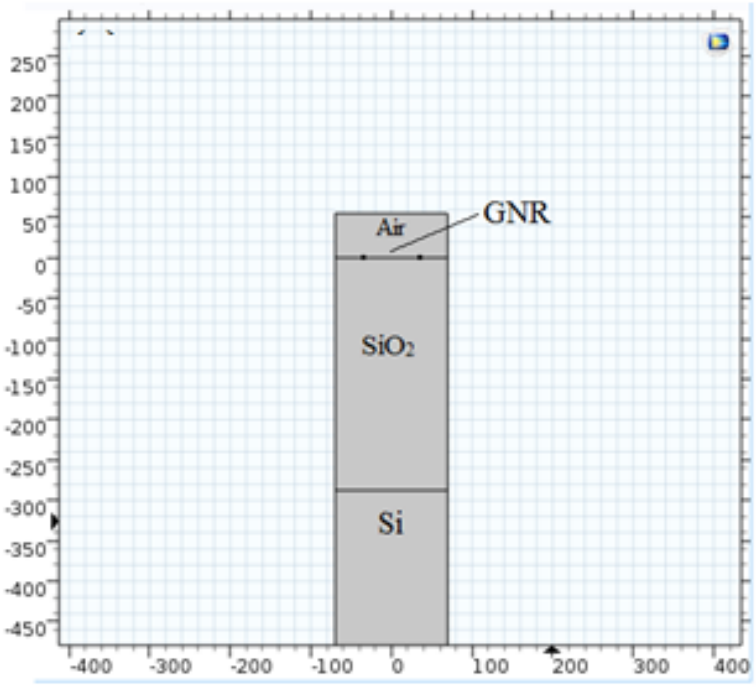

Fig 3.10: Sketch of modeled graphene nanoribbon on Si/SiO_2 substrate.

Graphene was treated as an effective medium with an RPA conductivity[6] $\sigma(\omega)$ given by equation 2.20. The dielectric constant of graphene is given by $\varepsilon_r(\omega) = i\sigma(\omega)/\omega\varepsilon_0 t$ where ε_0 is the permittivity of free space and *t* is the thickness of graphene layer which was

taken as 1 nm, which is a reasonable value considering the inhomogeneties in CVD graphene.[180]

In order to evaluate the electromagnetic near-field distributions of the gold Sierpinski carpet (SC) fractals, finite elements method (FEM) simulations were carried out in CST Microwave Studio. For our study, we considered Au SCs deposited on CaF_2 substrates as shown in Fig 3.11. The complex dielectric constant of the Au squares constituting the fractals is described by Rakic et al. model[240] while the dielectric constant of the CaF_2 substrate is given by Malitson model.[241]

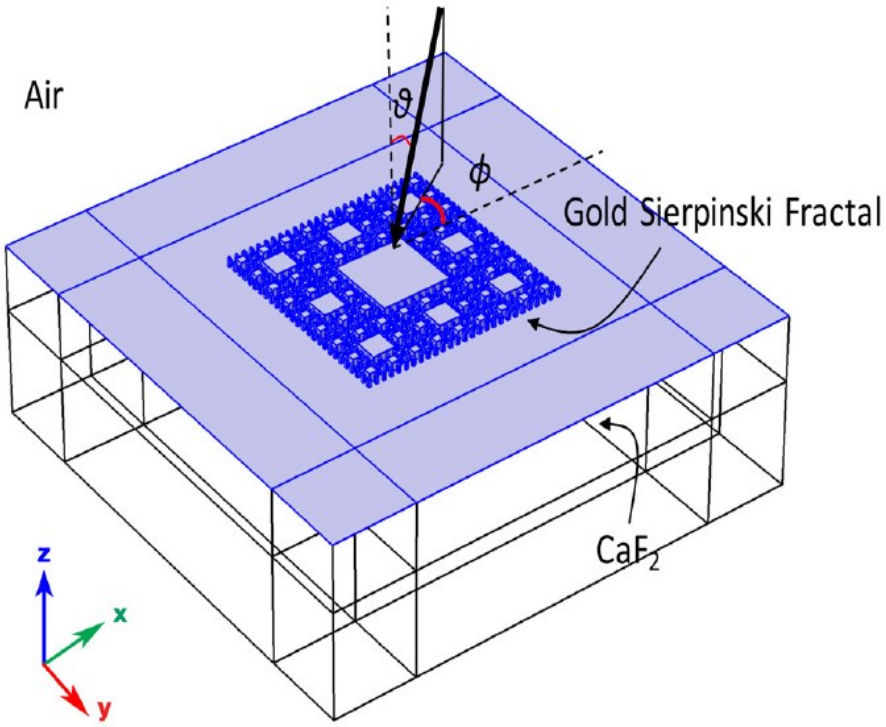

Fig 3.11: Modeled Au SC deposited on a CaF_2 substrate.

A linearly polarized plane wave (TM) radiation source with a varying wavelength is placed above the structure at normal incidence. An outer box corresponding to a perfectly matched layer was implemented to minimize unphysical reflections of the scattered waves. The boundary conditions were taken as Floquet periodic conditions. We used a sufficiently fine mesh that gave steady and mesh-independent results for the near-field distributions.

To simulate Au/G hybrid structures, graphene was modeled as an impedance surface with complex impedance obtained by aforementioned RPA conductivity for different Fermi energies. A linearly polarized plane wave (TM) radiation source with a varying wavelength is placed above the structure at normal incidence. A perfectly matched layer bounding box was implemented. The boundary conditions of the system were considered as periodic. A direct solver was chosen for the solution method (MUMPS), which allowed cluster computing for parallelization.

Chapter 4: Results and discussions

This chapter presents and explains the experimental results and compares them with electromagnetic simulations. The electrical, optical and Raman properties are analyzed for graphene nanoribbons, Au fractals and Au/G fractals in separate sections. Furthermore, the Au/G photodetector is introduced and discussed.

4.1 Graphene nanoribbons

Graphene nanoribbons (GNR) are narrow strips of graphene that have been largely investigated.[6,8,118,127,242–248] This section is intended to discuss the basic properties of GNR for their use in electronics and plasmonics. This would also serve as a benchmark in developing methodologies for the fabrication and characterization techniques that will be employed throughout this thesis, and applied to more complex structures and analysis.

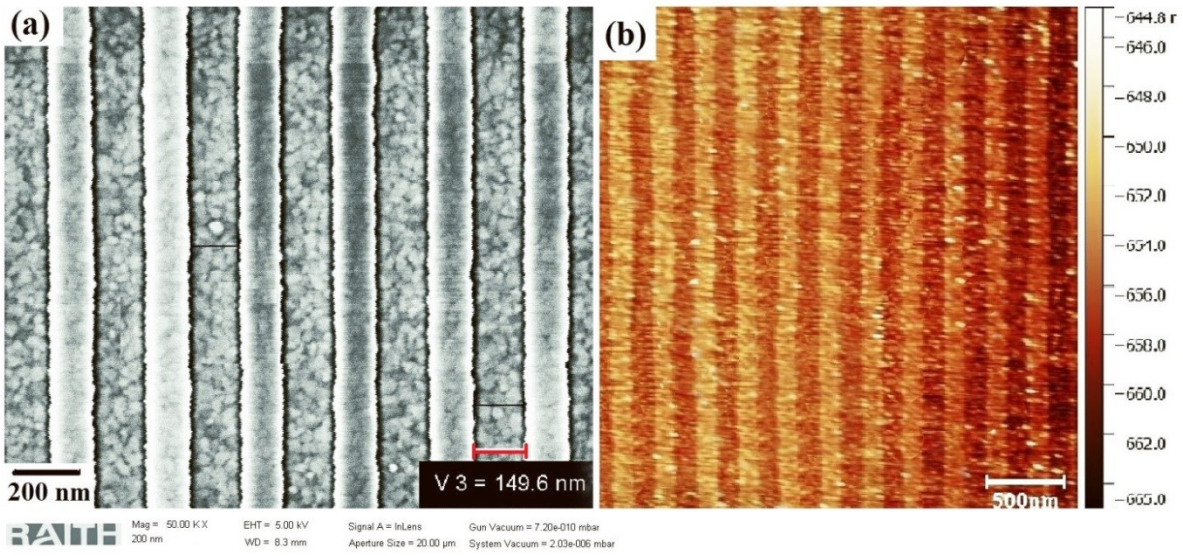

Figure 4.1: SEM **(a)** and AFM **(b)** images of GNR array fabricated on Si/SiO_2 substrate.

Figures 4.1a,b show SEM and AFM images of a representative graphene nanoribbon array, having dimension 75µm x 75µm fabricated on Si/SiO_2 substrate. SEM analysis indicates a ribbon width ~ 150 nm. Raman spectroscopy is employed to investigate structural quality of our CVD graphene samples and FTIR revealed their optical properties. GNR based field-effect devices are fabricated with Si backgate to explore transport characteristics. These results are presented in the following sections.

4.1.1 Raman characterization

Raman Spectroscopy measurements are performed at three different locations in the sample: graphene without patterning, GNR area, and the area where reactive ion etching was carried out. This would allow to access number of graphene layers[188,249], and provide a comparison between bare graphene and GNR in terms of defects[250] and edges.[190,251,252] Figure 4.2a shows representative Raman spectra on all the three regions at 633 nm laser excitation, 5 mW incident power, and 10 s collecting time.

It can be seen that the Raman spectra of CVD graphene reveal the characteristic features to be expected in any graphite based material namely G, D and 2D bands.[188,249] The G band (typically at 1580 - 1590 cm^{-1})[253] corresponds to Brillouin zone-center optical E_{2g} phonon in graphene. The E_{2g} phonon involves in-plane bond stretching of all pairs of carbon atoms.[188,254] It has a wavevector of zero, and thus the Raman process for G band can be satisfied even under non-resonant conditions. As a result, the intensity of G band is insensitive to external factors such as polarization and carrier concentration.[255]

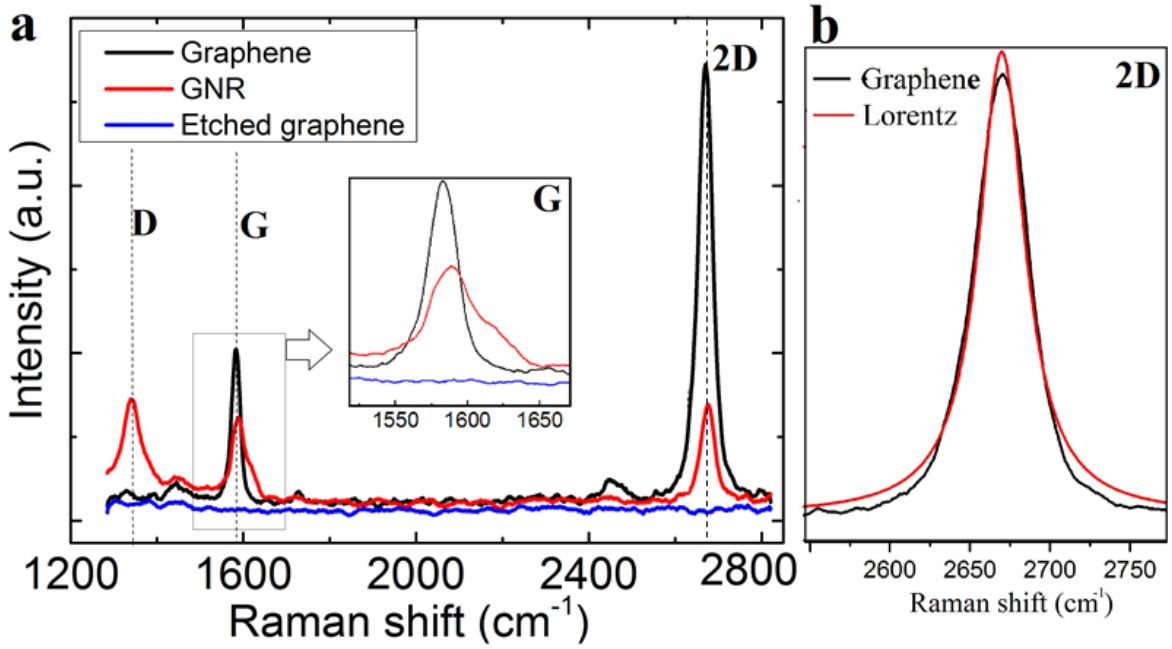

Figure 4.2: a) Raman spectra of graphene, GNR and area totally etched by RIE. Inset shows zoomed view of marked area. **b)** 2D peak of graphene fitted to single Lorentzian.

Band	Position (cm^{-1})		FWHM (cm^{-1})	
	Graphene	GNR	Graphene	GNR
D		1342		69
G	1583	1589	20.6	42
2D	2670	2675	35	35

Table 4.1: Key features obtained from the Raman spectra.

D band, typically positioned at ~ 1340 cm^{-1} [Ref. 253] is due to the breathing modes of six atom rings and requires defect for activation.[254,256] Presence of D band requires excitation and inelastic scattering of a charge carrier by a phonon, then a second elastic scattering by a defect or zone boundary, then resulting in recombination.[191] Thus this double resonance process include one elastic scattering event caused by defect of crystal and one inelastic

scattering event induced by electron-phonon interaction. Double resonance Raman scattering can also happen as an intravalley process, that is, connecting two points belonging to the same cone around K which gives rise to D´ band.[191]

The 2D band which lies around 2680 cm^{-1} [Ref. 253] is the second order of D band with frequency twice as that of D band, which originate from a double resonance process where momentum conservation is satisfied by two phonons with opposite wave vectors and no defects are required for its activation.[188,256] At room temperature, SLG exhibits a sharp 2D band that can be fitted with a single Lorentzian curve.[191] Differently, in a bilayer graphene, a parabolic energy dispersion E (k) originate as a consequence of the Bernal A-B stacking. In this case, 2D band is upshifted and is broadened. The 2D band consists of four components: $2D_{1A}$ and $2D_{1B}$ $2D_{2A}$ and $2D_{2A}$.The overall shape of the D band will be the convolution of these single Lorentzian features.[188,191]

Analyzing the acquired Raman spectrum in our samples, it is clear that the 2D band (~ 2670 cm^{-1}) can be fitted with a single Lorentzian peak (Fig 4.2b), which signifies presence of SLG.[188,191,257] Further, full-width-at-half-maximum (FWHM) of 2D band below 40 cm^{-1} is a signature of single layer nature of GNR,[188,257] which is calculated as ~ 35 cm^{-1} in our case. Generally speaking, anything that breaks the symmetry of the carbon honeycomb lattice can be regarded as defect in graphene[193], and as mentioned, D band requires defects for activation. The Raman spectrum of CVD graphene shown in Fig 4.2a does not have a well-defined D band whereas in GNR, a prominent D band is present with I_D/I_G ratio ~ 2. A broadening of G band can also be observed in GNR Raman spectrum unlike that of bare graphene. This is attributed to the splitting of G band into G and D' bands (~ 1620 cm^{-1})

due to the elastic inter-valley scattering of electrons induced by defects.[190,251,252] Although CVD GNR undergoes a few more processing steps than CVD graphene, the induced disorder is significant. It is worth noting that an I_D/I_G ratio of ~ 2 was reported[258] for GNR with comparable dimensions (~ 100 nm) fabricated on mechanically exfoliated graphene, which matches well with that of CVD GNR in our case. Also, from the literature, the basal plane C–H defects and crystalline defects introduced by EBL in graphene is negligible[258,259] and the intensity of D peak depends mainly on the edge-region of the nanoribbon.[253] Above observations along with the reported linear increase in I_D/I_G with decreasing ribbon width[253] suggests that the D band observed in our GNR can be attributed predominantly to the edges introduced during the etching process. [251–253]

A blue shift of ~ 6 cm^{-1} is observed in the G band position of GNR compared to that of CVD graphene as represented in table 4.1. This could be attributed to oxygen induced doping of GNR during the etching process. Oxygen is more electronegative than carbon and is expected to withdraw π electrons of GNRs (dope with holes).[260,261] Further, from the reported investigation of G band evolution based on electrical gate measurements[183], an approximate charge carrier density shift of ~ 5 x 10^{12} cm^{-1} is estimated due to oxygen induced doping. Similarly, an upshift in the position of 2D band by ~ 5 cm^{-1} corresponds to a change in charge density ~ 5 x 10^{12} cm^{-1} as estimated from the comparison with Ref. 183.

4.1.2 Transport measurements

The electronic transport properties of GNRs are investigated by fabricating field-effect transistors (FET) with Si as a backgate. The gate controls the current flow between source and the drain, exploiting the GNR array as channel material.[97,98,127,262–266]

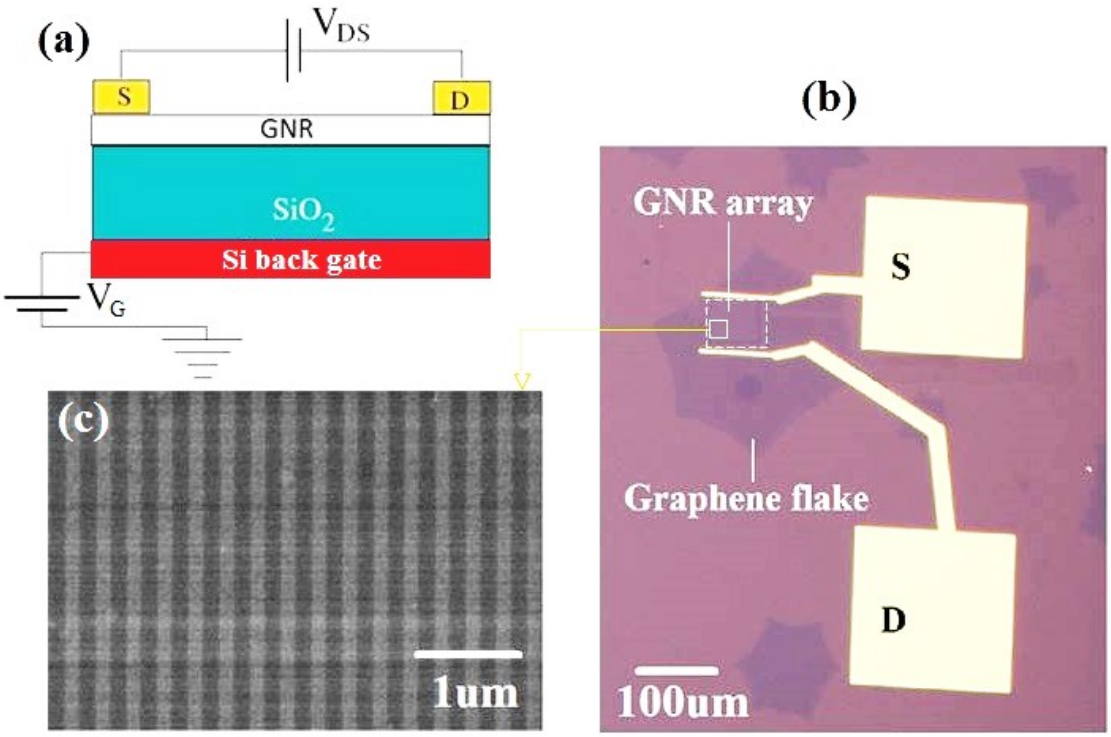

Figure 4.3: a) Schematic of GNR FET with Si backgate. S and D denote source and drain contacts respectively **b)** Optical image showing Au pads and graphene flake with GNR array. A zoomed view of GNR array is shown in **(c)** as obtained from SEM.

Figure 4.3a shows a schematic structure of the GNR – FET, while an optical image is shown in Fig 4.3b. S and D denote source and drain contacts respectively. The device has two metal pads (Ti/Au) as source/drain contacts, heavily p-doped Si as the back-gate, and a 285 nm thick SiO_2 which acts as dielectric layer. The current-voltage characteristics and transfer characteristics of the device are shown in Fig 4.4. V_{DS}, I_{DS} and V_G denote the source- drain bias voltage, source- drain current, and the gate voltage respectively.

Patterning graphene into nanometer size ribbons results in the formation of an energy gap due to quasi-one-dimensional confinement of the carriers in a stripe of length L and a small finite width W, which allows its use in conventional semiconductor device operations.[98,127,266] The remarkable property of graphene to continuously drive the Fermi level from the valence to the conduction band by applying a gate voltage[97,98,267] is shown in our devices for a gate voltage sweep from - 100 to 150 V (Fig 4.4a). We observe a variation of current as a function of Si backgate voltage.

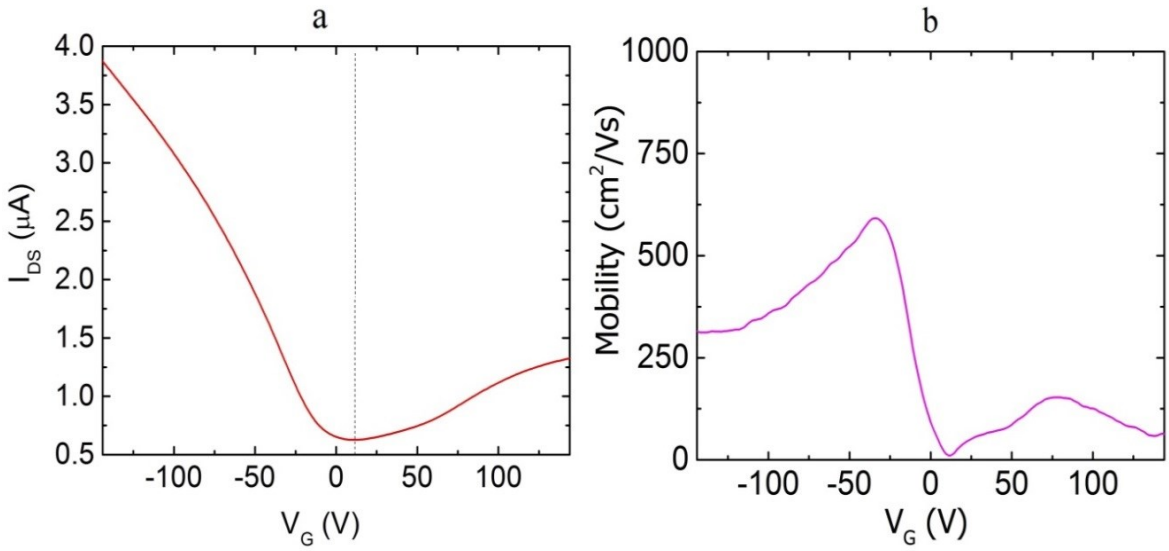

Figure 4.4: Electrical characterization of the GNR-based FET. a) Variation of source – drain voltage with the gate voltage recorded at V_{DS} = 10 mV. b) V_G dependent field – effect mobility of GNR FET. Measurements are performed at room temperature.

As the Fermi level is driven inside the conduction (valence) band, the current increases with increasing the concentrations of electrons (holes) induced by positive (negative) gate voltages. Whenever the Fermi level goes from the conduction (valence) band to the valence (conduction) band, it crosses the charge neutrality point voltage (V_{CNP} ~ 11 V) which manifests as the maximum resistance of the channel (i.e., minimum conductance). The

observed positive value of V_{CNP} indicates p – doping, i.e., presence of holes.[98] A number of reasons could be responsible for this unintentional doping including metals[268,269] and gases.[270] We also observe that for a region of back gate voltages near V_{CNP}, the current does not go to zero but remains at ~ 0.6 μA. In this case, charge transport can be described by leakage current due to thermionic emission as the Fermi tail of carriers is significant at room temperature.[97,98,271]

Traditional field-effect mobility model or direct transconductance method[272] was employed to calculate mobility of our device (Fig 4.4b), which uses the transconductance g_m and gate induced carrier density of the device to extract mobility. Although field-effect mobility is always lower than the real mobility due to the ignorance of contact resistance, it is close to the real mobility at longer channel lengths (> 6 μm) [Ref. 273] as the channel resistance is dominant over the contact resistance and our devices have a channel length of 75 μm. The field-effect mobility (μ_{FE}) is the change in sheet conductivity of graphene $\Delta\sigma$ due to carrier density modulation Δn as[272–274]:

$$\Delta\sigma = \Delta n e \mu \tag{4.1}$$

$$\mu_{FE} = \frac{\Delta\sigma}{\Delta n} e = \frac{L}{W} \frac{g_m}{C_g V_{DS}} \tag{4.2}$$

Where e is the electron charge, L is the gate channel length and W is the channel width. C_g is the gate capacitance per unit area which depends on the SiO_2 thickness (t) and the dielectric constant of the material (ε), i.e., $C_g = \varepsilon/t$. Field-effect mobility is plotted against gate voltage in Fig 4.4b as calculated from Equation 4.2. The transconductance is given

by $g_m = \frac{dI_{DS}}{dV_G}$. Note that when the drain current reaches a minimum at V_{CNP}, transconductance becomes zero. Constant field-effect mobility is observed when I_{DS} varies linearly with V_G. The difference between actual mobility and field-effect mobility depends on the gate voltage, and reaches a minimum value at a certain V_G which is close to the peak transconductance point.[273] It is observed that the transconductance reaches its maximum value approximately at - 34 V and the corresponding mobility is ~ 592 cm^2/vs which is comparable with reported values of GNR FET mobilities.[128,274,275] Carrier mobility in GNRs is greatly determined by the phonon scattering, charged impurities on the GNR surfaces, surface roughness of substrate, structural defects in the basal plane, edge-disorder, width and temperature.[276] The observed low value of mobility in GNR could be attributed to disordered edges, impurities and phonon scattering.[274,276–279]

The bandgap created by quantum confinement in a perfect armchair-edge GNR is $E_g = 2\pi\hbar v_F/3W \sim 1.38$ eV/ W (nm) where ħ is the reduced Planck's constant, $v_F = 10^6$ m/s is the Fermi velocity and W is the width of the GNR.[280] This implies sub-10 nm wide GNR can enable room temperature operation similar to traditional semiconductors. A rough estimation of the bandgap value in our device indicates $E_g \sim 9.2$ meV, assuming a width dependent band gap ($E_g \sim 1/ W^{\alpha}$ where α is close to unity[245,281]) through quantum confinement and edge effects. Note that this transport gap in our device originates from the disordered edges, leading to a thermally activated hopping transport along the localized states with sizes close to the GNR width[265] and a real bandgap becomes important only for much narrower GNRs below 10nm.[244] As a consequence, the device cannot be completely turned off[127,244], however, we clearly achieved a gate voltage controlled current flow.

4.1.3 Plasmons in graphene nanoribbons

Owing to the unique tunability[6,116,119,121,122], high degree of electromagnetic confinement,[121,122] and long plasmon lifetimes[6,282], graphene has recently attracted tremendous attention and shown to be promising candidate for optoelectronic and nanophotonic applications in a wide spectral range from THz to IR.[8,283] In this section, plasmon excitation in our GNR array by means of Fourier-transform infrared spectroscopy (FTIR) is presented.

The experimental setup is shown in Fig 4.5a. Electromagnetic response is represented in terms of reflectance of light from the ribbon array with electric-field polarized perpendicular and parallel to the ribbon with Si/SiO_2 substrate as reference (Fig 4.5b). We observe three major resonance dips (P1, P2 and P3) in the MIR region of the spectra. P1 and P2, located at $\omega_{sp1} = 883$ cm^{-1} and $\omega_{sp2} = 968$ cm^{-1}, could be attributed to the interaction of graphene plasmons with surface optical phonons of SiO_2 substrate. This results in collective plasmon modes in graphene, producing hybridized plasmon-phonon modes.[118,125,221,284] A third reflectance dip (P3), observed at $\omega_p = 1333$ cm^{-1} (7.5 μm), is attributed to the graphene intrinsic optical phonon mode.

Plasmon excitations in a graphene ribbon correspond to collective oscillations of electrons across its width. Therefore, the spectrum with parallel polarization shows no resonance peaks[116,118] while the spectrum with perpendicular polarization shows prominent resonance peaks due to the excitation of localized plasmons, as evident from Fig 4.5b. It is worth noting that the ribbon-to-ribbon coupling effects are negligible in this case.[119,285]

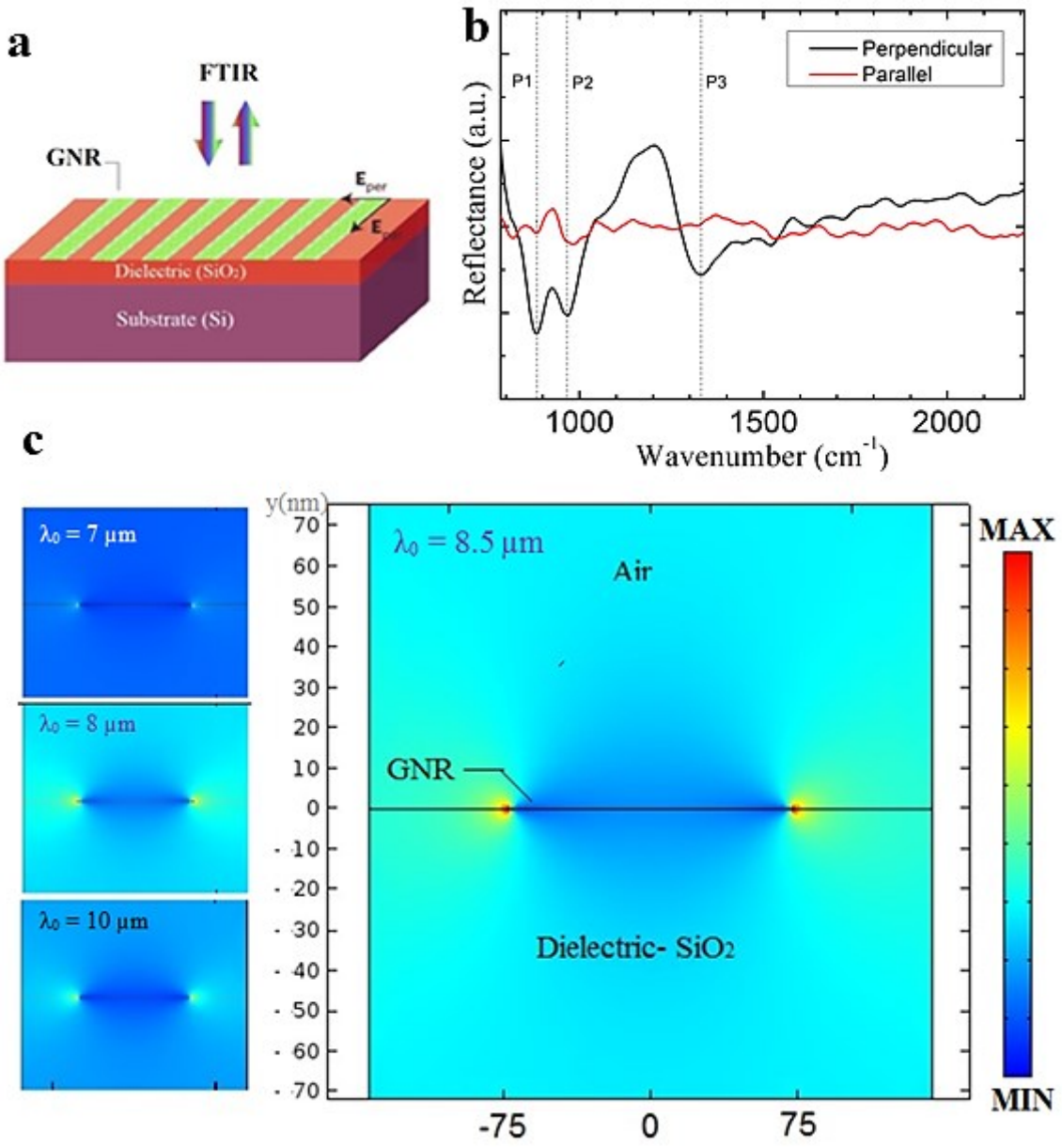

Fig 4.5: a) Schematic of experimental setup. **b)** Reflectance spectra of light from the ribbon array with electric-field polarized perpendicular and parallel to GNR. **c)** Electromagnetic simulation with light polarized perpendicular to the ribbon at incident wavelengths 7 μm, 8 μm, 8.5 μm and 10 μm showing electric-field distribution.

Effective charge dipoles are produced in each ribbon, which creates necessary restoring force for the collective charge oscillations. Enhanced field intensities occur at individual ribbon edges, as we visualize using finite element simulations (Fig 4.5c). Here the electric near-field distribution computed at different incident wavelengths is shown. A maximum enhancement can be observed at the resonance wavelength $\lambda_0 \sim 8.5$ μm ($\omega_p \sim 1176$ cm^{-1}), which is comparable with the experimentally observed reflectance dip at ~ 7.5 μm ($\omega_p \sim$ 1333 cm^{-1}). The marginal discrepancy might be due to the fact that the electrically active ribbon width is slightly lower than the physical width due to atomic-scale defects and complicated edge chemistry.[118,286]

4.2 Gold Sierpinski carpets

In this part, characterization of Au plasmonic structures inspired by Sierpinski carpet deterministic fractals is presented. The first five orders of Au SC are fabricated on CaF_2 and Si/SiO_2 substrates by employing EBL, electron beam evaporation and lift-off techniques (see chapter 3). We systematically investigated the far-field and near-field properties of Au SCs by FTIR and SERS, supported by FEM electromagnetic simulations.

Sierpinski carpets are realized starting from a unit cell of side $L_0 = 10$ μm that is divided into a 3 x 3 array of sub-cells of lateral size $L_t = L_0 3^{-t}$ with an Au square replacing the central sub-cell. By iteratively applying the same rule to each generated sub-cells, fractals with higher orders of complexity are obtained. Here, SC scale-invariance factor is $\mathcal{L}_t = 3^{-t}$. Since the number of sub-cells in SC is $\mathcal{N}_t = 8^t$, the fractal dimension is $d_H = \log \mathcal{N} / log(\mathcal{L}^{-1}) \approx 1.89$. The total area of the fractal is $\mathcal{A}_t = \sum_t N_t A_t$, with $A_t = L_t^2$ the area of the square elements, while its spatial filling fraction is $f = \mathcal{A}_t / L_0^2$. The main features of SC are summarized in table 4.2.

Figure 4.6a-e show representative SEM images of Au SC fabricated on a Si/SiO_2 substrate with nominal thickness 35 ± 3nm. Also, we realized periodic arrays of squares with lateral size L_t, as a reference. For example, Fig 4.6f shows a periodic array with size L_5. We carried out Fast Fourier Transform in SCs and periodic array to compare their reciprocal lattices. In Fig 4.7a,b, discrete square reciprocal lattices of the periodic array

with square size L_5 and a singular continuous reciprocal lattice of the SC for t = 5 are provided respectively.

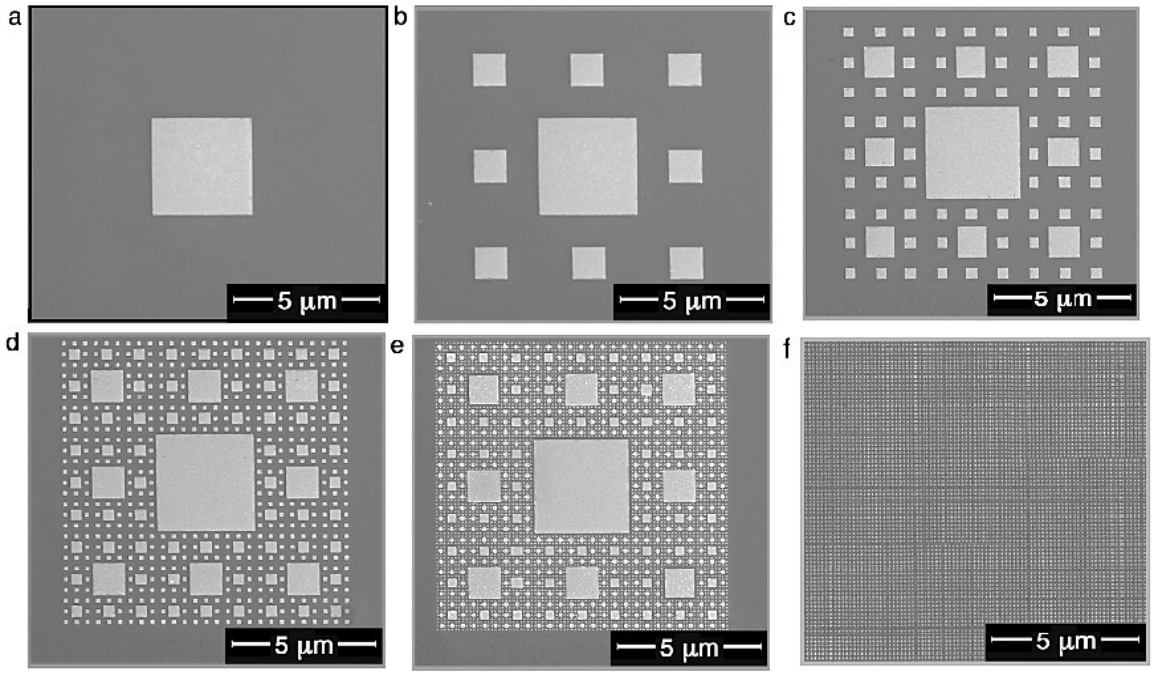

Figure 4.6: SEM images of Au SC fabricated on a Si/SiO_2 substrate with thickness $\mathbf{35 \pm 3\ nm}$ for fractal orders t = 1 **(a)**, t = 2 **(b)**, t = 3 **(c)**, t = 4 **(d)**, and t = 5 **(e)**. **f)** $\mathbf{35 \pm 3\ nm}$ thick Au periodic array with square size L_5.

It can be seen that the SC has a larger number of points in the reciprocal space than that of the periodic array due to the fact that its fractal reciprocal lattice is a superposition of five periodic lattices with different constants $a_t = 3L_t$ under periodic approximation.[51,287] Each point of such a lattice is distinguished by a lattice vector $\left|\mathbf{G}_{ij}^{(t)}\right| = 2\pi\sqrt{i^2 + j^2}/a_t$. It is worth mentioning that also $\mathbf{G}_{ij}$ is scale-invariant as $\mathbf{G}_{ij}^{(t)} = 3^{t-1}\mathbf{G}_{ij}^{(1)}$, thereby realizing a hierarchy of first pseudo-Brillouin zones $[-\pi/a_t, \pi/a_t]^2$.

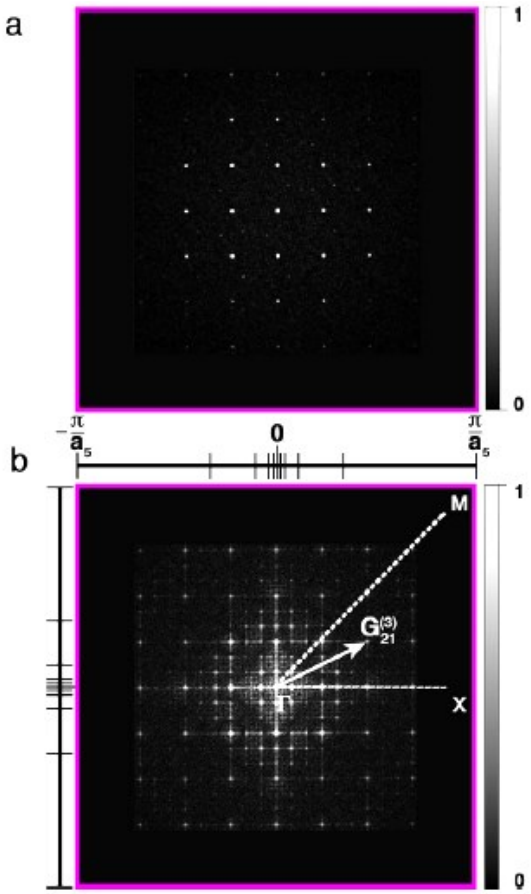

Fig 4.7: a) Fast Fourier transform (FFT) of the SEM image for the periodic array and **b)** that of SC at t = 5. $\Delta = \overline{\Gamma \boldsymbol{X}}$ and $\boldsymbol{\Sigma} = \overline{\Gamma \boldsymbol{M}}$ direction in the fractal reciprocal lattice are marked along with the first pseudo-Brillouin zones $[-\boldsymbol{\pi}/\boldsymbol{a_t}, \boldsymbol{\pi}/\boldsymbol{a_t}]^{\mathbf{2}}$ for different orders.

t	$\mathcal{N}_t$	N_t	L_t (μm)	A_t (μm^2)	$\mathcal{A}_t$ (μm^2)	f
1	8	1	3.382 ± 0.050	11.438 ± 0.338	11.438 ± 0.338	0.114 ± 0.003
2	64	8	1.121 ± 0.011	1.257 ± 0.025	21.494 ± 0.200	0.214 ± 0.002
3	512	64	0.390 ± 0.017	0.152 ± 0.013	31.222 ± 0.832	0.312 ± 0.008
4	4096	512	0.130 ± 0.007	0.017 ± 0.002	39.926 ± 1.024	0.399 ± 0.010
5	32768	4096	0.044 ± 0.003	0.002 ± 0.001	48.118 ± 4.096	0.481 ± 0.041

Table 4.2: Main features of our Au SC

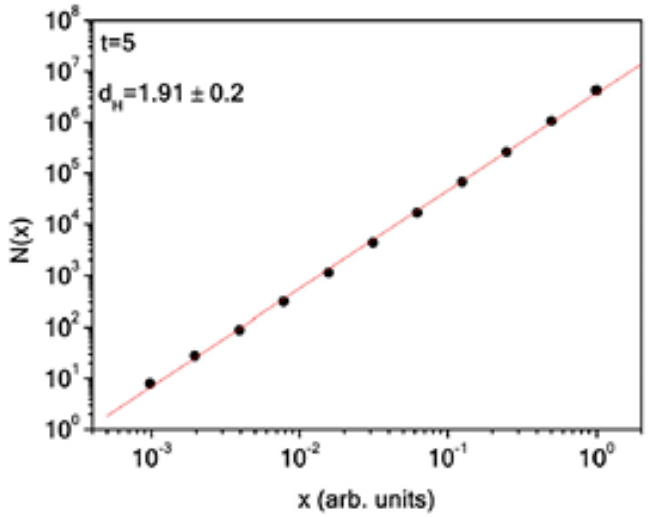

Fig 4.8: Box-counting algorithm applied on the SC reciprocal lattice. The fit returns a fractal dimension $d_H = 1.91 \pm 0.02$.

By box counting method[288], we confirmed that the reciprocal lattice of SC is also self-similar (Fig 4.8). The algorithm works as follows. A square array with periodicity x is superimposed on the reciprocal lattice image. Initially x is set at Ɛ/2 (where Ɛ is the size of the image), resulting in an array of $2^2 = 4$ boxes. Then N(x) is the number of all the squares containing at least one pixel of the image. The array periodicity x is then reduced stepwise by factor of 2 and the process is repeated until x equals to the distance between two adjacent pixels. The slope of the log N(x) - log x plot gives a fractal dimension $d_H = 1.91 \pm 0.02$.

4.2.1 Optical properties

Figure 4.9 details optical properties of Au SCs along with experimental and calculated wavelengths of the SC extinction peaks for fractal orders t = 1 - 5. We attribute the multiple resonances shown in Fig 4.9a to diffraction mediated localized surface plasmons[79,289] as explained in the following section.

In the case of periodic and quasi-periodic photonic crystals, when the wavelength of a LSP resonance is slightly larger than the lattice constant, the photonic mode due to the optical diffraction associated with the lattice couples to the plasmonic mode of each particle, producing a hybrid mode (i.e., Wood anomaly). [51,78–80,289–294] In particular, when the wavelength of the incident light is larger than the lattice spacing, all the diffracted beams other than zeroth order are evanescent (i.e., Rayleigh cutoff) and all the particles are radiating in phase by dipolar coupling in the plane of the grating. This results from the momentum matching condition[79,290,291,293] $\mathbf{q} = \mathbf{k} \sin\theta \pm \mathbf{g}_{ij}$, where $\boldsymbol{q} = \boldsymbol{k}\sqrt{\epsilon_{eff}}$ is the diffracted beam wavevector, ϵ_{eff} is the effective dielectric constant of the lattice, $|\mathbf{k}| = 2\pi/\lambda$ is the wavevector of the incident light, θ is its angle of incidence with respect to the lattice surface normal, and g_{ij} are the lattice wavevectors. Herein, g_{ij} are indeed the SC reciprocal vectors $\mathbf{G}_{ij}^{(t)}$. At normal incidence, diffraction mediated LSPs can be excited when $\mathbf{k}^{(t)}\sqrt{\epsilon_{eff}} = \pm\mathbf{G}_{ij}^{(t)}$. We predict a set of four-fold degenerate LSP resonances, due to the square lattice symmetry, emerging in the Au SC optical spectra at self-similar and power-law dependent wavelengths (i.e., critical modes[51])

$$\lambda_n^{(t)} = \frac{a_0 8^{-n/d_H}}{\sqrt{i^2 + j^2}}\sqrt{\epsilon_{eff}} \tag{4.3}$$

Where $n \in [1, t]$ is the n^{th} resonance at the t^{th} fractal order. Figure 4.9a, shows the zeroth-order (the incident and detected light are collinear) extinction (1 − T) spectra of the Au SCs exhibiting multiple resonances in the VIS-MIR range.

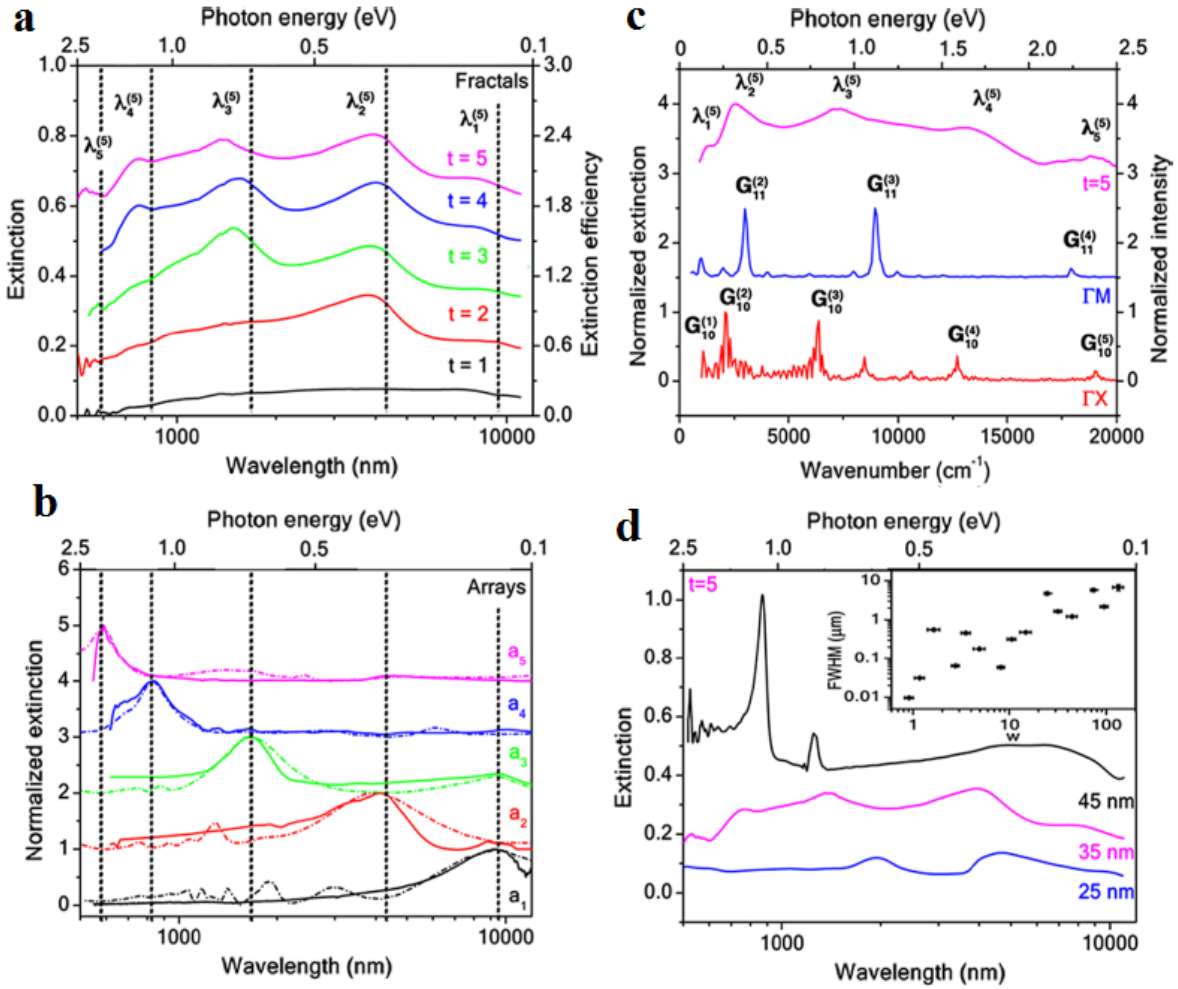

Fig 4.9: a) Experimental Extinction and extinction efficiency spectra of $\mathbf{35 \pm 3}$ nm thick SCs for t = 1 - 5. Extinction peaks $\boldsymbol{\lambda_n^{(5)}}$ are marked. **b)** Experimental (solid curves) and calculated (dash-dot curves) normalized extinction of $\mathbf{35 \pm 3}$ nm thick Au periodic arrays with lattice constants a_t. Dashed lines indicate the array LSPs. Curves in a and b are offset by 0.15. **c)** Normalized extinction spectrum of SC at t = 5 (magenta solid curve) and normalized intensity of the points in the SC fast Fourier transform in Fig 4.7b, along the $\Delta = \overline{\Gamma X}$ (red solid curve) and $\boldsymbol{\Sigma} = \overline{\Gamma M}$ (blue solid curve) directions. Curves are offset by 1.5. Note that the SC Fourier spectra are converted into photon energy units by ħω = ħkc. Extinction peaks $\boldsymbol{\lambda_n^{(5)}}$ and reciprocal vectors $\mathbf{G_{10}^{(t)}}$ are marked. **d)** Extinction spectra of SCs for t = 5 with thicknesses $\mathbf{25 \pm 3}$ nm (blue solid curve), $\mathbf{35 \pm 3}$ nm (magenta solid curve), and $\mathbf{45 \pm 3}$ nm (black solid curve). Inset: FWHM of the LSP modes as a function of aspect ratio *w* in log-log scale.

The extinction efficiency (i.e., the extinction divided by the total area of the fractal) of the resonances is up to 185%, thus showing an extraordinary extinction.[295]

It can be noted while comparing extinction spectra of periodic arrays that the position of the SC resonances scales linearly along with the lattice constant *a* as represented in Fig 4.9b. The SC resonances are blue-shifted with respect to those of the periodic arrays, due to the coupling between the squares belonging to the different fractal orders.

As depicted in Fig 4.9c, the position of the resonances in the SC extinction correspond to the first reciprocal lattice vector $G_{10}^{(t)}$ of each fractal order. However, such modes occur at slightly smaller wavenumbers than the Fourier peaks in the $\overline{\Gamma X}$ and $\overline{\Gamma M}$ directions obtained from Fig 4.7b (i.e., at wavelengths slightly larger than the lattice constants a_t); thus confirming that the origin of such resonances in the Au SC extinction spectra is not due to a diffraction mechanism, but to diffraction-mediated LSPs.

Figure 4.9d presents variation of extinction spectra for Au SC at t = 5 when thickness changes from 25 ± 3 nm to 45 ± 3 nm. In order to obtain a large extinction, the metal must be optically thick, which implies that the film thickness must be several times the skin depth of the metal.[289] Typical skin depths are on the order of 30−170 nm for Au in the VIS-MIR range. It is observed that increasing thickness results in sharp Fano-resonances in place of broad peaks as shown in Fig 4.10a. This suggests that the FWHM of the LSPs depends on the aspect ratio (i.e., lateral size to thickness) $w_t = L_t/h$.[291] As this ratio approaches unity, the resonance becomes sharper the as shown in inset of Fig 4.9d and the sharpest resonance occurs when the particle is isotropic (i.e., a cube), while the broadest

when it is oblate. In Fig 4.10a, we fitted the extinction resonances for 45 nm thick SC for t = 5 with the Fano total scattering cross-section[296]:

$$\sigma = \frac{\left(\frac{q\Gamma}{2} + \omega - \omega_0\right)^2}{\left(\frac{\Gamma}{2}\right)^2 + (\omega - \omega_0)^2} \tag{4.4}$$

With Γ the resonance width, ω_0 the resonance center, and q the Fano parameter, which measures the ratio of the scattering amplitudes related to the two different modes. The fit returns $q_1 = 0.9 \pm 0.2$ (dipole), $q_2 = 1.3 \pm 0.2$ (dipole), $q_3 = 3.5 \pm 0.1$ (quadrupole), and $q_4 = 7.9 \pm 0.4$ (octapole) Fano parameters.

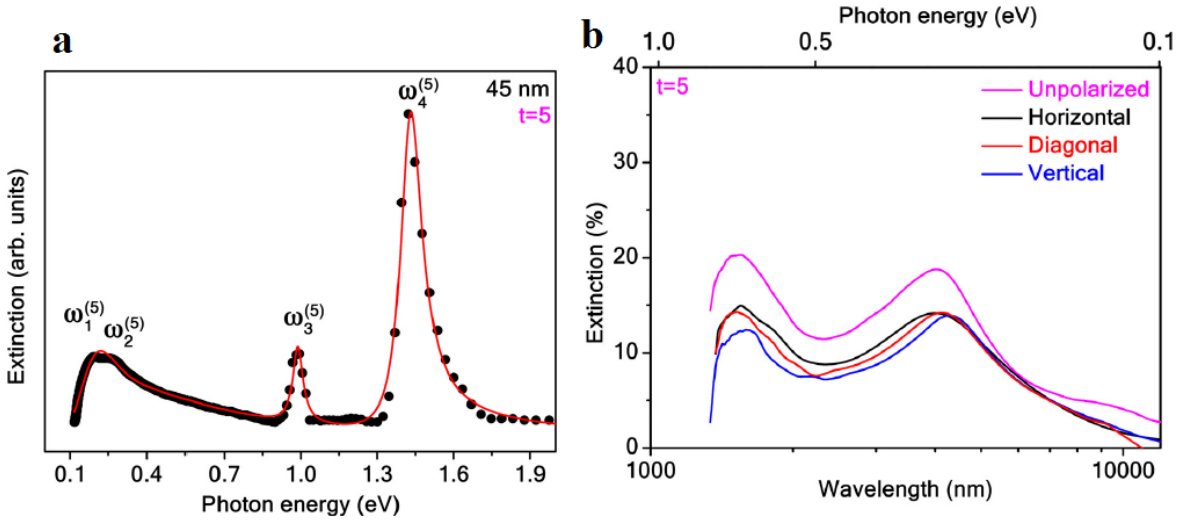

Fig 4.10: a) Experimental extinction spectrum of a 45 nm thick SC for t = 5. Fit of the $\omega_1^{(5)}, \omega_2^{(5)}, \omega_3^{(5)}$, and $\omega_4^{(5)}$ resonances with the Fano function (red solid curve). **b)** Experimental extinction spectra of SCs at t = 5 for unpolarized light and horizontal, diagonal, and vertical polarization.

Furthermore, polarization dependent optical properties of Au SCs at t = 5 is investigated. Figure 4.10b represents extinction spectra for unpolarized light and horizontal, diagonal, and vertical polarization, suggesting that Au SCs are insensitive to the linear and diagonal

polarization of the incident light, having a centrosymmetric geometry. This is an important feature in order to realize polarization-independent devices, since other fractal geometries[45,51,68,77,297] and conventional plasmonic structures[2,289] usually depend strongly on light polarization.

The SC optical spectrum at a given fractal order t exhibits n = t resonances with the wavelength $\lambda_n^{(t)}$ corresponding mainly at the first order of diffraction $(i,j) \equiv (1,0)$. Of such resonances, n - 1 refer to the SC at order t - 1, but shifted by a factor proportional to a_t^{-1} owing to the far-field diffraction coupling among the increased number of squares.[2] In Fig 4.11a, the wavelengths of SC extinction peaks $\lambda_n^{(t)}$ are shown for each fractal order obtained experimentally along with the calculated data for $\lambda_n^{(5)}$.

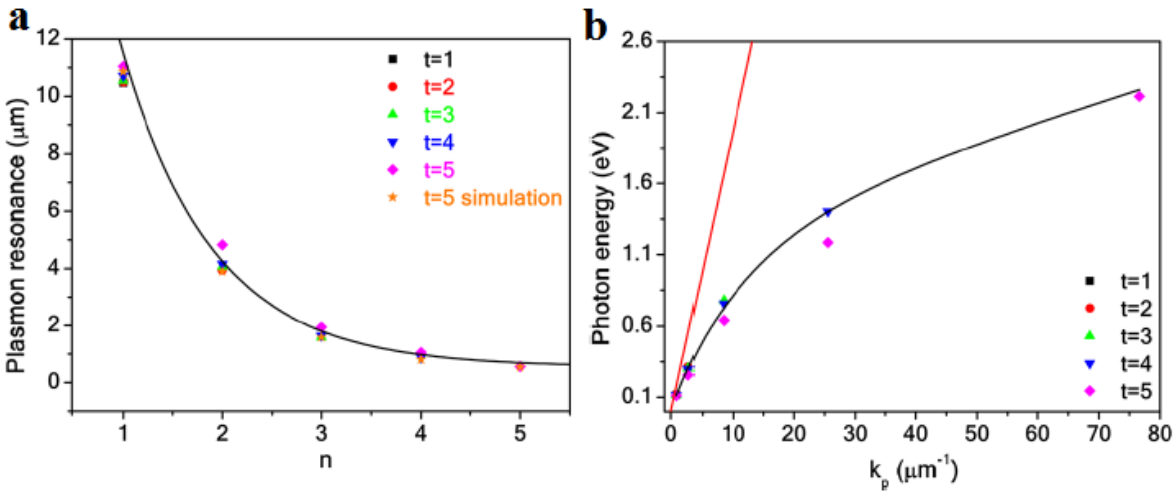

Fig 4.11: a) Experimental LSP resonances $\boldsymbol{\lambda_n^{(t)}}$ as a function of their index n. Black solid line is the best fit of the experimental data given by equation 4.3, which is in agreement with electromagnetic simulations for $\boldsymbol{\lambda_n^{(5)}}$ (orange star). The fit gives $d_H = 1.92 \pm 0.04$. **b)** Experimental and calculated (black curve) LSP resonances as a function of LSP wavevector $k_p = \pi/L_t$. The red line represents the free-space dispersion of light $\hbar\omega = \hbar kc$.

The best fit of the experimental data that are in good agreement with the electromagnetic simulations is given by Equation 4.3, by setting $(i,j) \equiv (1,0)$. The fit returns a fractal

dimension $d_H = 1.92 \pm 0.04$. As predicted, such LSP resonances are self-similar as their wavelength has the same scale-invariance law ($\mathcal{L}_t = 8^{-t/d_H}$) as the SC, depending on the fractal dimension as an exponential law. From the data in Fig 4.9a, we can plot the dispersion relation of diffraction-mediated LSP modes (Fig 4.11b). Here, $k_p = \pi/L_t = 3\pi/a_t$ is the LSP wavevector of the SC. It follows also that kp is self-similar.

4.2.2 Electromagnetic simulations

Figure 4.12 shows simulated electric near-field enhancement E_z/E_0 contour plots for t = 1 - 4 at their LSP resonances. The results suggest a resonant excitation of coupled dipolar antennas centered on the elements constituting the fractal that extends across the entire geometry. The system exhibits hot spots localized on a sub-wavelength scale, resulting in additional plasmonic modes at shorter wavelengths while increasing the fractal order. This mechanism provides a hierarchical multiscale of hot spots that transfer the excitations towards progressively smaller length scales, exhibiting large values of electric near-field enhancement. As a consequence of the SC fractal scaling, the hot spot distribution of the resonant modes is self-similar. With an increasing fractal order and thereby the number of squares, a redistribution of the electric near-field intensity occurs.

As a result, two main phenomena can be observed: 1) a red-shift at a given LSP wavelength along with a decrease of its electric near-field intensity. As already stated for the far-field optical spectra, this is attributed to the coupling among additional structural elements that are introduced in the system, with the difference that near-fields couple by dipolar interactions. 2) New LSP modes arise at shorter wavelengths with higher intensity.

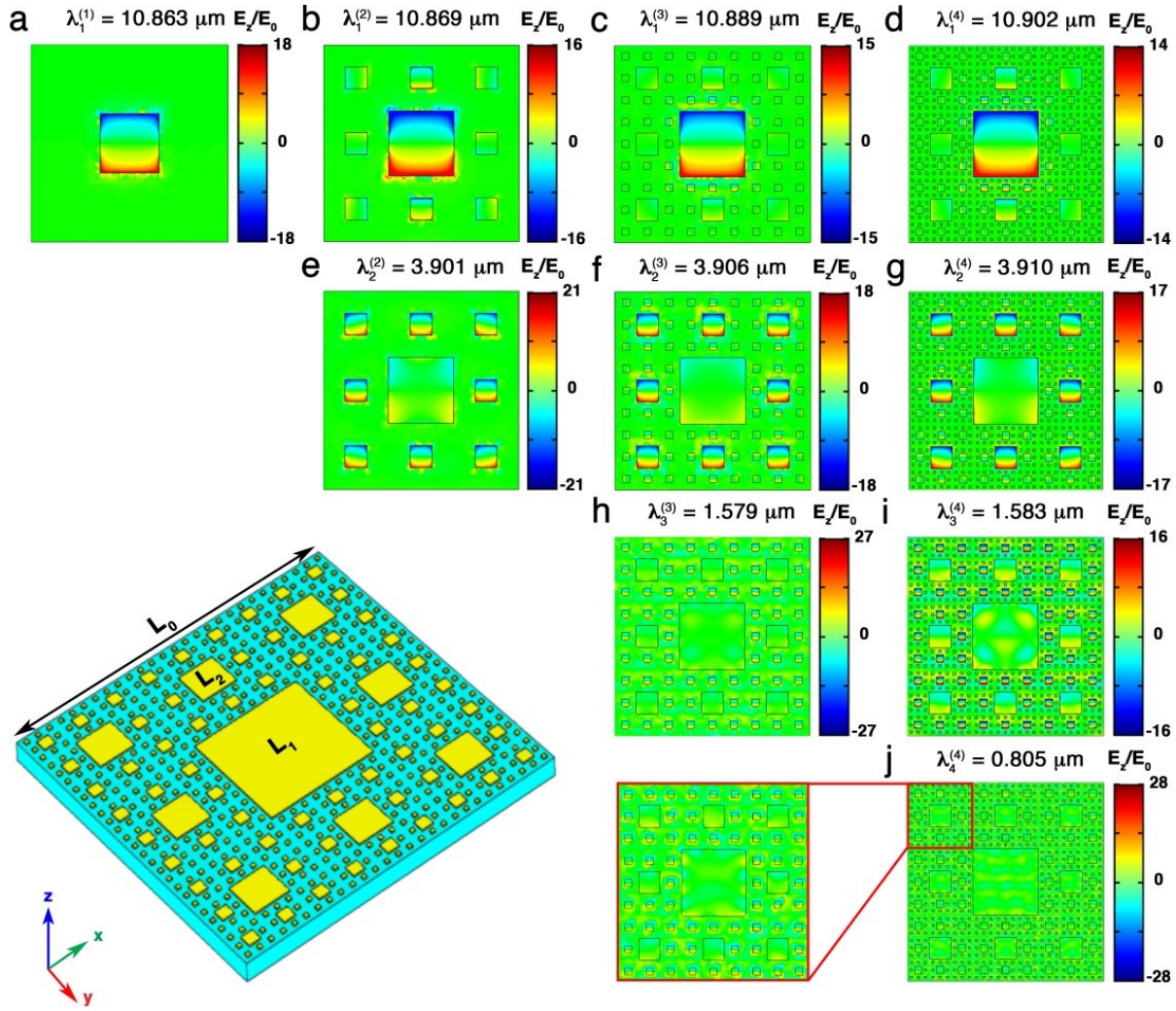

Fig 4.12: Electromagnetic simulations of plasmonic Au SCs. Simulated electric near-field enhancement (E_z/E_0) distribution of SCs for orders t = 1 - 4 (from left to right) at their resonances $\boldsymbol{\lambda_1^{(t)}}$ (**a-d**), $\boldsymbol{\lambda_2^{(t)}}$ (**e-g**), $\boldsymbol{\lambda_3^{(t)}}$ (**h-i**), and $\boldsymbol{\lambda_4^{(t)}}$ (**j**). The incident electric-field E_0 is polarized vertically and the phase is set to π/4 in order to maximize the field intensity. Each distribution is normalized to its maximum value. Inset shows a sketch of the modeled Au SC deposited on a CaF_2 substrate.

4.2.3 Surface enhanced Raman effects

We investigated the Au SC electric nearfield spatial distributions by SERS measurements on a thin layer (12 ± 2 nm) of Brilliant Cresyl Blue (BCB) dye [$(C_{17}H_{20}ClN_3O)_2\,ZnCl_2$], deposited on Au SCs. Fig 4.13a shows average Raman spectra acquired on the samples at λ_{ex} = 633 nm for t = 1 - 5 and for an unpatterned Au film as a reference. This excitation wavelength is resonant with the dye (Fig 4.13b). The band at 800-1000 cm^{-1} is due to the Si/SiO_2 substrate on which SCs are patterned. We observe a series of vibrational bands arising from the molecule with an increasing intensity as a function of the fractal order. It can be seen that the enhancement of Raman signal corresponding to higher orders of SCs is much stronger than that of the reference Au film, thus confirming the effective ability of the plasmonic hot spots of Au fractal to focus the electric-field.

We chose the strongest BCB vibrational band ω^* = 1655 cm^{-1}, which corresponds to the coupling of NH_2 scissor mode with the asymmetric stretch mode of C rings[298] to evaluate the maximum SERS enhancement factor EF_{sers}. EF_{sers} is is calculated by the relation:

$$EF_{sers} = \frac{\langle I_{sample}\rangle}{\langle I_{Au}\rangle}\frac{\langle A_{Au}\rangle}{A_{sample}N_{sample}} \qquad (4.5)$$

where $\langle I_{sample}\rangle$ is the average Raman intensity in adu units (1 adu = 1 count/mWs) at ω^* = 1655 cm^{-1} measured over the SC maps, A_{Au} = 0.785 μm^2 is the area of the laser beam spot on the reference Au film, $A_{sample} = L_t^2$ is the area of the smallest square of the fractal at order t for which the Raman enhancement is maximum, N_{sample} is the number of the smallest squares within the beam spot area, and $\langle I_{Au}\rangle$ is the average Raman intensity in adu units at ω^* measured over the map of the ideally smooth reference Au film.

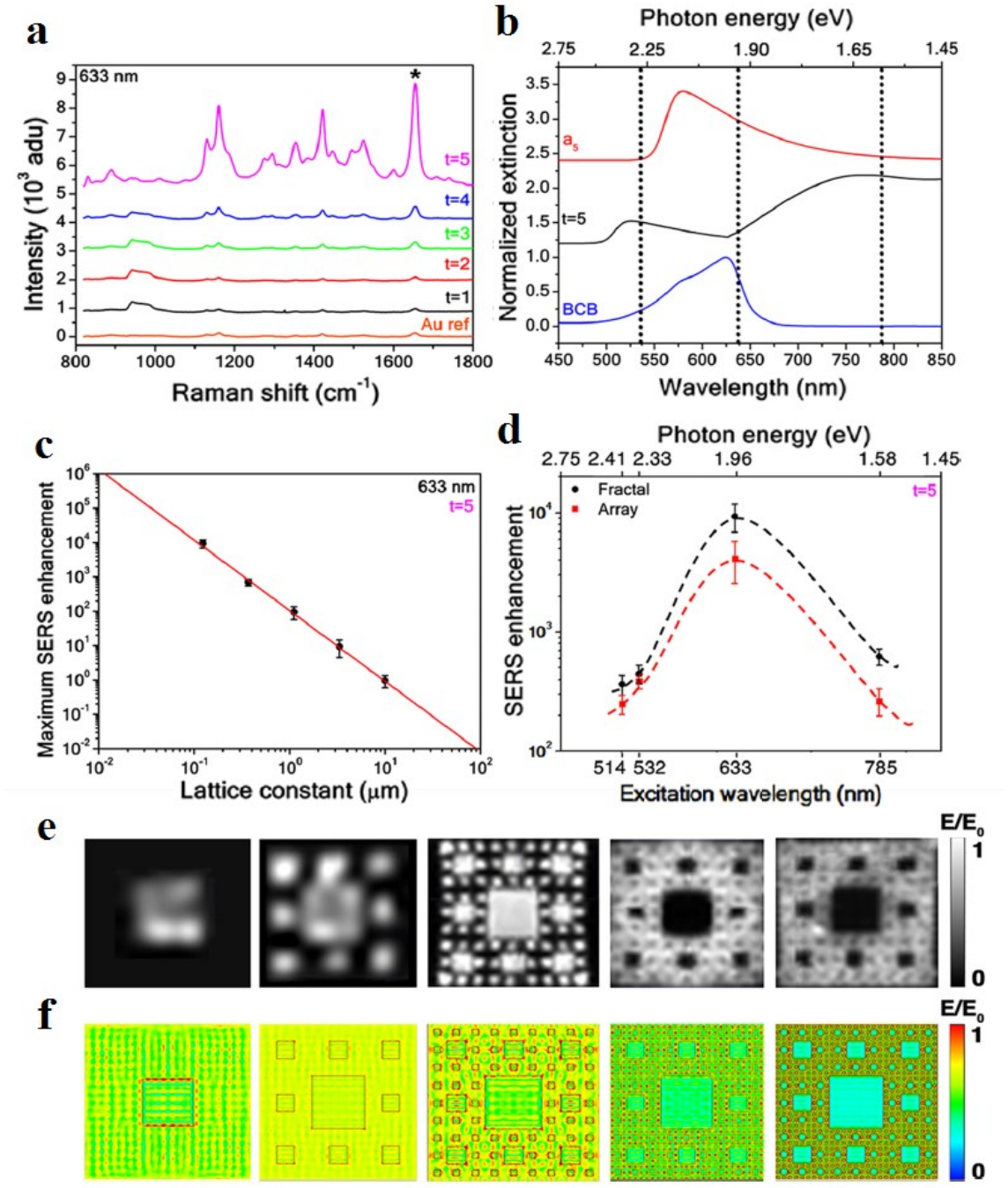

Fig 4.13: **a)** Raman spectra at λ_{ex} = 633 nm of BCB deposited on the SC for t = 1 - 5 and on a reference Au film. **b)** Normalized extinction spectra of BCB (blue curve), SC at t = 5 (black curve), and periodic array at L_5 (red curve). Dotted lines represent λ_{ex}. Curves are offset by 0.2 in a and b. SERS enhancement of the BCB vibrational mode ω^* = 1655 cm^{-1} at λ_{ex}=633 nm as a function of a_t in log-log scale **(c)** and as a function of λ_{ex} for the SC at t = 5 and periodic array at L_5 **(d)**. Dashed lines are guides for the eyes. Experimental electric-field enhancement E/E_0 maps of ω^* at λ_{ex} = 633 nm for t = 1 - 5 of the SC **(e)** and electromagnetic simulations of E/E_0 **(f).** Each map is normalized to its maximum value.

In Fig 4.13c, EF_{sers} value as a function of lattice constant a_t of the fractals at λ_{ex}=633 nm is shown, while that of the fractal at t = 5 as a function of the incident wavelength is reported in Fig 4.13d.

We found that EF_{sers} increases with the fractal order as a power law. Despite the fact that BCB is resonant at λ_{ex} = 633 nm, for orders t = 1 − 3 the enhancement factor is very small as no LSP mode is in resonance (Fig 4.13b). For orders t = 4 - 5, EF_{sers} is highest as the excitation wavelength is resonant not only with the dye but also with LSP resonance of the SC. The resonant EF_{sers} obtained at λ_{ex} = 633 nm is about 10^4, whereas in non-resonant case, for instance at λ_{ex} = 785 nm, it is about 10^3 (Fig 4.13d). This means a maximum electric-field enhancement factor of about 10 is provided in the resonant case, while it is about 5 in the non-resonant case. As the latter factor is not affected by the dye fluorescence, this is purely a surface-enhanced electromagnetic effect. We infer that the plasmonic fractal has a broadband EF_{sers}, which is about twice higher in absolute value than an equivalent periodic array (Fig 4.13d), and such a structure could be used for multiplexing experiments with several arrays absorbing in different ranges of the electromagnetic spectrum.

Fig 4.13e reports spatial distributions of electric-field enhancement E/E_0 as obtained from the Raman intensity maps of ω^* at λ_{ex} = 633 nm, normalized to the reference Au film for t = 1 - 5. It is clear that smaller the element size, larger the electric-field localization occurring on it due to LSPs supported by the Au structures, which decays rapidly outside the squares. The contour plots present a maximum of contrast distributed over the elements for the fractals for t = 1 - 3 orders however, for t = 4 - 5, a large

enhancement of the electric-field is shown in between the structures of the previous orders, respectively in correspondence of the squares with size L_4 and L_5. For instance, the intensity profile across the map at t = 5 changes of a factor ≈ 10 from the central square L_1 to the surrounding smaller squares (Fig 4.14).

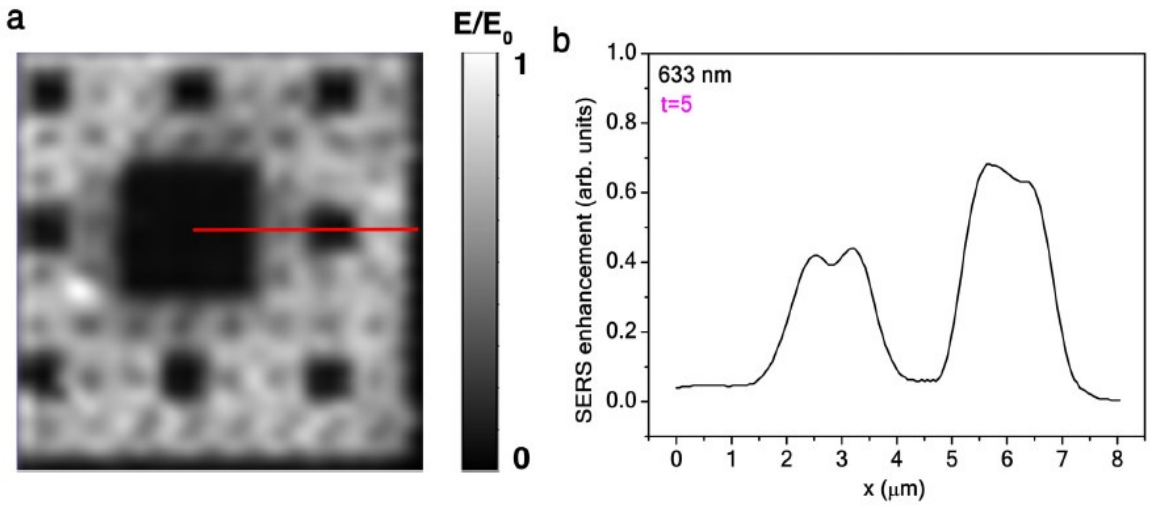

Fig 4.14: a) Experimental electric-field enhancement E_z/E_0 distribution of a SC for fractal order t = 5. **b)** Cross section of the map along the marked solid red line.

Note that since the resolution of the laser beam spot is 0.785 μm^2, the instrument averages out over the structures L_4 and L_5. Our results are in good agreement with those obtained by FEM simulations shown in Fig 4.13f. The simulated map for t = 5 has a maximum value of the electric-field enhancement $E/E_0 \approx 13$ on L_5 squares at λ_{ex} = 633 nm, which is comparable with the experimental value obtained $EF_{sers}^{1/4} \approx 10$.

4.3 Au/G Sierpinski carpets

Here the fabrication and study of Au SC deposited on graphene is presented. Design and realization of such novel Au/G hybrid fractals offer enhanced light - graphene interactions due to higher field localization. Figure 4.15 shows the first five orders of the Au SC deposited on a CVD-grown, single-layer, single-crystal graphene transferred on a Si/SiO_2 substrate. The methodologies followed to generate SCs are the same as described in section 4.2 while the design and fabrication of SC is explained in section 3.2.

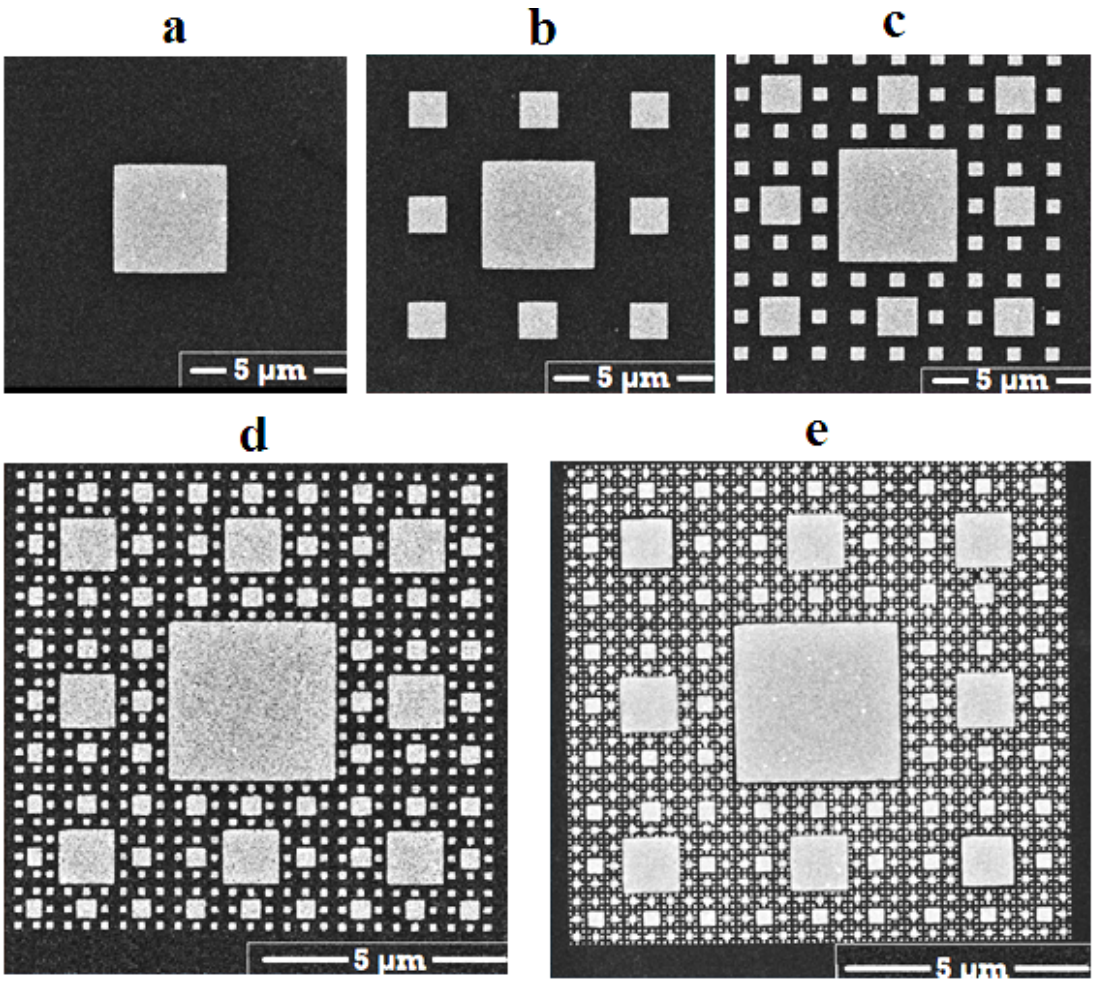

Fig 4.15: SEM images of Au SC on CVD grown graphene deposited on Si/SiO_2 substrates for fractal orders t = 1 **(a)**, t = 2 **(b)**, t = 3 **(c)**, t = 4 **(d)** and t = 5 **(e)**.

Electrical characterization of our samples is carried out by designing and fabricating FETs for order t = 0 – 5 (t = 0 represents bare graphene). The optical properties of Au/G fractals and their gate voltage dependence are measured using an FTIR spectrometer in reflection mode. A plasmonic multimodal spectral response from the VIS to MIR range similar to that of Au SC is observed. Dynamic control of optical properties by is demonstrated by changing the gate voltage. The peculiar optical properties are exploited to build a photodetector with broadband photoresponse, showing an enhancement factor about 10 over a bare graphene photodetector. Furthermore, SERS is carried out in our samples indicating large enhancement of the Raman signal up to 10^5, which tend to be progressively localized around the smallest Au squares. These results are presented in the following sections.

4.3.1 Electrical properties

Figures 4.16a,b show schematic and optical image of the representative Au/G FET. The channel consists of a 40 x 40 μm CVD-grown single-layer graphene flake sensitized with t = 1 - 5 orders of Au SCs. In the following parts I_{SD}, V_{SD}, V_G and V_{CNP} are used to denote source-drain current, source-drain voltage, applied gate voltage and charge neutrality point voltage respectively. Generally in a metal/graphene system, the metal causes Fermi level to move away from the Dirac points in graphene leading to doping with either electrons or holes, with the sign and amount of doping determined by the difference of metal and graphene work functions and interfacial interactions.[299,300] The band diagram of Au/G junction in equilibrium is shown in Fig 4.16c. A shift of graphene Fermi level is depicted due to difference in Fermi levels of graphene and Au contact

electrode. The work functions of graphene and Au are considered to be $\Phi_G \sim 4.5$ eV [Ref. 203] and $\Phi_{Au} \sim 4.8$ eV [Ref. 269]. As the work function of Au is larger than that of graphene, Au acts as an effective hole doping. This results in a p-doping for graphene which is relatively heavier closer to the Au contact and lighter farther away from it. Note that the small density of states in graphene near the Dirac energy causes a the large shift of the Fermi level even for limited charge transfer.[301,302] Figure 4.16d shows V_{SD} - I_{SD} plot for V_G = -100 V, indicating a linear relationship for all fractal orders, suggesting an ohmic contact between Au and graphene.

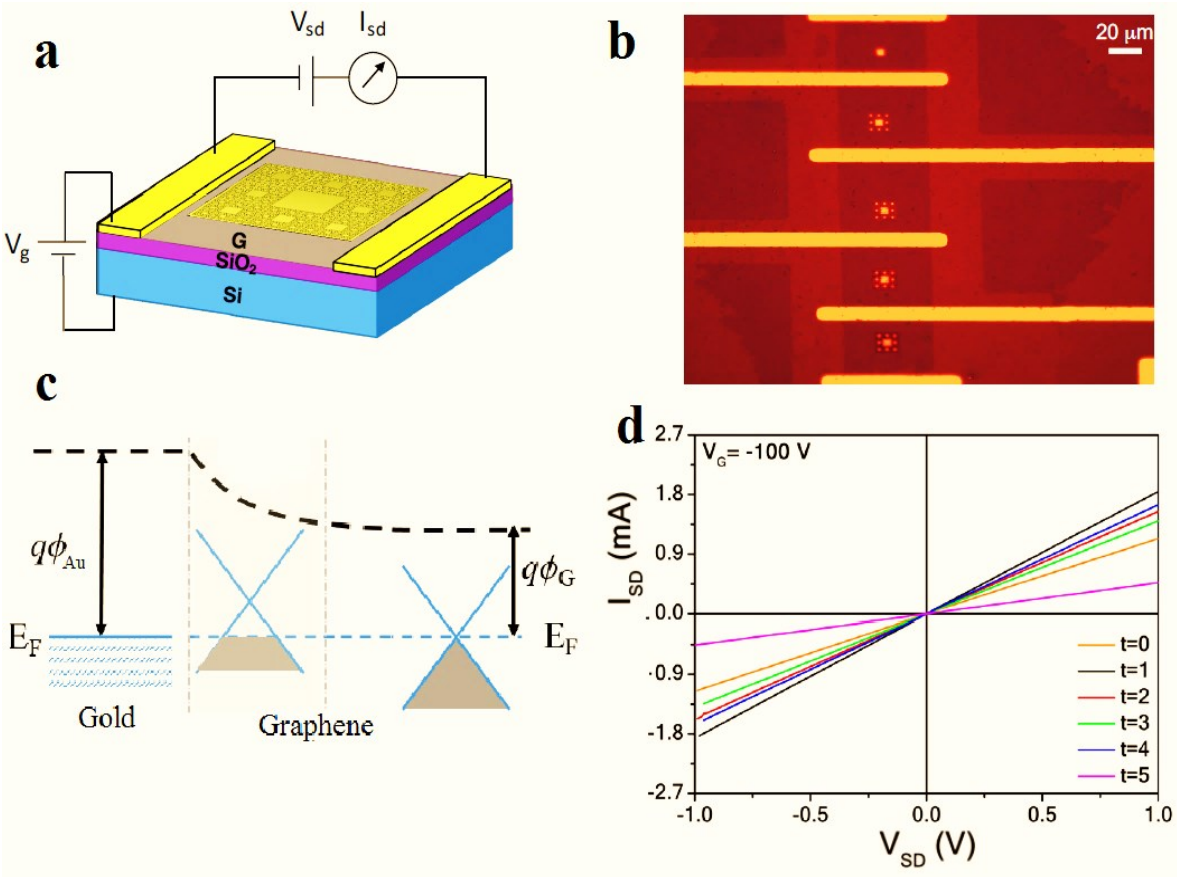

Fig 4.16: a) Schematic diagram of Au/G FET with a fractal order t = 5. **b)** Optical image of Au/G FET for t = 1 – 5 (top to bottom, in the same order) (scale bar = 20µm). **c)** Band diagram of the graphene-Au junction at thermal equilibrium. E_F is the junction Fermi energy at equilibrium. **d)** I_{SD}-V_{SD} curve at V_G = -100 V for t = 0 – 5.

The total resistance (R_{total}) of FET consists of contributions from graphene channel resistance, and contact resistance (R_C) from graphene-metal junction which is estimated from four probe measurements, are related by:[273]

$$R_{total} = 2R_C + \frac{L}{W}R_{sheet} \qquad (4.6)$$

Where L is length of the graphene channel, W is width of the graphene channel, and R_{sheet} is the sheet resistance of graphene; $R_{sheet} = \frac{1}{\mu n(V_G - V_{CNP})}$. Here μ denotes carrier mobility, *n* is the carrier density, and V_G and V_{CNP} are applied gate voltage and Dirac point voltage respectively. The gate dependent carrier density is given by:

$$n(V_G - V_{CNP}) = \sqrt{n_0^2 + \left(C_g|V_G - V_{CNP}|\right)^2} \qquad (4.7)$$

Where n_0 is residual charge density and C_g is the back-gate capacitance per unit area of FET, i.e., the capacitance of SiO_2 layer, given by $C_g = \varepsilon_r\varepsilon_0/t = 1.2 \times 10^{-4}$ Fm^{-2}, where ε_r is relative permittivity of SiO_2 and ε_0 is the permittivity of vacuum. Thickness of SiO_2 layer is t = 285 nm.

The transfer characteristics of our devices are obtained by recording I_{SD} for gate-voltage sweep with V_{SD} = 0.1 V in vacuum, revealing several trends with increasing fractal order. The dependence of resistivity on the gate voltage shift is presented in Fig 4.17a for fractals with t = 0 – 5. The gate voltage shift represents the shift of $V_G - V_{CNP}$ at a given fractal order with respect to $V_G - V_{CNP}$ of t = 0. Each curve shows a maximum value at $V_G = V_{CNP}$ due to the charge neutrality.

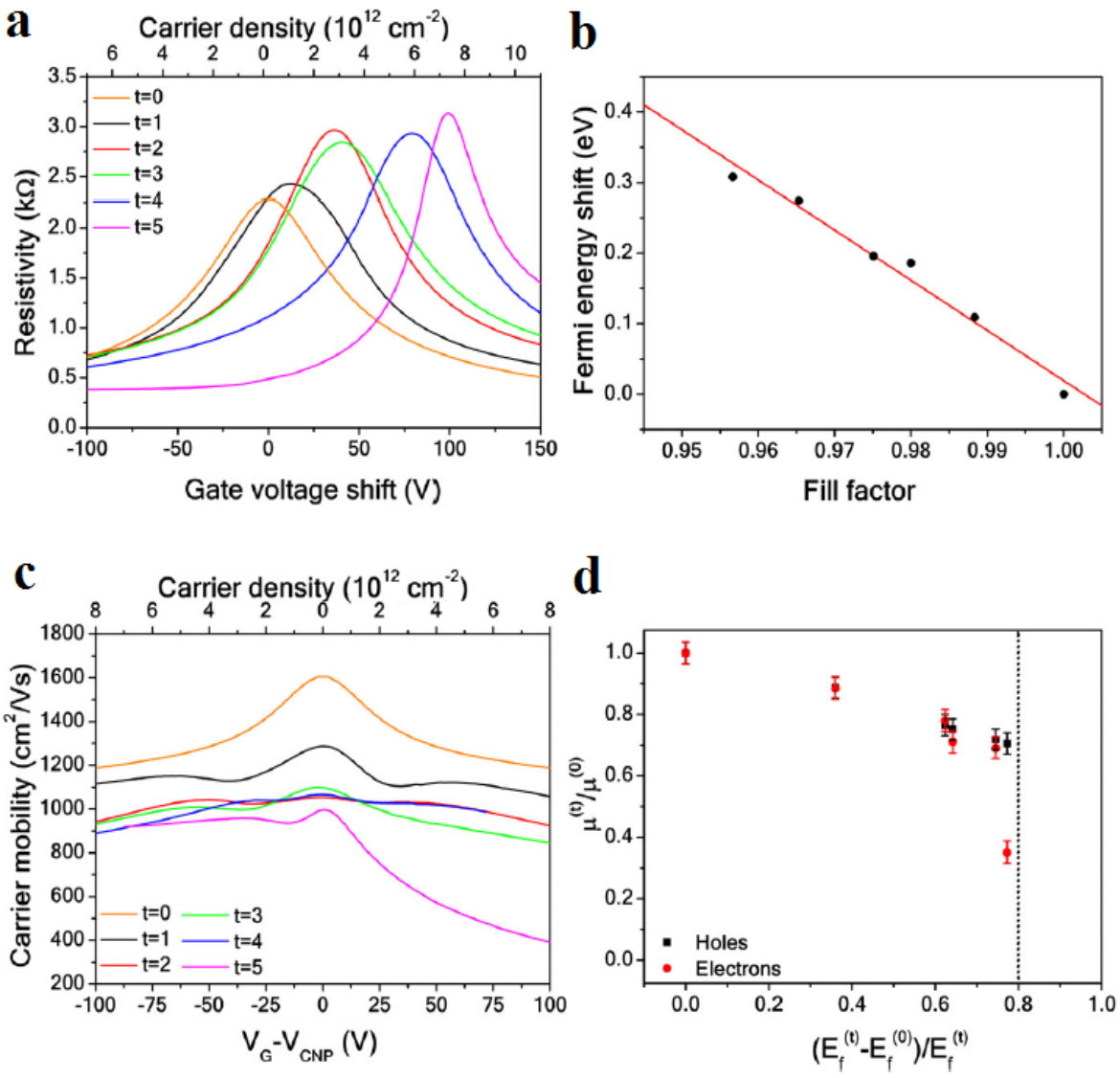

Fig 4.17: **a)** Resistivity at V_{SD} = 0.1 V of Au/G fractals for t = 0 – 5 as a function of the gate voltage shift and carrier density with respect to the unpatterned graphene device (t = 0). **b)** Dependence of Fermi energy on the fill factor. Red solid line shows linear fit to the data. **c)** Carrier mobility at V_{SD} = 0.1 V of Au/G fractals for t = 0 – 5 as a function of the relative gate voltage to the CNP and carrier density. **d)** Normalized mobility at 6x10^{12} cm^{-2} of Au/G fractals for t = 0 – 5 to the value for t = 0 as a function of the relative Fermi energy shift to the value for t = 0.

The charge neutrality point (CNP) shifts towards more positive voltages with increasing fractal order, attributed to increased p-type doping induced by Au. The graphene Fermi energy $E_F = \hbar v_F \sqrt{\pi n}$ is modified by the doping introduced by Au, which is visualized with respect to the Fermi energy of bare graphene in Fig 4.17b as a function of fill factor. Here, we define the fill factor, $1 - S_t/S_G$, as the area fraction of graphene not covered by Au (i.e., fill factor = 1 represents bare graphene). The shift of Fermi energy toward positive voltages follows a linear trend as the fill factor decreases, which in turn is due to the higher carrier concentration in graphene introduced by Au in higher fractal orders.

Carrier mobility is plotted in Fig 4.17c as a function of $V_G - V_{CNP}$ for different fractal orders t = 0 – 5 at V_{SD} = 0.1 V. Clearly, carrier mobility decreases with increasing fractal order. Between orders t = 0 and t = 5, a significant difference in mobility, reaching up to 750 cm^2/Vs is observed. To better visualize the effect of Au, the variation of mobility as a function of the Fermi energy shift induced by the fractals with respect to the unpatterned graphene (t = 0) is plotted in Fig 4.17d. Here the electron and hole mobilities are shown for t = 0 – 5 normalized to the value for t = 0 $\left(\text{i.e.}, \mu^{(t)}/\mu^{(0)}\right)$, as a function of the relative Fermi energy shift to the value for t = 0 $\left(\text{i.e.}, (E_f^{(t)} - E_f^{(0)})/E_f^{(t)}\right)$. Evidently, both electron and hole mobility monotonically decreases with relative Fermi energy shift. The reduced mobility can be attributed to increased concentration of Au adsorbed on the graphene surface which acts as sources of additional scattering for charge carriers.[268,303–305]

4.3.2 Optical properties

Optical spectroscopy is performed with unpolarized light in our Au/G FETs by FTIR spectrometer. We compare the results with that of Au fractals and present in Figs 4.18a-d. In-situ tuning of optical spectra is achieved varying back-gate voltage as shown in Fig 4.18e,f.

Figure 4.18a shows reflectance spectra for Au fractal and Au/G fractal at order t = 5 with Si/SiO_2 spectrum as reference. Both the spectra exhibit multiple features in the VIS - MIR region, which for the Au SC appear as maxima due to the radiative scattering in air, while for the Au/G SC result in red-shifted minima owing to the quenching electronic energy transfer from the Au scatterers to graphene.[306] The sharper and pronounced intensity of LSP dip at ω_3 could be due to the fact that it overlaps with graphene interband absorption threshold $2E_F$. The resonances corresponding to Au/G fractal appears to be red-shifted compared to that of Au fractal, suggesting an effective coupling between Au LSPs and graphene. The observed behavior, which has been extensively reported in literature[172,180,307–311] could be originating from polarizability variation of the local environment of Au structures that gives rise to image-dipole charges in graphene. This image-dipole reduces the internal field in the Au structures, resulting in a red shift of the resonance wavelength.[307–310,312] Also, there is a general decrease in the Au/G SC reflectance throughout the analyzed spectral range from that of Au SC, due to enhanced light absorption of graphene. Plasmon resonance position is plotted in Fig 4.18b as a function of the lattice constant a_t for Au and Au/G fractals. A linear correlation is observed for Au squares as expected from its self-similar optical response (Section 4.2.1)

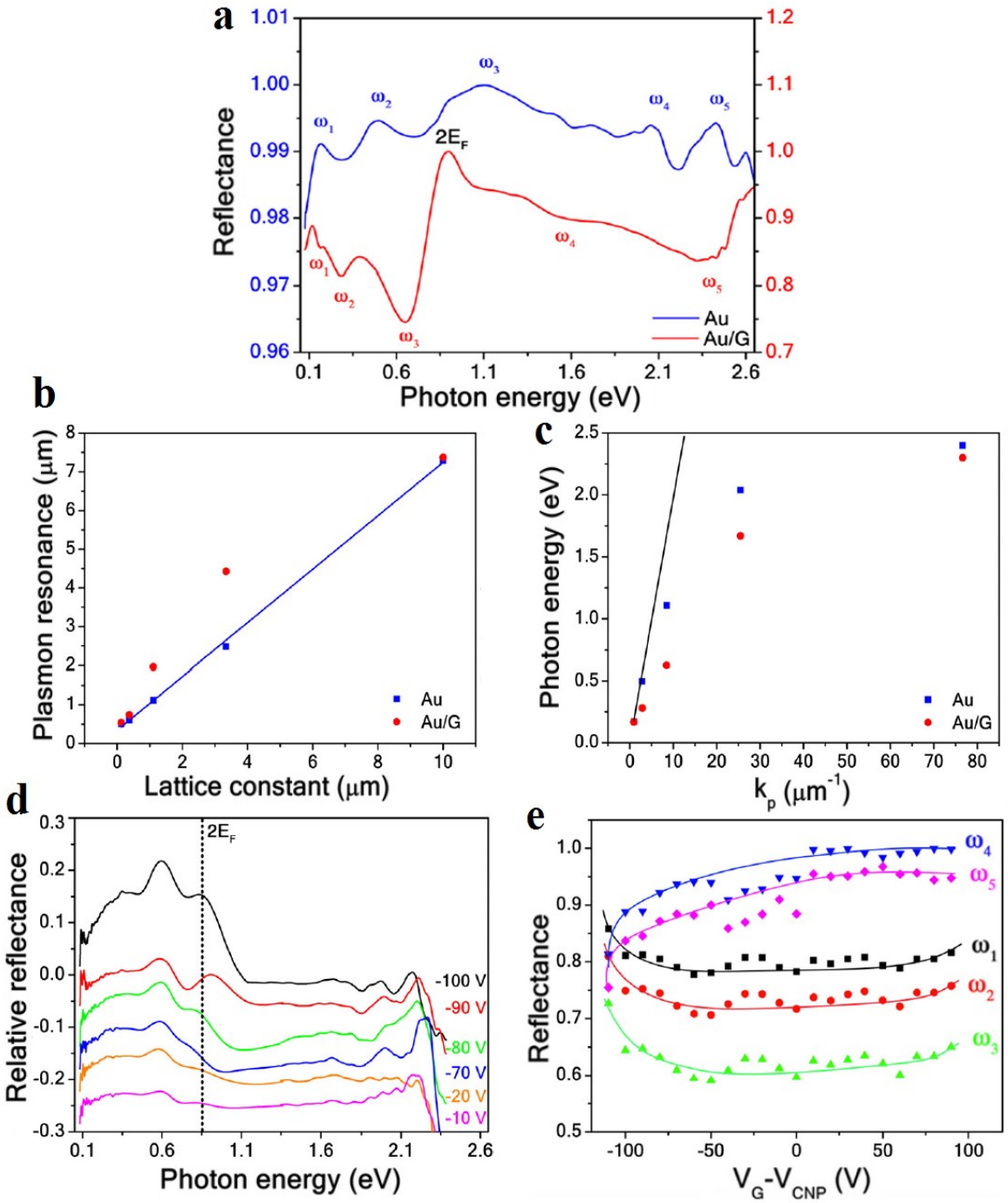

Fig 4.18: a) Experimental reflectance spectra of 35±3 nm thick Au and Au/G SCs for order t = 5. Reflectance dips due to Au LSP modes $\boldsymbol{\omega_n}$ are marked along with the graphene interband absorption threshold ($2E_F$). LSP resonances of Au and Au/G fractals as a function of the lattice constant **(b)** and as a function of LSP wavevector **(c)**. **d)** Relative reflectance of the Au/G SC at t = 5 for different gate voltages. $2E_F$ level at V_G = -100 V is marked. **e)** Reflectance of the LSP modes for the Au/G SC at t = 5 as a function of the relative gate voltage to the CNP. Solid curves are guides for the eyes.

while for Au/G, the dependence is nonlinear, resembling a square root function, i.e., $\lambda_t \propto a_t^{1/2}$. This might be attributed to the characteristic 2-dimensional plasmon dispersion in graphene.[7] Dispersion relation of LSP modes is shown in Fig 4.18c for Au and Au/G fractals, where the LSP wavevector of the SC is given by $k_p = \frac{\pi}{L_t} = \frac{3\pi}{a_t}$. The black line represents the free-space dispersion of light, $\hbar\omega = \hbar kc$.

Tuning of LSP resonances in Au/G fractal through electrostatic gating is demonstrated in Fig 4.18d for t = 5 for a range of gate voltage from -10 V to -100 V. The relative reflectance is defined as $R' = [R(V_G) - R(V_{CNP})]/R(V_{CNP})$ where R (V_G) and R (V_{CNP}) are reflectance at a given gate voltage and that at CNP voltage respectively. Clearly, applying larger negative V_G result in a significant increment in reflectance intensity which indicates reduced absorption in graphene caused by gate dependent carrier dynamics. The effect of gate voltage on relative reflectance becomes stronger as the frequency shifts towards NIR, showing about 30% increase in reflectance at ~ 0.6 eV. In order to distinguish the impact of gate voltage on each LSP mode, we plot the reflectance for ω_1 – ω_5 as a function of $V_G - V_{CNP}$ in Fig 4.18e. For ω_1 – ω_3, which lies below the double Fermi level, the increase of negative and positive gate voltages (i.e., holes and electrons carrier densities respectively) leads to slight increase of reflectance as a consequence of reduced absorbance while for ω_4 and ω_5 above the Fermi level, an increase of negative voltages or hole density leads to a decrease of reflectance as a consequence of enhanced absorbance. This might be due to different coupling mechanisms between the Au LSP modes and graphene, which is dependent on the Fermi energy. We note that complete understanding of this phenomenon requires further investigation, both experimental and theoretical.

4.3.3 Surface enhanced Raman effects

We employed Raman measurements on the Au/G SC in order to probe the electric near-field spatial distributions and the measurements indicate significant field enhancement in the vicinity of graphene due to plasmonic Au SC. The results are presented in following sections.

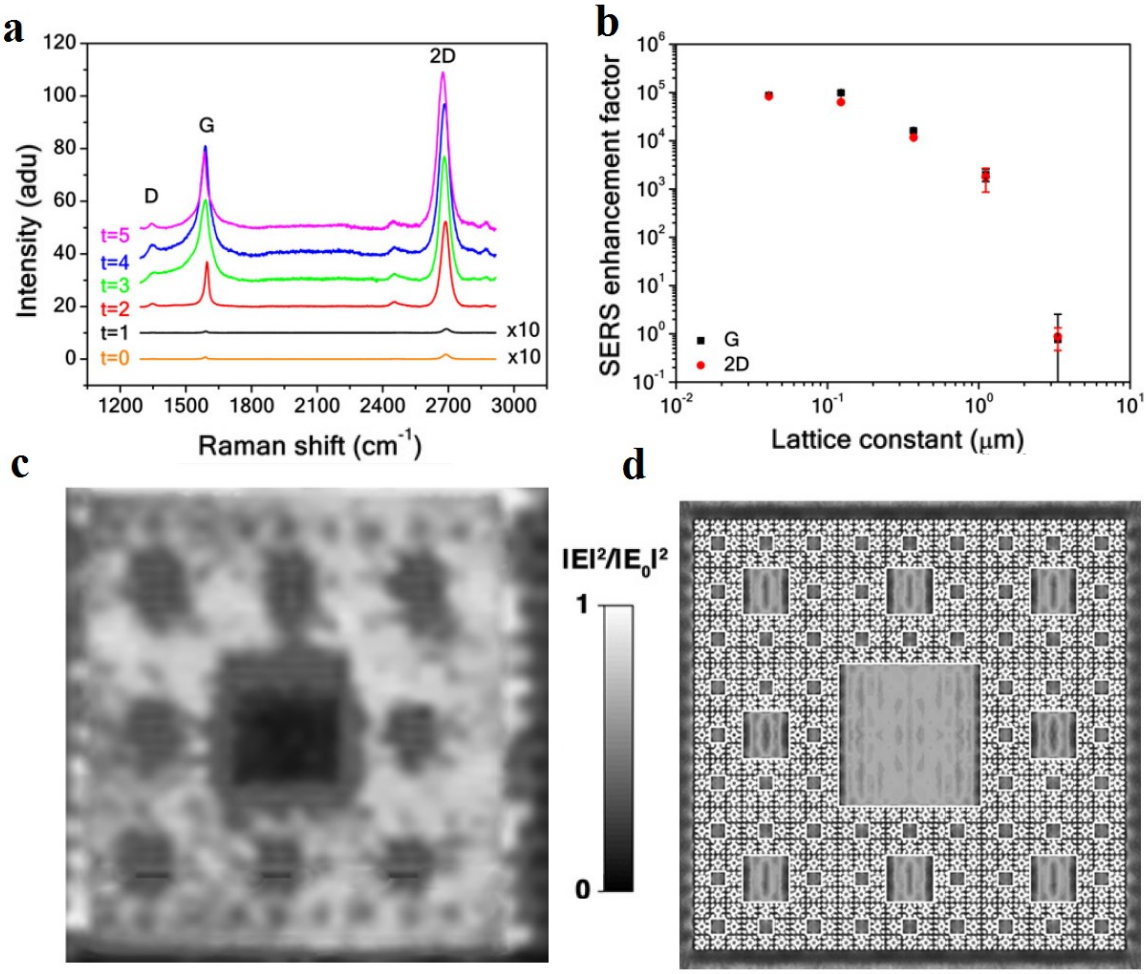

Fig 4.19: a) Average Raman spectra of Au/G fractals for t = 1 - 5 orders and for a reference unpatterned graphene (t = 0) recorded at λ_{ex} = 514 nm. Curves are offset by 10. **b)** SERS enhancement of the graphene G and 2D bands at λ_{ex} = 514 nm as a function of the SC lattice constant a_t in log-log scale. Experimental electric-field enhancement $|\boldsymbol{E}|^2/|\boldsymbol{E_0}|^2$ maps of the BCB vibrational band ω*=1655 cm^{-1} at λ_{ex} = 514 nm for t = 5 **(c)** and its electromagnetic simulation **(d)**. Each map is normalized to its maximum value.

Figure 4.19a shows average Raman spectra of Au/G fractals for t = 1 - 5 orders on a Si/SiO_2 substrate at an excitation wavelength λ_{ex} = 514 nm with a bare graphene as reference (t = 0). Prominent G and 2D bands, characteristic of graphene Raman spectra, are observed at 1584-1589 cm^{-1} and 2674-2689 cm^{-1} respectively, along with a small D peak at 1343-1349 cm^{-1}. As explained in detail (section 4.1.1), the G band corresponds to Brillouin zone-center optical E_{2g} phonon in graphene, D band is due to the breathing modes of six atom rings and requires defect for activation, and 2D band is the second order of D band which originate from a double resonance process that does not need a defect. The presence of weak D peak indicates quality of graphene is deteriorated to a certain degree, and this could be attributed to adatom-induced defects by gold.[159] Also, the broadening of the G band is negligible; suggesting phonon symmetry near the K-point is not broken. Note that the D band intensity was significantly stronger in the case of graphene nanoribbons (section 4.1.1) along with a broadened G band, which arise due to rigorous fabrication methods involving direct etching of graphene introducing edge defects. From this, it is evident that the Au/G plasmonic structures offer a distinct advantage of preserving the quality of graphene over direct patterning.

It can be inferred from Fig 4.19a that the enhancement of the Raman signal at higher orders is much stronger than that of the reference graphene, which predicts the presence of hot spots. When a LSP mode is excited through the Au fractal, a considerable field enhancement not only near the squares but also across the graphene layer occurs. The SERS enhancement factor for G and 2D band is quantitatively shown in Fig 4.19b as a function of the lattice constant a_t of the Au SCs at λ_{ex} = 514 nm. Enhancement is found to

be larger for smaller squares, achieving an enhancement factor up to 10^5 for the smallest square (L_5).

By depositing a thin layer of Brilliant Cresyl Blue (BCB) dye as a probe on t = 5 Au/G SC, the SERS enhancement all over the fractal surface is mapped (Fig 4.19c). The contour plot presents a maximum of contrast in between the squares with size L_4 and L_5 and is in excellent agreement with the electromagnetic simulation illustrated in Fig 4.19d. As the dye is not resonant at the probed excitation wavelength (see section 4.2.3), the observed signal is due purely to a surface-enhanced electromagnetic effect.

4.3.4 Au/G photodetector

Au/G photodetectors are realized by fabricating Au SC at t = 5 order on graphene. This scheme employs metal-graphene-metal configuration as a building block, combined with Au SC to enhance light absorption in graphene. The optical image and scheme are shown in Figure 4.20 while the experimental setup employed for characterization is outlined in Fig 3.9.

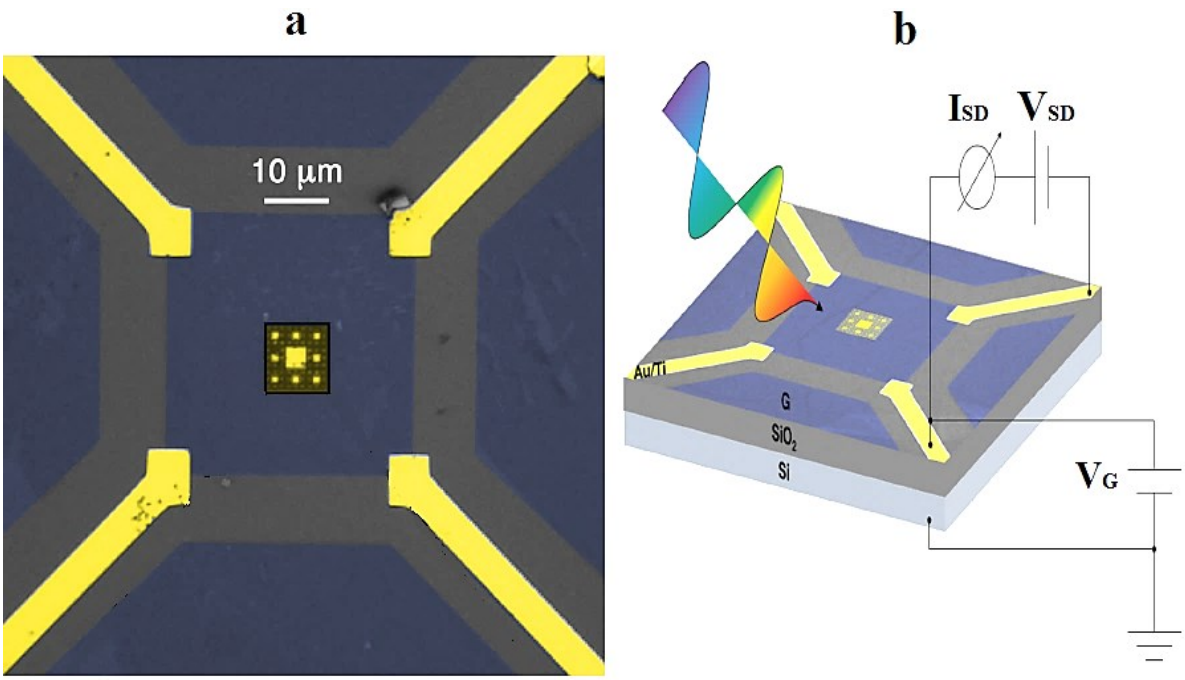

Fig 4.20: a) Optical image of a 35±3 nm thick Au SC for t = 5 (yellow) on SLG (blue) transferred on a Si/SiO_2 substrate (gray). Four leads of the photodetector are also shown (yellow). **b)** Scheme of the device.

Figures 4.21a-d present characterization of Au/G fractal photodetector for different incident photon energies and power densities. All the measurements are carried out at room temperature and in vacuum (10^{-6} mbar) and V_{SD} is set to 0.1 V. The photocurrent, i.e., the difference between the current measured under illumination and the dark current at five different incident laser energies (0.8 eV, 1.46 eV, 1.94 eV and 2.38 eV) as a function of

relative gate voltage to the CNP at a fixed incident power density 10 mW cm^{-2} is shown in Fig 4.21a. It is observed that a photocurrent is generated for all laser energies, confirming a functioning photodiode in the VIS-NIR regime. The photocurrent follows typical shape observed in graphene field-effect devices, with a minimum at $V_G = V_{CNP}$, due to charge neutrality which is translated as minimum photocurrent when the relative gate voltage is zero. At larger gate voltages close to -80 V, an increased photocurrent is observed at all the incident laser energies, ~ 100 times more compared to that at zero relative gate voltage. Fig 4.21b represents photocurrent as a function of V_G - V_{CNP} at 1.94 eV illumination energy for different laser powers. Here we considered the power impinging on the device area, i.e., the total area of graphene channel which is 40 x 40 μm. The influence of power is more pronounced at larger negative gate voltages, exhibiting up to 10 times enhancement when the power is varied from 1 mW cm^{-2} to 75 mW cm^{-2} at -80 V relative gate voltage shift. From Fig 4.21a,b it is obvious that the photocurrent can be efficiently controlled by changing the back gate voltage.

The dependence of photocurrent on incident power is further investigated and reported in Fig 4.21c. Here the photocurrent is recorded at 1.46, 1.94, and 2.38 eV laser energies (849 nm, 639 nm and 521 nm respectively) at a fixed gate voltage -50V, by varying incident power density from 0 up to 130 mW cm^{-2}. Photocurrent shows a large linear increment up to ~ 20 mW cm^{-2} with power density and a further increase shows a reduced slope, indicating a saturation effect. This could be due to electrostatic and thermal effects, trapping and re-combination occurring at high values of power.[69,313,314]

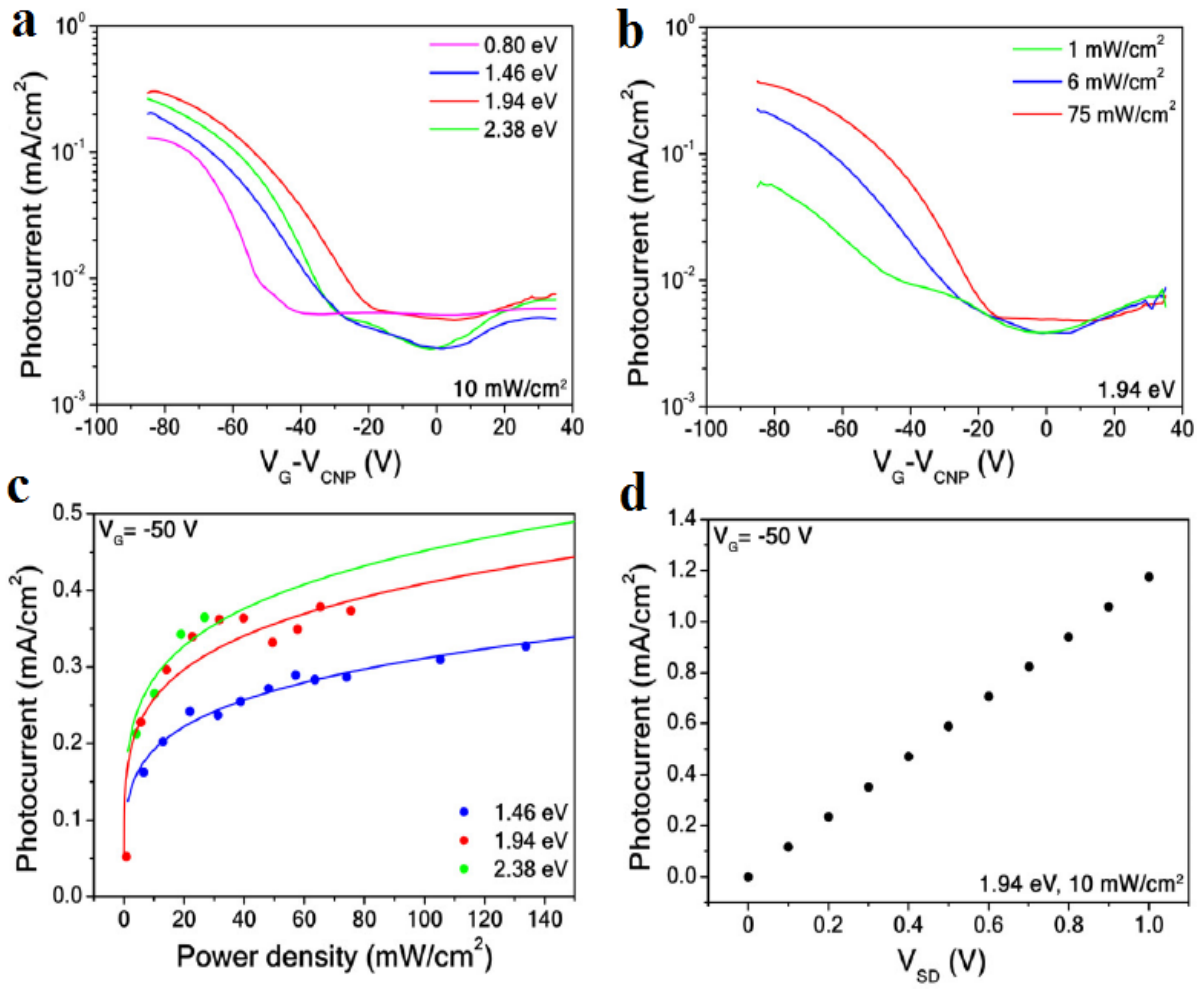

Fig 4.21: AC photocurrent density as a function of the relative gate voltage to the CNP for different incident laser energies at 10 mW cm^{-2} **(a)** and for different incident powers of a 1.94 eV laser **(b)**. **c)** AC photocurrent at V_G = -50 V as a function of power for different laser energies. Solid lines show power law fits. **d)** AC photocurrent at V_G = -50 V as a function of the V_{SD} for a 1.94 eV laser at 10 mW cm^{-2} incident power.

The photocurrent as a function of V_{SD} under 1.94 eV laser frequency and 10 mW cm^{-2} power at -50V gate voltage is shown in Fig 4.21d, indicating linear increase of photocurrent with V_{SD}.

Fig 4.22 summarizes figures of merit of our Au/G fractal array photodetectors (See section 2.4.2 for definitions and equations). We ensured to work in linear region in Fig 4.21c to avoid any overheating in the sample. Therefore the power density was fixed at 10 mW cm^{-2}

for all the measurements presented here. In Fig 4.22a, the broadband and electrically tunable responsivity $R = I_{ph}/P_{in}$ of a 3 x 3 array of t = 5 Au/G SC is shown as a function of the applied gate voltage. The device total absorption A = 1 - R, and the external ($EQE = R\hbar\omega/e$) and internal ($IQE = EQE/A$) quantum efficiencies are evaluated in Fig 4.22b. It is worth noting that in the spectral range investigated, the Au/G SC photodetector IQE is up to 100% in correspondence of the ω_5 LSP resonance. An enhancement factor of up to 10 is presented in Figure 4.22c for the Au/G SC device over an unpatterned graphene device.

The efficiency measurements can be affected by noise signals, such as thermal noise and shot noise.[313,315] Therefore a proper assessment of the PD performance is not just provided by the responsivity, but also by measuring the noise-equivalent-power (NEP). NEP quantifies sensitivity of a photodetector by expressing the weakest optical signal that can be detected and it is defined as the input signal power that results in a signal-to-noise ratio (SNR) of unity.[316] NEP is calculated from responsivity R as [223,302,317,318]: $NEP = S_i/R\ [W.Hz^{-1/2}]$, where S_i is the noise current spectral density measured with 0.5 s integration time. Usually, the noise level of photodetectors in current-operating mode is limited by the thermal Johnson-Nyquist contribution which is given by[313,319] $\sqrt{4k_BT/R_d}$ which can be directly extracted from the measured conductivity. Here R_d and T represent dark resistance of the device and the absolute temperature respectively. Frequency-dependent NEP at a bias voltage 0.1 V and V_G = -50 V is presented in Fig 4.22d. NEP exhibits a minimum value of 2×10^{-14} W Hz $^{-1/2}$ at 2.38 eV photon energy, which is compatible with state-of-the-art two-dimensional photodetectors.[320]

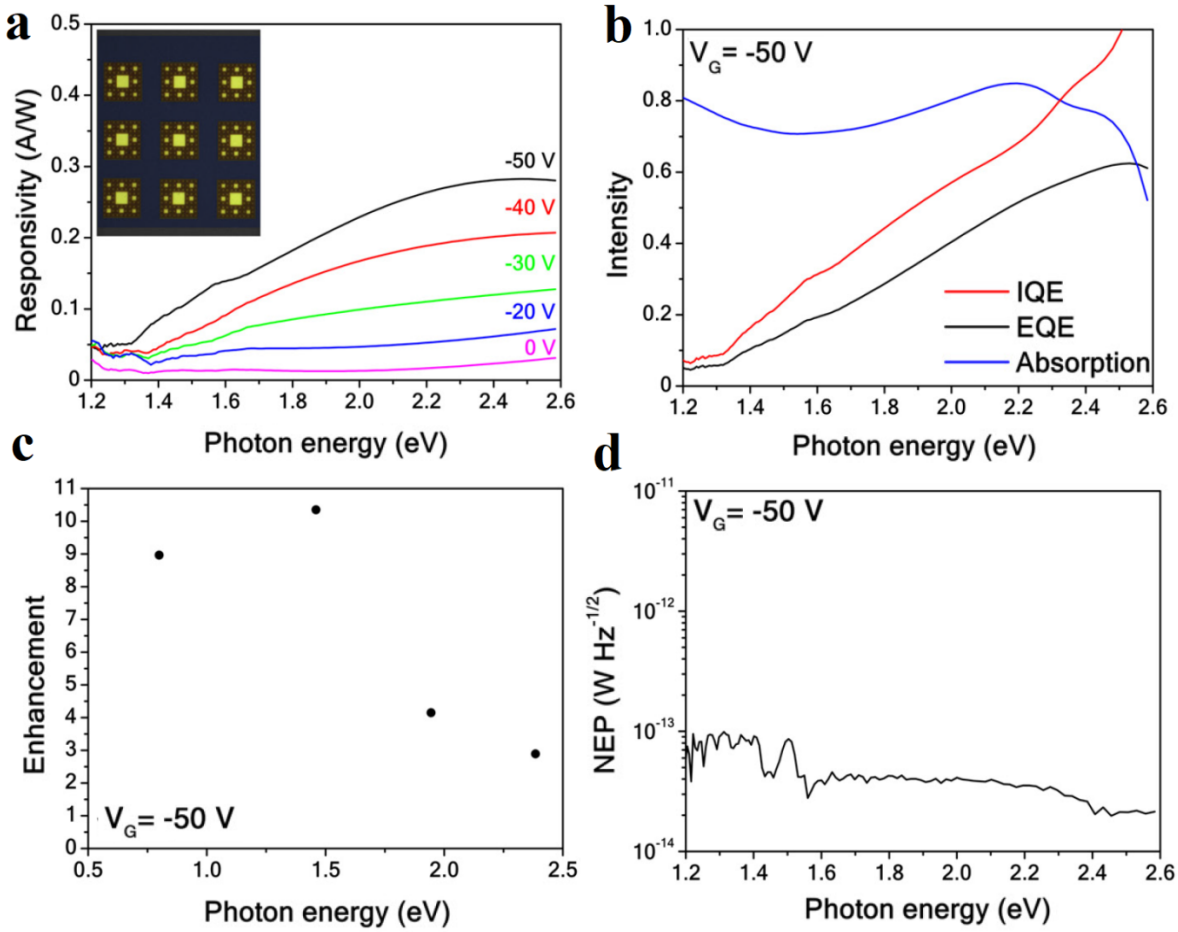

Fig 4.22: a) Responsivity as a function of photon energy for different gate voltages. Inset shows a false color optical microscopy micrograph of the 3x3 array device. **b)** Internal and external quantum efficiencies at V_G = -50 V. **c)** Responsivity enhancement factor with respect to a bare graphene photodetector (t = 0) at V_G = -50 V. **e)** NEP as a function photon energy at V_G = -50 V.

To summarize, we realized a novel, highly sensitive graphene based PD with a broadband optical response employing Au SC fractals. Further, plasmonic SCs are insensitive to the linear and diagonal polarization of the incident light, having a centrosymmetric geometry as shown in section 4.2.1. These provide a distinct advantage in our devices compared to the previously proposed plasmonic enhancement methods in graphene, which are mostly narrowband and polarization dependent.[164,165,221,222] Our device exhibits an enhancement up to an order of magnitude over bare graphene PD, which is comparable to the reported

enhancement factor 8-13 for a graphene PD with Au snowflake fractal.[69] The enhanced photocurrent generation in our Au/G plasmonic PD could be attributed to the increased absorption of incident light due to strong electric-field enhancements provided by the plasmonic fractal. The Au SC positioned on graphene at their LSPR leads to generation of hot carriers[321], which possess an excess energy compared to the Fermi energy of the system. As a consequence, a photovoltage is generated by PTE effect. This mechanism may have been greatly favored by the small electron heat capacity and large light-induced changes in electron temperature in graphene.[217,322,323] Separation of the generated charge carriers requires a junction, which is provided by a difference in work function of metal and graphene (see Fig 4.16c) as well as the applied bias voltage.[221,324] These carriers then produce a photocurrent either by reaching the contacts while still hot or by establishing a local photovoltage within the focal area of laser spot which drives the photocurrent through the rest of the device. We note that the overall photodetection efficiency in graphene based PD can be benefitted from carrier multiplication, which is the conversion of one high-energy electron–hole pair into multiple electron–hole pairs of lower energy due to electron-electron scattering.[320,325]

Although much progress has been made recently, graphene based PD is in its infancy and faces many challenges in fundamental and practical aspects. As outlined in section 2.4.2, physical mechanisms of photoresponse in graphene PD could be attributed to several phenomenon, which are still debated and yet to be investigated thoroughly. In our devices, further studies such as scanning photocurrent confocal microscopy might be able to provide better insight into the photocurrent generation. Further, it is worth noting that the properties

of metal/graphene interfaces require more attention as the contact doping involves not only the electron transfer between materials with different work functions, but also the metal-graphene chemical interaction.[269] As future direction, we propose top-gating schemes to be integrated with graphene PDs for better control of carrier dynamics by applying smaller gate voltages which has been recently reported using ionic liquid electrolyte in graphene-fractal metasurface device.[326] We also note that better device performance, particularly high speed operation[327], could be achieved by employing hBN as a substrate instead SiO_2 as it offers superior carrier mobility in graphene.[328]

Chapter 5: Conclusions

We systematically investigated electrical and plasmonic properties of graphene, gold, and hybrid nanostructures. To this end, we fabricated graphene nanoribbons and gold nanostructures inspired by the Sierpinski carpet fractal on both graphene and on Si/SiO_2. Electrical and optical characterizations along with electromagnetic simulations were performed demonstrating their uniquely tunable plasmonic response.

Exploration of GNR devices served as a benchmark in developing methodologies for the state-of-the-art EBL and characterization techniques that were applied to more complex structures afterwards. GNR arrays with ribbon width ~ 150 nm were fabricated. Raman studies indicated strong D band, attributed to the edges. GNR based FETs were implemented, demonstrating the possibility to control the current flow through such devices by changing the gate voltage. Optical studies on GNR arrays revealed multiple peaks in the MIR regime, attributed to the interaction of graphene plasmons with surface optical phonons accommodated by SiO_2 substrate, as well as the graphene intrinsic optical phonon mode. Experimental observations were supported by COMSOL simulations, visualizing enhanced field intensities in individual ribbon edges.

For the realization of devices with multiband spectral response, Au SC deterministic fractals were fabricated. FTIR revealed a broadband spectral response showing the possibility to support multiple resonances. Through systematic study of such multi-resonant modes spanning from VIS to MIR range, we demonstrated that they are originating from diffraction-mediated LSPs. Simple calculations by finite element method electromagnetic

simulations has also demonstrated large values of electric near-field enhancements in progressively smaller length scales of the fractal elements. Furthermore, SERS was employed to experimentally verify these results. The electric near-field enhancement was visualized on Brilliant Cresyl Blue molecules using the 5th order SC, providing a maximum electric-field enhancement factor of ~ 10 in the resonant case while ~ 5 in the non-resonant case.

Novel Au/G systems were realized yielding enhanced light-graphene interactions, thanks to the higher field localization provided by Au plasmonic SC. A multimodal spectral response from the VIS to MIR range similar to that of SC without graphene was observed, but with an advantage of controlling such resonances through electrical gating of graphene. Strong SERS enhancement was observed for the G and 2D vibrational band intensities with increasing order of fractal, reaching a SERS enhancement factor up to 10^5. Also the experimental electric-field enhancement map corresponding to the BCB vibrational band showed good agreement with the spatial distribution of the electric near-field enhancement obtained by electromagnetic simulations. Finally, Au/G photodetectors were realized to exploit increased absorption of incident light due to strong electric-field enhancements provided by Au plasmonic SCs. A broadband photoresponse was observed in the VIS-NIR range and an enhancement factor about 10 over a bare graphene photodetector was achieved.

Publications

- De Nicola, F., Puthiya Purayil, N.S., Spirito, D., Miscuglio, M., Tantussi, F., Tomadin, A., De Angelis, F., Polini, M., Krahne, R. and Pellegrini, V., 2018. **Multiband plasmonic Sierpinski carpet fractal antennas**, **ACS Photonics**. DOI: 10.1021/acsphotonics.8b00186.
- **Graphene plasmonic fractal photodetectors** (In preparation June 2018).

Conference presentations and contributions

- **N. Puthiya Purayil**, D. Spirito, and V. Pellegrini, **Electrical and plasmonic studies of lithographically patterned graphene nanoribbons**, International Conference on Nanosciences and Nanotechnologies (NN), Thessaloniki, Greece, 2016 (Poster).
- **N. Puthiya**, M. Miscuglio, F. De Nicola, D. Spirito, A. Tomadin, F. Tantussi, F. De Angelis, M. Polini, R. Krahne, and V. Pellegrini, **Fabrication and characterization of plasmonic gold Sierpinski Nanocarpets,** Nanophotonics and Micro/Nano Optics International Conference (NANOP), Barcelona, Spain, 2017 (Poster).

- **De Nicola**, **F.,** Puthiya Purayil, N.S., Spirito, D., Miscuglio, M., Tantussi, F., Tomadin, A., De Angelis, F., Polini, M., Krahne, R. and Pellegrini, V., **Plasmonics in Fractal Dimensions**, MRS fall meeting and exhibit, Boston, Massachusetts, 2017 (Oral presentation).
- **F. De Nicola**, V. Mišeikis, N. Puthiya Purayil, D. Spirito, A. Tomadin, C. Coletti, M. Polini, R. Krahne, and V. Pellegrini, **Fractal plasmonics in graphene**, Graphene week, Athens, Greece, 2017 (Poster).

References

1. Bhushan, B. Handbook of Nanotechnology. in *Handbook of Nanotechnology* 278 (2010). doi:10.1007/3-540-29838-X

2. Maier, S. A. *Plasmonics: fundamentals and applications*. (Springer Science & Business Media, 2007).

3. Novoselov, K. S. *et al.* Electric field effect in atomically thin carbon films. *Science* **306,** 666–9 (2004).

4. Geim, A. K. & Novoselov, K. S. The rise of graphene. *Nat. Mater.* **6,** 183–191 (2007).

5. Geim, A. K. Graphene: status and prospects. *Science* **324,** 1530–4 (2009).

6. Koppens, F. H. L., Chang, D. E. & García De Abajo, F. J. Graphene plasmonics: A platform for strong light-matter interactions. *Nano Lett.* **11,** 3370–3377 (2011).

7. Grigorenko, A. N., Polini, M. & Novoselov, K. S. Graphene plasmonics. *Nat. Photonics* **6,** 749–758 (2012).

8. Luo, X., Qiu, T., Lu, W. & Ni, Z. Plasmons in graphene: Recent progress and applications. *Mater. Sci. Eng. R Reports* **74,** 351–376 (2013).

9. BARBER, D. J. & FREESTONE, I. C. AN INVESTIGATION OF THE ORIGIN OF THE COLOUR OF THE LYCURGUS CUP BY ANALYTICAL TRANSMISSION ELECTRON MICROSCOPY. *Archaeometry* **32,** 33–45 (1990).

10. Polvorinos del Rio, A., Roehrs, S., Aucouturier, M., Castaing, J. & Bouquillon, A. MEDINA AL-ZAHRA LUSTRE CERAMICS: 10 (th) CENTURY LOCAL NANOTECHNOLOGY OR IMPORTATION FROM MIDDLE EAST. *Arab. J. Sci. Eng.* **35,** 157–168 (2010).

11. Padovani, S. *et al.* Copper in glazes of Renaissance luster pottery: Nanoparticles, ions, and local environment. *J. Appl. Phys.* **93,** 10058–10063 (2003).

12. Brill, R. The chemistry of the Lycurgus Cup. (1965).

13. Freestone, I., Meeks, N., Sax, M. & Higgitt, C. The Lycurgus Cup — A Roman nanotechnology. *Gold Bull.* **40,** 270–277 (2007).

14. Doria, G. *et al.* Noble Metal Nanoparticles for Biosensing Applications. *Sensors* **12,**

1657–1687 (2012).

15. Li, Y., Schluesener, H. J. & Xu, S. Gold nanoparticle-based biosensors. *Gold Bull.* **43,** 29–41 (2010).

16. Kneipp, K., Wang, Y., Kneipp, H., Perelman, L. T. & Itzkan, I. Single molecule detection using surface-enhanced Raman scattering (SERS). *Phys. Rev. ...* **78,** 1667–1670 (1997).

17. Atwater, H. A. & Polman, A. Plasmonics for improved photovoltaic devices. *Nat. Mater.* **9,** 205–213 (2010).

18. Ditlbacher, H., Krenn, J. R., Lamprecht, B., Leitner, A. & Aussenegg, F. R. Spectrally coded optical data storage by metal nanoparticles. *Opt. Lett.* **25,** 563 (2000).

19. Zheludev, N. I. A Roadmap for Metamaterials. *Opt. Photonics News* **22,** 30 (2011).

20. Noguez, C. & Rom??n-Vel??zquez, C. E. Dispersive force between dissimilar materials: Geometrical effects. *Phys. Rev. B - Condens. Matter Mater. Phys.* **70,** 1–8 (2004).

21. Blaber, M. G., Arnold, M. D. & Ford, M. J. Search for the Ideal Plasmonic Nanoshell: The Effects of Surface Scattering and Alternatives to Gold and Silver. *J. Phys. Chem. C* **113,** 3041–3045 (2009).

22. KOC, S. KITTEL, C-INTRODUCTION TO SOLID STATE PHYSICS. (1967).

23. Willets, K., Chem., R. V. D.-A. R. P. & 2007, undefined. Localized surface plasmon resonance spectroscopy and sensing. *annualreviews.org*

24. Chou, C.-H. & Chen, F.-C. Plasmonic nanostructures for light trapping in organic photovoltaic devices. *Nanoscale* **6,** 8444 (2014).

25. Barnes, W. L., Dereux, A. & Ebbesen, T. W. Surface plasmon subwavelength optics. *Nature* **424,** 824–830 (2003).

26. Otto, A. Excitation of non radiative surface plasma waves in silver by the method of frustrated total reflection. *Z. Physik* **216,** 398–410 (1968).

27. Kretschmann, E. & Raether, H. Radiative Decay of Non Radiative Surface Plasmons Excited by Light. *Zeitschrift fur Naturforschung - Section A Journal of Physical Sciences* **23,** 2135–2136 (1968).

28. Sambles, J. R., Bradbery, G. W. & Yang, F. Optical excitation of surface plasmons: An introduction. *Contemp. Phys.* **32,** 173–183 (1991).

29. Vigderman, L., Khanal, B. P. & Zubarev, E. R. Functional gold nanorods: Synthesis, self-assembly, and sensing applications. *Advanced Materials* **24,** 4811–4841 (2012).

30. Rycenga, M. *et al.* Controlling the synthesis and assembly of silver nanostructures for plasmonic applications. *Chemical Reviews* **111,** 3669–3712 (2011).

31. Chen, H., Shao, L., Li, Q. & Wang, J. Gold nanorods and their plasmonic properties. *Chem. Soc. Rev.* **42,** 2679–2724 (2013).

32. Li, X., Zhu, J. & Wei, B. Hybrid nanostructures of metal/two-dimensional nanomaterials for plasmon-enhanced applications. *Chem. Soc. Rev.* **45,** 3145–3187 (2016).

33. Jiang, R., Li, B., Fang, C. & Wang, J. Metal/Semiconductor Hybrid Nanostructures for Plasmon-Enhanced Applications. *Adv. Mater.* **26,** 5274–5309 (2014).

34. Link, S. & El-Sayed, M. A. Size and Temperature Dependence of the Plasmon Absorption of Colloidal Gold Nanoparticles. *J. Phys. Chem. B* **103,** 4212–4217 (1999).

35. McFarland, A. D. & Van Duyne, R. P. Single silver nanoparticles as real-time optical sensors with zeptomole sensitivity. *Nano Lett.* **3,** 1057–1062 (2003).

36. Van Der Zande, B. M. I., Böhmer, M. R., Fokkink, L. G. J. & Schönenberger, C. Colloidal dispersions of gold rods: Synthesis and optical properties. *Langmuir* **16,** 451–458 (2000).

37. Link, S. & El-Sayed, M. A. Shape and size dependence of radiative, non-radiative and photothermal properties of gold nanocrystals. *Int. Rev. Phys. Chem.* **19,** 409–453 (2000).

38. Yang, W. H., Schatz, G. C. & Van Duyne, R. P. Discrete dipole approximation for calculating extinction and Raman intensities for small particles with arbitrary shapes. *J. Chem. Phys.* **103,** 869–875 (1995).

39. Kreibig, U. & Vollmer, M. Optical Properties of Metal Clusters. *J. Am. Chem. Soc.* **118,** 6098–6098 (1995).

40. Link, S., Wang, Z. L. & El-Sayed, M. A. Alloy Formation of Gold−Silver Nanoparticles and the Dependence of the Plasmon Absorption on Their

Composition. *J. Phys. Chem. B* **103,** 3529–3533 (1999).

41. Lindquist, N. C., Nagpal, P., McPeak, K. M., Norris, D. J. & Oh, S. H. Engineering metallic nanostructures for plasmonics and nanophotonics. *Reports on Progress in Physics* **75,** (2012).

42. Mallin, M. P. & Murphy, C. J. Solution-Phase Synthesis of Sub-10 nm Au-Ag Alloy Nanoparticles. *Nano Lett.* **2,** 1235–1237 (2002).

43. Liz-Marzán, L. M. Tailoring surface plasmons through the morphology and assembly of metal nanoparticles. *Langmuir* **22,** 32–41 (2006).

44. Werner, D. H. & Ganguly, S. An overview of fractal antenna engineering research. *IEEE Antennas Propag. Mag.* **45,** 38–57 (2003).

45. Miyamaru, F. *et al.* Terahertz electric response of fractal metamaterial structures. *Phys. Rev. B - Condens. Matter Mater. Phys.* **77,** 1–6 (2008).

46. Maraghechi, P. & Elezzabi, A. Y. Enhanced THz radiation emission from plasmonic complementary Sierpinski fractal emitters. *Opt. Express* **18,** 27336 (2010).

47. Agrawal, A., Matsui, T., Zhu, W., Nahata, A. & Vardeny, Z. V. Terahertz spectroscopy of plasmonic fractals. *Phys. Rev. Lett.* **102,** (2009).

48. Mahler, L. *et al.* Quasi-periodic distributed feedback laser. *Nat. Photonics* **4,** 165–169 (2010).

49. Wen, W., Zhou, L., Hou, B., Chan, C. T. & Sheng, P. Resonant transmission of microwaves through subwavelength fractal slits in a metallic plate. *Phys. Rev. B - Condens. Matter Mater. Phys.* **72,** 2–5 (2005).

50. Hou, B., Liao, X. Q. & Poon, J. K. S. Resonant infrared transmission and effective medium response of subwavelength H-fractal apertures. *Opt. Express* **18,** 3946–3951 (2010).

51. Dal Negro, L. & Boriskina, S. V. Deterministic aperiodic nanostructures for photonics and plasmonics applications. *Laser Photonics Rev.* **6,** 178–218 (2012).

52. Aouani, H. *et al.* Plasmonic nanoantennas for multispectral surface-enhanced spectroscopies. *J. Phys. Chem. C* **117,** 18620–18626 (2013).

53. Mandelbrot, B. B. *The Fractal Geometry of Nature*. *American Journal of Physics* **51,** (1983).

54. Falconer, K. Fractal Geometry: Mathematical Foundations and Applications. *John Wiley and Sons* **46,** 886 (1990).

55. Hausdorff, F. Dimension und äußeres Maß. *Math. Ann.* **79,** 157–179 (1918).

56. Schleicher, D. Hausdorff dimension, its properties, and its surprises. *Am. Math. Mon.* **114,** 509–528 (2007).

57. Von Koch, H. On a continuous curve without tangents constructible from elementary geometry. *Class. Fractals (Westview Press. 2004) pp* **25,** 45 (1993).

58. Sharma, V. Deterministic chaos and fractal complexity in the dynamics of cardiovascular behavior: perspectives on a new frontier. *Open Cardiovasc. Med. J.* **3,** 110–123 (2009).

59. Jiang, S. & Liu, D. Box-Counting Dimension of Fractal Urban Form. *Int. J. Artif. Life Res.* **3,** 41–63 (2012).

60. Vicsek, T. *Fractal growth phenomena*. (World Scientific, 1989).

61. Sierpinski, W. Sur une courbe cantorienne qui contient une image biunivoque et continue de toute courbe donnée. *CR Acad. Sci. Paris* **162,** 629–632 (1916).

62. Golestanirad, L., Pollo, C. & Graham, S. J. Analysis of fractal electrodes for efficient neural stimulation. in *Proceedings of the Annual International Conference of the IEEE Engineering in Medicine and Biology Society, EMBS* 791–794 (2013). doi:10.1109/EMBC.2013.6609619

63. Prusinkiewicz, P. & Lindenmayer, A. *The algorithmic beauty of plants*. (Springer Science & Business Media, 1990).

64. Zhu, L.-H. *et al.* Broadband absorption and efficiency enhancement of an ultra-thin silicon solar cell with a plasmonic fractal. *Opt. Express* **21,** A313–A323 (2013).

65. Volpe, G., Volpe, G. & Quidant, R. Fractal plasmonics: subdiffraction focusing and broadband spectral response by a Sierpinski nanocarpet. *Opt. Express* **19,** 3612 (2011).

66. Kazerooni, H. & Khavasi, A. Plasmonic fractals: Ultrabroadband light trapping in thin film solar cells by a Sierpinski nanocarpet. *Opt. Quantum Electron.* **46,** 751–757 (2014).

67. Chen, T. L., Dikken, D. J., Prangsma, J. C., Segerink, F. & Herek, J. L. Characterization of Sierpinski carpet optical antenna at visible and near-infrared

wavelengths. *New J. Phys.* **16,** 093024 (2014).

68. Aslan, E. E. *et al.* Multispectral Cesaro-Type Fractal Plasmonic Nanoantennas. *ACS Photonics* **3,** 2102–2111 (2016).

69. Fang, J. *et al.* Enhanced graphene photodetector with fractal metasurface. *Nano Lett.* **17,** 57–62 (2017).

70. Hatab, N. A. *et al.* Free-standing optical gold bowtie nanoantenna with variable gap size for enhanced Raman spectroscopy. *Nano Lett.* **10,** 4952–4955 (2010).

71. Grigorenko, I. Nanostructures with the Hilbert curve geometry as surface enhanced Raman scattering substrates. *Appl. Phys. Lett.* **103,** (2013).

72. Zhou, L., Chan, C. T. & Sheng, P. Theoretical studies on the transmission and reflection properties of metallic planar fractals. *J. Phys. D. Appl. Phys.* **37,** 368–373 (2004).

73. Dong, J. *et al.* Simultaneous SEF and SERRS from silver fractal-like nanostructure. *Sensors Actuators, B Chem.* **191,** 595–599 (2014).

74. Hou, C. *et al.* Ag-nanoparticle-decorated Au-fractal patterns on bowl-like-dimple arrays on Al foil as an effective SERS substrate for the rapid detection of PCBs. *Chem. Commun.* **50,** 569–571 (2014).

75. Tsai, D. P. *et al.* Photon Scanning-Tunneling-Microscopy Images of Optical-Excitations of Fractal Metal Colloid Clusters. *Phys. Rev. Lett.* **72,** 4149–4152 (1994).

76. Stockman, M. I., Shalaev, V. M., Moskovits, M., Botet, R. & George, T. F. Enhanced Raman scattering by fractal clusters: Scale-invariant theory. *Phys. Rev. B* **46,** 2821–2830 (1992).

77. Gottheim, S., Zhang, H., Govorov, A. O. & Halas, N. J. Fractal nanoparticle plasmonics: The Cayley tree. *ACS Nano* **9,** 3284–3292 (2015).

78. Bao, Y. J. *et al.* Surface-plasmon-enhanced transmission through metallic film perforated with fractal-featured aperture array. *Appl. Phys. Lett.* **90,** 1–4 (2007).

79. Ghaemi, H. F., Thio, T., Grupp, D. E., Ebbesen, T. W. & Lezec, H. J. Surface plasmons enhance optical transmission through subwavelength holes. *Phys. Rev. B* **58,** 6779–6782 (1998).

80. Bao, Y. J. *et al.* Tailoring the resonances of surface plasmas on fractal-featured metal film by adjusting aperture configuration. *Appl. Phys. Lett.* **92,** 90–93 (2008).

81. Wallace, P. R. The band theory of graphite. *Phys. Rev.* **71,** 622–634 (1947).

82. Fradkin, E. Critical behavior of disordered degenerate semiconductors. II. Spectrum and transport properties in mean-field theory. *Phys. Rev. B* **33,** 3263–3268 (1986).

83. Mermin, N. D. Crystalline order in two dimensions. *Phys. Rev.* **176,** 250–254 (1968).

84. Novoselov, K. S. *et al.* Two-dimensional gas of massless Dirac fermions in graphene. *Nature* **438,** 197–200 (2005).

85. Castro Neto, A. H. ., Peres, N. M. R. ., Novoselov, K. S. ., Geim, A. K. . & Guinea, F. The electronic properties of graphene. *Rev. Mod. Phys.* **81,** 109–162 (2009).

86. Zhang, Y. B., Tan, Y. W., Stormer, H. L. & Kim, P. Experimental observation of the quantum Hall effect and Berry's phase in graphene. *Nature* **438,** 201–204 (2005).

87. Zheng, Y. & Ando, T. Hall conductivity of a two-dimensional graphite system. *Phys. Rev. B - Condens. Matter Mater. Phys.* **65,** 2454201–24542011 (2002).

88. Novoselov, K. S. *et al.* Two-dimensional atomic crystals. *Proc. Natl. Acad. Sci.* **102,** 10451–10453 (2005).

89. Geim, A. K. & MacDonald, A. H. Graphene: Exploring carbon flatland. *Phys. Today* **60,** 35–41 (2007).

90. Lee, C., Wei, X., Kysar, J. W. & Hone, J. Measurement of the Elastic Properties and Intrinsic Strength of Monolayer Graphene. *Science (80-.).* **321,** 385–388 (2008).

91. Bryan, S. E. Structural and electrical properties of epitaxial graphene nanoribbons. (2013).

92. Bunch, J. S. Mechanical and Electrical Properties of Graphene Sheets. *Chem. ...* 1–140 (2008).

93. Chen, J.-H., Jang, C., Xiao, S., Ishigami, M. & Fuhrer, M. S. Intrinsic and extrinsic performance limits of graphene devices on SiO2. *Nat. Nanotechnol.* **3,** 206–209 (2008).

94. Morozov, S. V, Novoselov, K. S. & Geim, A. K. Electron transport in graphene. *Physics-Uspekhi* **51,** 744–748 (2008).

95. Mayorov, A. S. *et al.* Micrometer-scale ballistic transport in encapsulated graphene at room temperature. *Nano Lett.* **11,** 2396–2399 (2011).

96. Pierret, R. F. *Semiconductor device fundamentals*. (Pearson Education India, 1996).

97. Reddy, D., Register, L. F., Carpenter, G. D. & Banerjee, S. K. Graphene field-effect transistors. *J. Phys. D. Appl. Phys.* **45,** 019501 (2012).

98. Chen, Z., Lin, Y. M., Rooks, M. J. & Avouris, P. Graphene nano-ribbon electronics. *Phys. E Low-Dimensional Syst. Nanostructures* **40,** 228–232 (2007).

99. Stauber, T., Peres, N. M. R. & Geim, A. K. The optical conductivity of graphene in the visible region of the spectrum. 1–8 (2008). doi:10.1103/PhysRevB.78.085432

100. Mak, K. F. *et al.* Measurement of the Optical Conductivity of Graphene. *Phys. Rev. Lett.* **101,** 196405 (2008).

101. Wang, X., Zhi, L. & Müllen, K. Transparent, conductive graphene electrodes for dye-sensitized solar cells. *Nano Lett.* **8,** 323–327 (2008).

102. Falkovsky, L. A. Optical properties of graphene. *J. Phys. Conf. Ser.* **129,** (2008).

103. Liu, C., Bai, Y., Zhou, J., Zhao, Q. & Qiao, L. A review of graphene plasmons and its combination with metasurface. *Journal of the Korean Ceramic Society* **54,** 349–365 (2017).

104. Jain, P. K., Huang, X., El-Sayed, I. H. & El-Sayed, M. A. Review of some interesting surface plasmon resonance-enhanced properties of noble metal nanoparticles and their applications to biosystems. *Plasmonics* **2,** 107–118 (2007).

105. Park, M. T. Graphene Plasmonics: Challenges and Opportunities. **24,** (2014).

106. Li, Z. Q. *et al.* Dirac charge dynamics in graphene by infrared spectroscopy. *Nat. Phys.* **4,** 532–535 (2008).

107. Wang, F. *et al.* Gate-Variable Optical Transitions in Graphene. *Science (80-.).* **320,** 206–209 (2008).

108. Emani, N. K. *et al.* Electrically Tunable Plasmonic Resonances with Graphene. *Nano Lett.* JTu1M.2 (2012). doi:10.1364/CLEO_AT.2012.JTu1M.2

109. Hwang, E. H. & Das Sarma, S. Dielectric function, screening, and plasmons in two-dimensional graphene. *Phys. Rev. B - Condens. Matter Mater. Phys.* **75,** 1–6 (2007).

110. Abedinpour, S. H. *et al.* Drude weight, plasmon dispersion, and ac conductivity in doped graphene sheets. *Phys. Rev. B - Condens. Matter Mater. Phys.* **84,** 1–14 (2011).

111. Wunsch, B., Stauber, T., Sols, F. & Guinea, F. Dynamical polarization of graphene at finite doping. *New J. Phys.* **8,** (2006).

112. Mermin, N. D. Lindhard dielectric function in the relaxation-time approximation. *Phys. Rev. B* **1,** 2362–2363 (1970).

113. Rana, F. Graphene Terahertz Plasmon Oscillators. *IEEE Trans. Nanotechnol.* **7,** 91–99 (2008).

114. Chen, C. F. *et al.* Controlling inelastic light scattering quantum pathways in graphene. *Nature* **471,** 617–620 (2011).

115. Garciía De Abajo, F. J. Multiple excitation of confined graphene plasmons by single free electrons. *ACS Nano* **7,** 11409–11419 (2013).

116. Ju, L. *et al.* Graphene plasmonics for tunable terahertz metamaterials. *Nat. Nanotechnol.* **6,** 630–634 (2011).

117. Christensen, J., Manjavacas, A., Thongrattanasiri, S., Koppens, F. H. L. & García De Abajo, F. J. Graphene plasmon waveguiding and hybridization in individual and paired nanoribbons. *ACS Nano* **6,** 431–440 (2012).

118. Yan, H. *et al.* Damping pathways of mid-infrared plasmons in graphene nanostructures. *Nat. Photonics* **7,** 394–399 (2013).

119. Yan, H. *et al.* Tunable infrared plasmonic devices using graphene/insulator stacks. *Nat. Nanotechnol.* **7,** 330–334 (2012).

120. Thongrattanasiri, S., Koppens, F. H. L. & Garc??a De Abajo, F. J. Complete optical absorption in periodically patterned graphene. *Phys. Rev. Lett.* **108,** (2012).

121. Chen, J. *et al.* Optical nano-imaging of gate-tunable graphene plasmons. *Nature* **487,** 77–81 (2012).

122. Fei, Z. *et al.* Gate-tuning of graphene plasmons revealed by infrared nano-imaging. *Nature* **486,** 82–85 (2012).

123. Mikhailov, S. A. & Savostianova, N. A. Influence of contacts on the microwave response of a two-dimensional electron stripe. *Phys. Rev. B - Condens. Matter Mater. Phys.* **74,** (2006).

124. Fuchs, R. & Kliewer, K. L. Optical modes of vibration in an ionic crystal slab. *Phys. Rev.* **140,** (1965).

125. Hwang, E. H., Sensarma, R., Das Sarma, S. & Sarma, S. Das. Plasmon-phonon coupling in graphene. *Phys. Rev. B* **82,** 1–5 (2010).

126. Fratini, S. & Guinea, F. Substrate-limited electron dynamics in graphene. *Phys. Rev. B - Condens. Matter Mater. Phys.* **77,** (2008).

127. Han, M. Y., Ozyilmaz, B., Zhang, Y. & Kim, P. Energy band-gap engineering of graphene nanoribbons. *Phys. Rev. Lett.* **98,** 1–4 (2007).

128. Todd, K., Chou, H. T., Amasha, S. & David, G. G. Quantum dot behavior in graphene nanoconstrictions. *Nano Lett.* **9,** 416–421 (2009).

129. Radovic, L. R. & Bockrath, B. On the chemical nature of graphene edges: Origin of stability and potential for magnetism in carbon materials. *J. Am. Chem. Soc.* **127,** 5917–5927 (2005).

130. Ferrari, A. C. *et al.* Science and technology roadmap for graphene, related two-dimensional crystals, and hybrid systems. *Nanoscale* **7,** 4598–4810 (2015).

131. Raccichini, R., Varzi, A., Passerini, S. & Scrosati, B. The role of graphene for electrochemical energy storage. *Nat. Mater.* **14,** 271 (2015).

132. Del Rio Castillo, A. E. *et al.* High yield production of 2D crystals by wet-jet milling. *Submitted...* 1–17 (2017). doi:10.1039/x0xx00000x

133. Novoselov, K. S. Nobel Lecture: Graphene: Materials in the Flatland. *Rev. Mod. Phys.* **83,** 837–849 (2011).

134. Roddaro, S., Pingue, P., Piazza, V., Pellegrini, V. & Beltram, F. The optical visibility of graphene: Interference colors of ultrathin graphite on SiO2. *Nano Lett.* **7,** 2707–2710 (2007).

135. Cooper, D. R. *et al.* Experimental review of graphene. **2012,** (2011).

136. Li, X. *et al.* Large-Area Synthesis of High-Quality and Uniform Graphene Films on Copper Foils. *Science (80-.).* **324,** 1312–1314 (2009).

137. Kim, K. S. K. S. *et al.* Large-scale pattern growth of graphene films for stretchable transparent electrodes. *Nature* **457,** 706–710 (2009).

138. Miao, C., Zheng, C., Liang, O. & Xie, Y.-H. Chemical vapor deposition of graphene. in *Physics and applications of graphene-experiments* (InTech, 2011).

139. Liu, W. *et al.* Chemical vapor deposition of large area few layer graphene on Si

catalyzed with nickel films. *Thin Solid Films* **518,** (2010).

140. Obraztsov, A. N., Obraztsova, E. A., Tyurnina, A. V. & Zolotukhin, A. A. Chemical vapor deposition of thin graphite films of nanometer thickness. *Carbon N. Y.* **45,** 2017–2021 (2007).

141. Mattevi, C., Kim, H. & Chhowalla, M. A review of chemical vapour deposition of graphene on copper. *J. Mater. Chem.* **21,** 3324–3334 (2011).

142. Li, X. *et al.* Graphene films with large domain size by a two-step chemical vapor deposition process. *Nano Lett.* **10,** 4328–4334 (2010).

143. Polat, E. O. *et al.* Synthesis of Large Area Graphene for High Performance in Flexible Optoelectronic Devices. *Sci. Rep.* **5,** (2015).

144. Novoselov, K. S. *et al.* A roadmap for graphene. *Nature* **490,** 192–200 (2012).

145. Forbeaux, I., Themlin, J.-M. & Debever, J.-M. Heteroepitaxial graphite on 6 H− SiC (0001): Interface formation through conduction-band electronic structure. *Phys. Rev. B* **58,** 16396 (1998).

146. Berger, C. Electronic Confinement and Coherence in Patterned Epitaxial Graphene. *Science (80-.).* **312,** 1191–1196 (2006).

147. Hernandez, Y. *et al.* High-yield production of graphene by liquid-phase exfoliation of graphite. *Nat. Nanotechnol.* **3,** 563–568 (2008).

148. Bonaccorso, F. & Sun, Z. Solution processing of graphene, topological insulators and other 2d crystals for ultrafast photonics. *Opt. Mater. Express* **4,** 63 (2014).

149. Lotya, M., King, P. J., Khan, U., De, S. & Coleman, J. N. High-concentration, surfactant-stabilized graphene dispersions. *ACS Nano* **4,** 3155–3162 (2010).

150. Bonaccorso, F. *et al.* Graphene, related two-dimensional crystals, and hybrid systems for energy conversion and storage. *Science* **347,** (2015).

151. Naik, G. V., Shalaev, V. M. & Boltasseva, A. Alternative plasmonic materials: Beyond gold and silver. *Advanced Materials* **25,** 3264–3294 (2013).

152. Fang, Z. *et al.* Gated tunability and hybridization of localized plasmons in nanostructured graphene. *ACS Nano* **7,** 2388–2395 (2013).

153. Brar, V. W., Jang, M. S., Sherrott, M., Lopez, J. J. & Atwater, H. A. Highly confined tunable mid-infrared plasmonics in graphene nanoresonators. *Nano Lett.* **13,** 2541–

2547 (2013).

154. Jablan, M., Buljan, H. & Solja??i??, M. Plasmonics in graphene at infrared frequencies. *Phys. Rev. B - Condens. Matter Mater. Phys.* **80,** 1–7 (2009).

155. West, P. R. *et al.* Searching for better plasmonic materials. *Laser and Photonics Reviews* **4,** 795–808 (2010).

156. Nair, R. R. *et al.* Fine structure constant defines visual transparency of graphene. *Science (80-.).* **320,** 1308 (2008).

157. Mueller, T., Xia, F. & Avouris, P. Graphene photodetectors for high-speed optical communications. *Nat. Photonics* **4,** 297–301 (2010).

158. Schedin, E Lidorikis, a Lombardo, V G Kravets, a K Geim, a N Grigorenko, K S Novoselov, a C. F. Surface-enhanced Raman spectroscopy of graphene. *ACS Nano* **4,** 5617–5626 (2010).

159. Wang, P., Zhang, D., Zhang, L. & Fang, Y. The SERS study of graphene deposited by gold nanoparticles with 785 nm excitation. *Chem. Phys. Lett.* **556,** 146–150 (2013).

160. Wang, Y. *et al.* Gold on graphene as a substrate for surface enhanced Raman scattering study. *Appl. Phys. Lett.* **97,** (2010).

161. Xu, W. *et al.* Surface enhanced Raman spectroscopy on a flat graphene surface. *Proc. Natl. Acad. Sci.* **109,** 9281–9286 (2012).

162. Lee, J., Shim, S., Kim, B. & Shin, H. S. Surface-enhanced Raman scattering of single- and few-layer graphene by the deposition of gold nanoparticles. *Chemistry* **17,** 2381–7 (2011).

163. Fang, Z. *et al.* Graphene-antenna sandwich photodetector. *Nano Lett.* **12,** 3808–13 (2012).

164. Liu, Y. *et al.* Plasmon resonance enhanced multicolour photodetection by graphene. *Nat. Commun.* **2,** (2011).

165. Echtermeyer, T. J. *et al.* Strong plasmonic enhancement of photovoltage in graphene. *Nat. Commun.* **2,** 1–6 (2011).

166. Gan, X. *et al.* Chip-integrated ultrafast graphene photodetector with high responsivity. *Nat. Photonics* **7,** 883–887 (2013).

167. Echtermeyer, T. J. *et al.* Surface Plasmon Polariton Graphene Photodetectors. *Nano Lett.* **16,** 8–20 (2016).

168. Salihoglu, O., Balci, S. & Kocabas, C. Plasmon-polaritons on graphene-metal surface and their use in biosensors. *Appl. Phys. Lett.* **100,** (2012).

169. Hashemi, M., Farzad, M. H., Asger Mortensen, N. & Xiao, S. Enhanced absorption of graphene in the visible region by use of plasmonic nanostructures. *J. Opt. (United Kingdom)* **15,** (2013).

170. Kim, J. *et al.* Electrical Control of Optical Plasmon Resonance with Graphene. *Nano Lett.* **12,** 5598–5602 (2012).

171. Emani, N. K. *et al.* Electrical Modulation of Fano Resonance in Plasmonic Nanostructures Using Graphene. *Nano Lett.* **14,** 78–82 (2014).

172. Zhu, X. *et al.* Enhanced light-matter interactions in graphene-covered gold nanovoid arrays. *Nano Lett.* **13,** 4690–4696 (2013).

173. Vicarelli, L., Heerema, S. J., Dekker, C. & Zandbergen, H. W. Controlling defects in graphene for optimizing the electrical properties of graphene nanodevices. *ACS Nano* **9,** 3428–3435 (2015).

174. Kravets, V. G. V. G. *et al.* Surface hydrogenation and optics of a graphene sheet transferred onto a plasmonic nanoarray. *J. Phys. Chem. C* **116,** 3882–3887 (2011).

175. Xu, G. *et al.* Plasmonic graphene transparent conductors. *Adv. Mater.* **24,** (2012).

176. Wang, X., Chen, Y. P. & Nolte, D. D. Strong anomalous optical dispersion of graphene: complex refractive index measured by Picometrology. *Opt. Express* **16,** 22105 (2008).

177. Hoggard, A. *et al.* Using the plasmon linewidth to calculate the time and efficiency of electron transfer between gold nanorods and graphene. *ACS Nano* **7,** 11209–11217 (2013).

178. Gilbertson, A. M. *et al.* Plasmon-induced optical anisotropy in hybrid graphene-metal nanoparticle systems. *Nano Lett.* **15,** 3458–3464 (2015).

179. Liu, M., Yin, X., Wang, F. & Zhang, X. Graphene optical modulator. *SPIE Opt. 2011* **8101,** 81010J–81010J–6 (2011).

180. Emani, N. K. *et al.* Electrically tunable damping of plasmonic resonances with graphene. *Nano Lett.* **12,** 5202–5206 (2012).

181. Tantiwanichapan, K. *et al.* Graphene Terahertz Plasmons: A Combined Transmission Spectroscopy and Raman Microscopy Study. *ACS Photonics* **4,** 2011–2017 (2017).

182. Valmorra, F. *et al.* Low-bias active control of terahertz waves by coupling large-area CVD graphene to a terahertz metamaterial. *Nano Lett.* **13,** 3193–3198 (2013).

183. Das, A. *et al.* Monitoring dopants by Raman scattering in an electrochemically top-gated graphene transistor. *Nat. Nanotechnol.* **3,** 210–215 (2008).

184. Qian, H. *et al.* Electrical tuning of surface plasmon polariton propagation in graphene-nanowire hybrid structure. *ACS Nano* **8,** 2584–2589 (2014).

185. Nie, S. & Emory, S. R. Probing single molecules and single nanoparticles by surface-enhanced Raman scattering. *Science (80-.).* **275,** 1102–1106 (1997).

186. Stiles, P. L., Dieringer, J. A., Shah, N. C. & Van Duyne, R. P. Surface-Enhanced Raman Spectroscopy. *Annu. Rev. Anal. Chem.* **1,** 601–626 (2008).

187. Sur, U. K. Surface-enhanced Raman spectroscopy. *Resonance* **15,** 154–164 (2010).

188. Ferrari, A. C. *et al.* Raman spectrum of graphene and graphene layers. *Phys. Rev. Lett.* **97,** 1–4 (2006).

189. Casiraghi, C., Pisana, S., Novoselov, K. S., Geim, A. K. & Ferrari, A. C. Raman fingerprint of charged impurities in graphene. *Appl. Phys. Lett.* **91,** (2007).

190. Casiraghi, C. *et al.* Raman spectroscopy of graphene edges. *Nano Lett.* **9,** 1433–1441 (2009).

191. Ferrari, A. C. Raman spectroscopy of graphene and graphite: Disorder, electron-phonon coupling, doping and nonadiabatic effects. *Solid State Commun.* **143,** 47–57 (2007).

192. Liu, J. *et al.* The dependence of graphene Raman D-band on carrier density. *Nano Letters* **13,** 6170–6175 (2013).

193. Eckmann, A. *et al.* Probing the nature of defects in graphene by Raman spectroscopy. *Nano Lett.* **12,** 3925–3930 (2012).

194. You, S. A., Kwon, O. S. & Jang, J. A facile synthesis of uniform Ag nanoparticle decorated CVD-grown graphene via surface engineering. *J. Mater. Chem.* **22,** 17805 (2012).

195. Xu, W. *et al.* Graphene-veiled gold substrate for surface-enhanced raman spectroscopy. *Adv. Mater.* **25,** 928–933 (2013).

196. Xu, H., Xie, L., Zhang, H. & Zhang, J. Effect of graphene Fermi level on the Raman scattering intensity of molecules on graphene. in *ACS Nano* **5,** 5338–5344 (2011).

197. Kim, N., Oh, M. K., Park, S., Kim, S. K. & Hong, B. H. Effect of gold substrates on the raman spectra of graphene. *Bull. Korean Chem. Soc.* **31,** 999–1003 (2010).

198. Omnes, F. Introduction to Semiconductor Photodetectors. in *Optoelectronic Sensors* 1–14 (2010). doi:10.1002/9780470611630.ch1

199. Streetman, B. G. & Banerjee, S. *Solid state electronic devices*. *Prentice Hall series in solid state physical electronics* (2000).

200. Dawlaty, J. M., Shivaraman, S., Chandrashekhar, M., Rana, F. & Spencer, M. G. Measurement of ultrafast carrier dynamics in epitaxial graphene. *Appl. Phys. Lett.* **92,** (2008).

201. Kuzmenko, A. B., Van Heumen, E., Carbone, F. & Van Der Marel, D. Universal optical conductance of graphite. *Phys. Rev. Lett.* **100,** (2008).

202. Dawlaty, J. M. *et al.* Measurement of the optical absorption spectra of epitaxial graphene from terahertz to visible. *Appl. Phys. Lett.* **93,** (2008).

203. Bonaccorso, F., Sun, Z., Hasan, T. & Ferrari, A. C. Graphene photonics and optoelectronics. *Nat. Photonics* **4,** 611–622 (2010).

204. Chakraborty, C. *et al.* Optical antenna enhanced graphene photodetector. *Appl. Phys. Lett.* **105,** (2014).

205. Pospischil, A. *et al.* CMOS-compatible graphene photodetector covering all optical communication bands. *Nat. Photonics* **7,** 892–896 (2013).

206. Kang, P., Wang, M. C., Knapp, P. M. & Nam, S. W. Photodetectors: Crumpled Graphene Photodetector with Enhanced, Strain-Tunable, and Wavelength-Selective Photoresponsivity (Adv. Mater. 23/2016). *Advanced Materials* **28,** 4565 (2016).

207. Xia, F., Mueller, T., Lin, Y. M., Valdes-Garcia, A. & Avouris, P. Ultrafast graphene photodetector. *Nat. Nanotechnol.* **4,** 839–843 (2009).

208. Furchi, M. *et al.* Microcavity-integrated graphene photodetector. *Nano Lett.* **12,** 2773–2777 (2012).

209. Lee, Y. *et al.* High-performance perovskite-graphene hybrid photodetector. *Adv. Mater.* **27,** 41–46 (2015).

210. Kim, M., Kang, P., Leem, J. & Nam, S. A stretchable crumpled graphene photodetector with plasmonically enhanced photoresponsivity. *Nanoscale* **9,** 4058–4065 (2017).

211. Shi, S. F. *et al.* Optimizing broadband terahertz modulation with hybrid graphene/metasurface structures. *Nano Lett.* **15,** 372–377 (2015).

212. Gowda, P., Mohapatra, D. R. & Misra, A. Enhanced photoresponse in monolayer hydrogenated graphene photodetector. *ACS Appl. Mater. Interfaces* **6,** 16763–16768 (2014).

213. Zhang, B. Y. *et al.* Broadband high photoresponse from pure monolayer graphene photodetector. *Nat. Commun.* **4,** (2013).

214. Echtermeyer, T. J. *et al.* Photothermoelectric and photoelectric contributions to light detection in metal-graphene-metal photodetectors. *Nano Lett.* **14,** 3733–3742 (2014).

215. Song, J. C. W., Rudner, M. S., Marcus, C. M. & Levitov, L. S. Hot carrier transport and photocurrent response in graphene. *Nano Lett.* **11,** 4688–4692 (2011).

216. Lemme, M. C. *et al.* Gate-activated photoresponse in a graphene p-n junction. *Nano Lett.* **11,** 4134–4137 (2011).

217. Gabor, N. M. *et al.* Hot carrier-assisted intrinsic photoresponse in graphene. *Science (80-.).* **334,** 648–652 (2011).

218. Freitag, M., Low, T., Xia, F. & Avouris, P. Photoconductivity of biased graphene. *Nat. Photonics* **7,** 53–59 (2013).

219. Mittendorff, M. *et al.* Ultrafast graphene-based broadband THz detector. *Appl. Phys. Lett.* **103,** (2013).

220. Xia, F. *et al.* Photocurrent imaging and efficient photon detection in a graphene transistor. *Nano Lett.* **9,** 1039–1044 (2009).

221. Freitag, M. *et al.* Photocurrent in graphene harnessed by tunable intrinsic plasmons. *Nat. Commun.* **4,** (2013).

222. Yao, Y. *et al.* High-responsivity mid-infrared graphene detectors with antenna-enhanced photocarrier generation and collection. *Nano Lett.* **14,** 3749–3754 (2014).

223. Vicarelli, L. *et al.* Graphene field-effect transistors as room-temperature terahertz detectors. *Nat. Mater.* **11,** 865–871 (2012).

224. Graham, M. W., Shi, S. F., Ralph, D. C., Park, J. & McEuen, P. L. Photocurrent measurements of supercollision cooling in graphene. *Nat. Phys.* **9,** 103–108 (2013).

225. Miseikis, V. *et al.* Rapid CVD growth of millimetre-sized single crystal graphene using a cold-wall reactor. *2D Mater.* **2,** 014006 (2015).

226. Wang, Y. *et al.* Electrochemical delamination of CVD-grown graphene film: Toward the recyclable use of copper catalyst. *ACS Nano* **5,** 9927–9933 (2011).

227. d'Angelo, P., Behrmann, K.-U., Jenny, A., Nowozin, S. & Halley, E. Hugin. (2010).

228. Mohammad, M. A., Muhammad, M., Dew, S. K. & Stepanova, M. Fundamentals of electron beam exposure and development. in *Nanofabrication: Techniques and Principles* **9783709104,** 11–41 (2012).

229. Rius Suñé, G., Pérez Murano, F. & Bausells Roige, J. *Electron beam lithography for nanofabrication*. (Universitat Autònoma de Barcelona, 2008).

230. Kirchner, M. & Kahl, M. Raith-electron beam lithography for research. in *Acta Physica Polonica A* **116,** (2009).

231. Pease, R. F. W. Electron beam lithography. *Contemp. Phys.* **22,** 265–290 (1981).

232. McCord, M. A. & Rooks, M. J. SPIE handbook of microlithography, micromachining and microfabrication. in *SPIE, Bellingham* (2000).

233. Nabity, J., Compbell, L. A., Zhu, M. & Zhou, W. E-beam nanolithography integrated with scanning electron microscope. in *Scanning Microscopy for Nanotechnology: Techniques and Applications* 120–151 (2007). doi:10.1007/978-0-387-39620-0_5

234. Chang, T. H. P. Proximity effect in electron-beam lithography. *J. Vac. Sci. Technol.* **12,** 1271–1275 (1975).

235. Altissimo, M. E-beam lithography for micro-/nanofabrication. *Biomicrofluidics* **4,** 026503 (2010).

236. Robin, F. Electron-Beam Lithography Applications at ETH Zurich, Raith application note. *Raith GmbH* 1–4 (2006).

237. Hoffmann, J., Hafner, C., Leidenberger, P., Hesselbarth, J. & Burger, S. Comparison of electromagnetic field solvers for the 3D analysis of plasmonic nano antennas.

(2009). doi:10.1117/12.828036

238. COMSOL Multiphysics. Introduction to COMSOL Multiphysics. *Manual* 168 (2009).

239. Malitson, I. H. Interspecimen Comparison of the Refractive Index of Fused Silica*,†. *J. Opt. Soc. Am.* **55,** 1205 (1965).

240. Rakic, A. D., Djurisic, A. B., Elazar, J. M. & Majewski, M. L. Optical properties of metallic films for vertical-cavity optoelectronic devices. *Appl. Opt.* **37,** 5271–5283 (1998).

241. Malitson, I. H. A Redetermination of Some Optical Properties of Calcium Fluoride. *Appl. Opt.* **2,** 1103–1107 (1963).

242. Farmer, D. B., Rodrigo, D., Low, T. & Avouris, P. Plasmon-Plasmon Hybridization and Bandwidth Enhancement in Nanostructured Graphene. *Nano Lett.* **15,** 2582–2587 (2015).

243. Rodrigo, D. *et al.* Mid-infrared plasmonic biosensing with graphene. *Science (80-.).* **349,** 165–168 (2015).

244. Li, X., Wang, X., Zhang, L., Lee, S. & Dai, H. Chemically derived, ultrasmooth graphene nanoribbon semiconductors. *Science (80-.).* **319,** 1229–1232 (2008).

245. Son, Y. W., Cohen, M. L. & Louie, S. G. Energy gaps in graphene nanoribbons. *Phys. Rev. Lett.* **97,** (2006).

246. Abbas, A. N. *et al.* Patterning, characterization, and chemical sensing applications of graphene nanoribbon arrays down to 5 nm using helium ion beam lithography. *ACS Nano* **8,** 1538–1546 (2014).

247. Kawai, S. *et al.* Atomically controlled substitutional boron-doping of graphene nanoribbons. *Nat. Commun.* **6,** (2015).

248. Yu, W. J. & Duan, X. Tunable transport gap in narrow bilayer graphene nanoribbons. *Sci. Rep.* **3,** (2013).

249. Ferrari, A. C. & Basko, D. M. Raman spectroscopy as a versatile tool for studying the properties of graphene. *Nat. Nanotechnol.* **8,** 235–246 (2013).

250. Cançado, L. G. *et al.* Quantifying defects in graphene via Raman spectroscopy at different excitation energies. *Nano Lett.* **11,** 3190–3196 (2011).

251. Cançado, L. G., Pimenta, M. A., Neves, B. R. A., Dantas, M. S. S. & Jorio, A. Influence of the atomic structure on the Raman spectra of graphite edges. *Phys. Rev. Lett.* **93,** (2004).

252. Cançado, L. G. *et al.* Anisotropy of the Raman spectra of nanographite ribbons. *Phys. Rev. Lett.* **93,** 047403-1 (2004).

253. Bischoff, D. *et al.* Raman spectroscopy on etched graphene nanoribbons. *J. Appl. Phys.* **109,** (2011).

254. Tuinstra, F. & Koenig, J. L. Raman Spectrum of Graphite. *J. Chem. Phys.* **53,** 1126–1130 (1970).

255. Basko, D. M. Theory of resonant multiphonon Raman scattering in graphene. *Phys. Rev. B - Condens. Matter Mater. Phys.* **78,** (2008).

256. Ferrari, A. C. & Robertson, J. Resonant Raman spectroscopy of disordered, amorphous, and diamondlike carbon. *Phys. Rev. B* **64,** 075414 (2001).

257. Graf, D. *et al.* Spatially resolved raman spectroscopy of single- and few-layer graphene. *Nano Lett.* **7,** 238–242 (2007).

258. Ryu, S., Maultzsch, J., Han, M. Y., Kim, P. & Brus, L. E. Raman spectroscopy of lithographically patterned graphene nanoribbons. *ACS Nano* **5,** 4123–4130 (2011).

259. Kang, S., Movva, H. C. P., Sanne, A., Rai, A. & Banerjee, S. K. Influence of electron-beam lithography exposure current level on the transport characteristics of graphene field effect transistors. *J. Appl. Phys.* **119,** (2016).

260. Liu, L. *et al.* Graphene oxidation: Thickness-dependent etching and strong chemical doping. *Nano Lett.* **8,** 1965–1970 (2008).

261. Paredes, J. I., Martínez-Alonso, A. & Tascón, J. M. D. Multiscale imaging and tip-scratch studies reveal insight into the plasma oxidation of graphite. *Langmuir* **23,** 8932–8943 (2007).

262. Yoon, Y. & Guo, J. Effect of edge roughness in graphene nanoribbon transistors. *Appl. Phys. Lett.* **91,** (2007).

263. Basu, D., Gilbert, M. J., Register, L. F., Banerjee, S. K. & MacDonald, A. H. Effect of edge roughness on electronic transport in graphene nanoribbon channel metal-oxide-semiconductor field-effect transistors. *Appl. Phys. Lett.* **92,** 2006–2009 (2008).

264. Tan, Y. W. *et al.* Measurement of scattering rate and minimum conductivity in

graphene. *Phys. Rev. Lett.* **99,** 10–13 (2007).

265. Han, M. Y., Brant, J. C. & Kim, P. Electron transport in disordered graphene nanoribbons. *Phys. Rev. Lett.* **104,** 2–5 (2010).

266. Yang, L., Park, C. H., Son, Y. W., Cohen, M. L. & Louie, S. G. Quasiparticle energies and band gaps in graphene nanoribbons. *Phys. Rev. Lett.* **99,** (2007).

267. Bennett, P. B. *et al.* Bottom-up graphene nanoribbon field-effect transistors. *Appl. Phys. Lett.* **103,** 253114 (2013).

268. Chen, J. H. *et al.* Charged-impurity scattering in graphene. *Nat. Phys.* **4,** 377–381 (2008).

269. Giovannetti, G. *et al.* Doping graphene with metal contacts. *Phys. Rev. Lett.* **101,** (2008).

270. Ghosh, a, Late, D. J., Panchakarla, L. S., Govindaraj, a & Rao, C. N. R. NO2 and humidity sensing characteristics of few-layer graphenes. *J. Exp. Nanosci.* **4,** 313–322 (2009).

271. Hu, J., Ruan, X. & Chen, Y. P. Thermal conductivity and thermal rectification in graphene nanoribbons: A molecular dynamics study. *Nano Lett.* **9,** 2730–2735 (2009).

272. Schroder, D. K. *Semiconductor Material and Device Characterization: Third Edition*. *Semiconductor Material and Device Characterization: Third Edition* (2005). doi:10.1002/0471749095

273. Zhong, H., Zhang, Z., Xu, H., Qiu, C. & Peng, L. M. Comparison of mobility extraction methods based on field-effect measurements for graphene. *AIP Adv.* **5,** (2015).

274. Yu, X. *et al.* A high performance, visible to mid-infrared photodetector based on graphene nanoribbons passivated with HfO_2. *Nanoscale* **8,** 327–332 (2016).

275. Xu, W. & Lee, T.-W. Recent progress in fabrication techniques of graphene nanoribbons. *Mater. Horiz.* **3,** 186–207 (2016).

276. Fang, T., Konar, A., Xing, H. & Jena, D. Mobility in semiconducting graphene nanoribbons: Phonon, impurity, and edge roughness scattering. *Phys. Rev. B - Condens. Matter Mater. Phys.* **78,** (2008).

277. Lian, C. *et al.* Quantum transport in graphene nanoribbons patterned by metal masks.

Appl. Phys. Lett. **96,** (2010).

278. Betti, A., Fiori, G. & Iannaccone, G. Strong mobility degradation in ideal graphene nanoribbons due to phonon scattering. *Appl. Phys. Lett.* **98,** (2011).

279. Nagashio, K., Nishimura, T. & Toriumi, A. Estimation of residual carrier density near the Dirac point in graphene through quantum capacitance measurement. *Appl. Phys. Lett.* **102,** (2013).

280. Brey, L. & Fertig, H. A. Electronic states of graphene nanoribbons studied with the Dirac equation. *Phys. Rev. B* **73,** 2–6 (2006).

281. Barone, V., Hod, O. & Scuseria, G. E. Electronic structure and stability of semiconducting graphene nanoribbons. *Nano Lett.* **6,** 2748–2754 (2006).

282. Yan, H. *et al.* Infrared spectroscopy of tunable Dirac terahertz magneto-plasmons in graphene. *Nano Lett.* **12,** 3766–3771 (2012).

283. Otsuji, T., Popov, V. & Ryzhii, V. Active graphene plasmonics for terahertz device applications. *J. Phys. D. Appl. Phys.* **47,** (2014).

284. Fei, Z. *et al.* Infrared nanoscopy of dirac plasmons at the graphene-SiO2interface. *Nano Lett.* **11,** 4701–4705 (2011).

285. Nikitin, A. Y., Guinea, F., Garcia-Vidal, F. J. & Martin-Moreno, L. Surface plasmon enhanced absorption and suppressed transmission in periodic arrays of graphene ribbons. 1–5 (2011). doi:10.1103/PhysRevB.85.081405

286. Areshkin, D. A., Gunlycke, D. & White, C. T. Ballistic transport in graphene nanostrips in the presence of disorder: Importance of edge effects. *Nano Lett.* **7,** 204–210 (2007).

287. Gambaudo, J.-M. & Vignolo, P. Brillouin zone labelling for quasicrystals. *New J. Phys.* **16,** 043013 (2014).

288. Douketis, C., Wang, Z., Haslett, T. L. & Moskovits, M. Fractal character of cold-deposited silver films determined by low-temperature scanning tunneling microscopy. *Phys. Rev. B* **51,** 11022 (1995).

289. Genet, C. & Ebbesen, T. W. Light in tiny holes. *Nature* **445,** 39–46 (2007).

290. Gopinath, A., Boriskina, S. V., Feng, N. N., Reinhard, B. M. & Dal Negro, L. Photonic-plasmonic scattering resonances in deterministic aperiodic structures. *Nano Lett.* **8,** 2423–2431 (2008).

291. Ebbesen, T. W. *et al.* Extraordinary optical transmission through sub-wavelength hole arrays. *Nature* **86,** 1114–7 (1998).

292. Matsui, T., Agrawal, A., Nahata, A. & Vardeny, Z. V. Transmission resonances through aperiodic arrays of subwavelength apertures. *Nature* **446,** 517–521 (2007).

293. Kravets, V. G., Schedin, F. & Grigorenko, A. N. Extremely narrow plasmon resonances based on diffraction coupling of localized plasmons in arrays of metallic nanoparticles. *Phys. Rev. Lett.* **101,** (2008).

294. Auguié, B. & Barnes, W. L. Collective resonances in gold nanoparticle arrays. *Phys. Rev. Lett.* **101,** (2008).

295. Lochbihler, H. Surface polaritons on gold-wire gratings. *Phys. Rev. B* **50,** 4795–4801 (1994).

296. Luk'yanchuk, B. *et al.* The Fano resonance in plasmonic nanostructures and metamaterials. *Nat. Mater.* **9,** 707–715 (2010).

297. Chirumamilla, M. *et al.* Hot-Spot Engineering in 3D Multi-Branched Nanostructures: Ultrasensitive Substrates for Surface-Enhanced Raman Spectroscopy. *Adv. Opt. Mater.* **5,** (2017).

298. Nieckarz, R. J., Oomens, J., Berden, G., Sagulenko, P. & Zenobi, R. Infrared multiple photon dissociation (IRMPD) spectroscopy of oxazine dyes. *Phys. Chem. Chem. Phys.* **15,** 5049 (2013).

299. Huh, S., Park, J., Kim, K. S., Hong, B. H. & Kim, S. Bin. Selective n-type doping of graphene by photo-patterned gold nanoparticles. *ACS Nano* **5,** 3639–3644 (2011).

300. Wu, Y. *et al.* Tuning the doping type and level of graphene with different gold configurations. *Small* **8,** 3129–3136 (2012).

301. Ifuku, R., Nagashio, K., Nishimura, T. & Toriumi, A. The density of states of graphene underneath a metal electrode and its correlation with the contact resistivity. *Appl. Phys. Lett.* **103,** (2013).

302. Di Bartolomeo, A. Graphene Schottky diodes: An experimental review of the rectifying graphene/semiconductor heterojunction. *Phys. Rep.* **606,** 1–58 (2016).

303. Pi, K. *et al.* Electronic doping and scattering by transition metals on graphene. *Phys. Rev. B - Condens. Matter Mater. Phys.* **80,** (2009).

304. McCreary, K. M. *et al.* Effect of cluster formation on graphene mobility. *Phys. Rev.*

B - Condens. Matter Mater. Phys. **81,** (2010).

305. McCreary, K. M., Pi, K. & Kawakami, R. K. Metallic and insulating adsorbates on graphene. *Appl. Phys. Lett.* **98,** (2011).

306. Ferreira, A. & Peres, N. M. R. Complete light absorption in graphene-metamaterial corrugated structures. *Phys. Rev. B - Condens. Matter Mater. Phys.* **86,** (2012).

307. Niu, J. *et al.* Shifting of surface plasmon resonance due to electromagnetic coupling between graphene and Au nanoparticles. *Opt. Express* **20,** 19690 (2012).

308. Niu, J., Jun Shin, Y., Lee, Y., Ahn, J. H. & Yang, H. Graphene induced tunability of the surface plasmon resonance. *Appl. Phys. Lett.* **100,** (2012).

309. Osváth, Z. *et al.* The structure and properties of graphene on gold nanoparticles. *Nanoscale* **7,** 5503–5509 (2015).

310. Haghighian, N. *et al.* Morphological modulation of graphene-mediated hybridization in plasmonic systems. *Phys. Chem. Chem. Phys.* **18,** 27493–27499 (2016).

311. Polyushkin, D. K. *et al.* Graphene as a substrate for plasmonic nanoparticles. *J. Opt. (United Kingdom)* **15,** (2013).

312. Zhao, Y. *et al.* Strong light–matter interactions in sub-nanometer gaps defined by monolayer graphene: toward highly sensitive SERS substrates. *Nanoscale* **6,** 11112–11120 (2014).

313. Sze, S. M. & Ng, K. K. *Physics of Semiconductor Devices*. *Physics of semiconductor device* (2006). doi:10.1049/ep.1970.0039

314. Li, K. *et al.* Photovoltage responses of graphene-Au heterojunctions. *AIP Adv.* **7,** (2017).

315. Rossi, A. *et al.* Patterned tungsten disulfide/graphene heterostructures for efficient multifunctional optoelectronic devices. *Nanoscale* **10,** 4332–4338 (2018).

316. Richards, P. L. Bolometers for infrared and millimeter waves. *J. Appl. Phys.* **76,** 1–24 (1994).

317. Kim, C. O. *et al.* High photoresponsivity in an all-graphene p-n vertical junction photodetector. *Nat. Commun.* **5,** (2014).

318. McKitterick, C. B., Prober, D. E., Vora, H. & Du, X. Ultrasensitive graphene far-infrared power detectors. *J. Phys. Condens. Matter* **27,** (2015).

319. Tauk, R. *et al.* Plasma wave detection of terahertz radiation by silicon field effects transistors: Responsivity and noise equivalent power. *Appl. Phys. Lett.* **89,** (2006).

320. Koppens, F. H. L. *et al.* Photodetectors based on graphene, other two-dimensional materials and hybrid systems. *Nat. Nanotechnol.* **9,** 780–793 (2014).

321. Brongersma, M. L. L., Halas, N. J. J. & Nordlander, P. Plasmon-induced hot carrier science and technology. *Nature Nanotechnology* **10,** 25–34 (2015).

322. Wei, P., Bao, W., Pu, Y., Lau, C. N. & Shi, J. Anomalous thermoelectric transport of dirac particles in graphene. *Phys. Rev. Lett.* **102,** (2009).

323. Sun, Z. *et al.* Graphene and Graphene-like Two-Dimensional Materials in Photodetection : Mechanisms. 4133–4156 (2014).

324. Mueller, T., Xia, F., Freitag, M., Tsang, J. & Avouris, P. Role of contacts in graphene transistors: A scanning photocurrent study. *Phys. Rev. B - Condens. Matter Mater. Phys.* **79,** (2009).

325. Winzer, T., Knorr, A. & Malic, E. Carrier multiplication in graphene. *Nano Lett.* **10,** 4839–4843 (2010).

326. Aygar, A. M. *et al.* Comparison of Back and Top Gating Schemes with Tunable Graphene Fractal Metasurfaces. *ACS Photonics* **3,** 2303–2307 (2016).

327. Shiue, R. J. *et al.* High-Responsivity Graphene-Boron Nitride Photodetector and Autocorrelator in a Silicon Photonic Integrated Circuit. *Nano Lett.* **15,** 7288–7293 (2015).

328. Yankowitz, M., Xue, J. & LeRoy, B. J. Graphene on hexagonal boron nitride. *J. Phys. Condens. Matter* **26,** 303201 (2014).